MULTISCALE MODELING OF ELECTROMAGNETIC RADIATION TRANSPORT

A Dissertation
Submitted to the Graduate Faculty
of the
North Dakota State University
of Agriculture and Applied Science

By

Erik David Sapper

In Partial Fulfillment of the Requirements
for the Degree of
DOCTOR OF PHILOSOPHY

Major Department:
Coatings and Polymeric Materials

December 2012

Fargo, North Dakota

North Dakota State University
Graduate School

Title

Multiscale Modeling of Electromagnetic Radiation Transport

By

Erik David Sapper

The Supervisory Committee certifies that this disquisition complies with North Dakota State University's regulations and meets the accepted standards for the degree of

DOCTOR OF PHILOSOPHY

SUPERVISORY COMMITTEE:

Dr. Brian Hinderliter
Chair

Dr. Stuart Croll

Dr. Vicki Gelling

Dr. Daniel Kroll

Approved:

December 18, 2012
Date

Dr. Dean Webster
Department Chair

ABSTRACT

The transport of electromagnetic radiation is a critical factor in determining many of the advanced features of novel materials, composites, and coatings systems. The radiation interaction with a material's surface, as well as its transport and interaction within the material, both combine to produce the overall electromagnetic signature of that object, which is the root cause of the color and appearance of these materials.

Historically, approaches to light scattering behavior prediction focus on either the surface interactions or the bulk interactions. The models most used today are valid only for certain compatible size and length scales of radiation. As next generation materials become more advanced and increasingly have formulation components that reside on the nanoscale, a robust, rigorous, yet highly general approach to electromagnetic signature prediction is required.

A hybrid, multiscale approach to the computational prediction of light scattering by coatings and composite materials is presented here, where ray tracing and geometric optics formalism tracks individual photons as they enter the material of interest, and finite element solutions to the Maxwell equations are used to generate the radiation interaction result of nanoscale inclusions embedded within the bulk of the material. The approach presented here is highly general in nature; scattering inclusions may be pigments, fibers, nanoparticles, air voids, or heterogeneous phase components. The multiscale approach enables investigation of the electromagnetic signature at various length scales, and predicts spectral reflectance, directional reflectance, and color, among other properties, of various multicomponent systems.

ACKNOWLEDGMENTS

I would first like to graciously acknowledge my advisor, Dr. Brian Hinderliter, without whom little of this would have been possible. Brian's patience and guidance are second to none. Thanks, Brian, for tackling this problem with me, even as we reside on separate coasts.

I would further like to thank the members of my graduate committee for being supportive during this endeavor, and for ensuring my tenure at North Dakota State University was a worthwhile intellectual endeavor.

Finally, I would like to acknowledge the Army Research Laboratory for funding this effort, under ARL grant #14518, as well as that grant's principal investigator, Prof. Victoria Johnston Gelling, at North Dakota State University, for her support of the work.

-EDS

DEDICATION

Dedicated to Jennifer, Jane, and Solomon; my Snowflake, my Little Nut, and my Sauce.

-EDS

TABLE OF CONTENTS

LIST OF TABLES

LIST OF FIGURES

LIST OF APPENDIX TABLES

CHAPTER 1. ELECTROMAGNETIC RADIATION TRANSPORT AND COMPUTATIONAL METHODS

"A photon goes from point to point. That explains all about optics; that's the entire theory of light!"

– Richard P Feynman[1]

1.1. Introduction

The high performance and novel traits of many advanced engineering materials are increasingly being defined, in one way or another, by one or more of their transport properties. While molecular transport properties account for a large variety of material properties, electromagnetic radiation transport properties are the main contributors to color, appearance, material visual quality, as well as the detectability of a material by many various sorts of detectors, ranging from human and other mammalian eyes, to advanced military applications like radar detectors. The human eyes can perceive color changes from roughness and microscale pigments, but the human eye as an instrument, though a very workable and useful tool for us humans, is not that advanced an instrument from a universal perspective. Indeed, every distinct species of animal has a different set of standard observer functions that inform the owner or observer of the color of visual effect that is rendered or seen in the animal brain. Blaze orange is a staple color in hunting apparel that is highly observable to humans and warns of neighbors within range, but in ducks or other wildlife the standard observer functions around orange are not as great, and so that same blaze orange that is obnoxious to human eyes blends into the environment as seen by a duck or a bear. In this way, the blaze orange safety garments call attention to humans where needed without interfering with the "cover" so necessary to most hunting outings. In similar fashion, advanced materials may

be designed that obfuscate detection in specified bandwidths, while remaining visible to other spectral ranges.

Furthermore, as materials become more advanced technologically (for example, consider the newest class of stealth coatings and metamaterials), the entire electromagnetic spectrum signature or fingerprint becomes relevant. Especially when the "eye" observing a surface might be a highly advanced computer detector spectrophotometer, the entire electromagnetic signature must be considered; not only what the human eye can observe.

The introduction and increasing use of nanomaterials in composites and other materials has provided another reason to study the fundamental color and appearance properties of materials containing these nanoscale elements. While commonly sold or touted as being "invisible" or “clear” in formulations, thirty nanometer diameter silica nanoparticles still scatter and interact with incident radiation. Because a human observer in the lab cannot tell the difference between a polyurethane clearcoat with nanoparticles and a polyurethane clearcoat without nanoparticles does not mean that the difference is undetectable or not real, per se, and also does not mean that light is interacting with both materials equally or equivalently, an inference that is commonly made at the application level. One goal of this research is to provide a virtual, multiscale laboratory, where the differences in electromagnetic signature of nanocomposite materials may be investigated, measured, and controlled.

The research effort presented in part in this dissertation attempts to combine aspects from various fields, spanning from biological transport through diffusive tissue media[2], to highly mathematical analytical solutions to many body scattering problems[3-5], with the hope that a unifying set of models and computational approaches may be combined into a single suite or toolbox of methods, which can address many different scattering problems at many different length scales, from nanoscale inclusions and nanoscale surface roughnesses on optically flat surfaces, to

templated and highly-engineered materials like icephobic coating materials that have fractal surface roughness patterns, and multilayer systems common to automotive, aerospace, and energy harvesting industries. Indeed, the methods presented here are almost entirely scalable across many problem geometries, so that the same mathematical formalism used to address nanoscale surface roughness scattering may also be used to predict the light scattering behavior of lunar regolith and wavy ocean surfaces. The complexity hinges on the definition of a problem-specific geometric limit, and effective switching of solution regimes below, near, and above the geometric limit will ultimately determine the robustness and applicability of the solutions presented here.

1.2. Impact, implications, and applications of this work

The multiscale hybrid approach to light scattering simulation presented in this work represents a novel shift from detailed, length scale- and application-specific light scattering models, towards modeling approaches that are highly general and adaptive, yet are fundamentally rigorous but still computationally efficient in the process.

The hybrid approach to light scattering simulation provides a virtual, *in silico* multiscale laboratory, where the differences in electromagnetic signature of nanocomposite materials may be investigated, measured, and controlled. Because the approach presented here relies on both ray tracing approaches and finite element calculations of the Maxwell equations, the size scale of the composite, coating, or material of interest is arbitrary; this approach can handle quantum dot scattering as easily as it can ocean wave or desert dune scattering.

The hybrid approach presented here will serve to broaden and expand the available knowledge of the light scattering behavior of composites, plastics, and surfaces that have at least one dimension on the nanoscale. This dissertation will document benefits of the multiscale approach that are not realizable with traditional methods, such as color change prediction with increasing

surface roughness, reflectance changes during nanocomposite material weathering, and retroreflectance increases in nanocomposites exhibiting local coarseness. Throughout the dissertation references are made to areas for improvement and growth of the multiscale modeling toolbox. Indeed, the design of the approach from the ground up ensures a flexible system adaptable to many different complex problems, and an effort is made to identify room for growth and further implementation.

Specifically, the research presented in this dissertation has accomplished many things:

- A virtual, multiscale laboratory and electromagnetic radiation transport modeling approach has been designed, where the properties of electromagnetic signature of nanocomposite materials may be investigated, measured, and controlled.
- The coupling of surface and bulk scattering into a single adaptive, general, and rigorous approach has been developed and detailed, with an emphasis on coatings applications.
- Photon transport behavior in materials has been compiled into predictions for color and appearance change, as well as detectability when retroreflectance is concerned. This approach has been coupled to earlier Monte Carlo models of photodegradation in order to begin uncovering novel non-destructive evaluation and assessment methods using interrogating light beams.
- Photon transport behavior has been compiled into less common results, such as tracking the number of scattering events per incident photon, or the portion of a surface caught in shadow. These results shed new light on the surface scattering problem, and are useful tools in the assessment of rough surfaces being impinged on by incident radiation.
- Demonstration of retroreflectance onset in nanocomposites exhibiting inclusion coarseness was shown and quantified, representing the expansion of available knowledge concerning the light scattering behavior of nanomaterials. With a multiscale modeling approach such as

the one presented here, a materials designer can detect at what loading level various nanomaterials become detectable by different optical systems and techniques.

- A computer code package was written to translate, interpret, and predict the spectral visual response of materials having nanoscale surface roughnesses.
- A translation matrix for XYZ to CIE L*a*b* was developed, out of necessity, and is documented in Appendix A.

1.3. A framework for multiscale color and appearance modeling: from atoms to appearances

The multiscale framework developed and proposed in this dissertation represents a multidirectional approach to the treatment of complex material systems, electromagnetic radiation transport, and observed or measured electromagnetic signature or color and appearance. A multiscale approach as shown in Figure1-1, becomes increasingly relevant as structures at the meter length scale, such as vehicles, aircraft, buildings, or other architectural structures, all demand tailored and designed electromagnetic signature and visual appearance. In some cases, the demand is for purely aesthetic reasons; consumers want cars that are shiny and appear wet, so color flop and distinctness of image are important manufacturing and R&D considerations in the automotive industry. Or, the demand may be more than aesthetic; the US Army, for instance, is interested in vehicle coatings that have low retroreflectance, matte finishes, blend into their surrounding visual environments, and have low intensity signatures when scanned by advanced optical detection systems. Because of the disparate needs by those interested in electromagnetic signature modeling, the overall light scattering problem must be addressed at length scales beyond those that cover solely the visible electromagnetic spectrum. Target concealment, impact of weathering on target signature, rapid *in silico* screening of novel concepts, and entire electromagnetic spectrum signature beyond the visible range are all areas that are addressable within this multiscale framework.

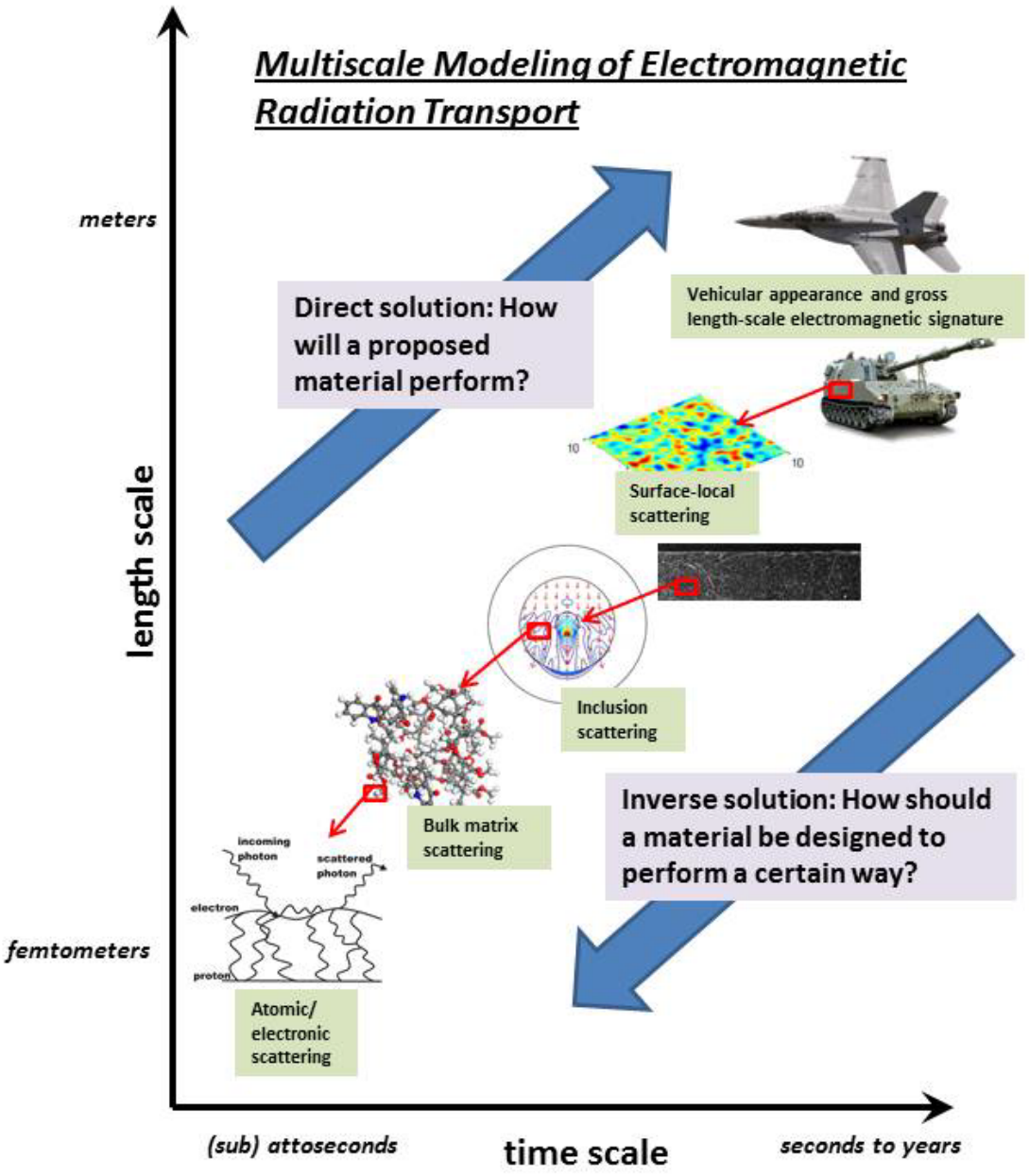

Figure 1-1. The multiscale electromagnetic radiation transport addresses the problem at length scales ranging from electronic to vehicular, and all points in between. Images from author's personal collection and purchased from iStockPhoto.com[6, 7].

At the smallest length and time scales, atomic and electronic scattering occurs, where electrons in a material are jiggled and set to oscillate when bombarded by incident radiation.

Electrons in real materials are bound to protons and neutrons. The oscillating electric field competes with the photons being exchanged between an electron and a proton, and the energy imparted into the system by the incident photon is eventually scattered as a photon leaves the system. These atomistic scattering predictions are computed using the most detailed *ab initio* quantum mechanics software packages, and are computationally expensive. Luckily, for many systems, semi-empirical models may be used to address the scattering behavior.

At the molecular length and time scales, semi-empirical approaches based on molecular orbital theory may be used to predict the scattering behavior of material components in coatings, composites, colored plastics, textiles, and other engineering materials of interest. Care must be taken in this regime, as the semi-empirical computational methods are efficient because they neglect certain complex integrals used in the *ab initio* forms. Because crucial information is sometimes lost in the simplification process, the results of these methods should be benchmarked against empirical measurements made on real, physical materials.

When inclusions are larger than molecules or long-chain oligomeric polymers, the continuum length scale is reached, and finite element methods are used to solve the Maxwell equations for inclusions embedded in homogenous material matrices.

The inclusion scattering events occur, positionally, below the surface of most materials, and surface scattering occurs at larger length scales than the bulk events due to the relatively large surface areas involved. Here, geometric optics ray tracing approaches are used to predict the photon transport properties, such as absorption and scattering, of rough materials.

The surface and bulk scattering prediction components at various length scales may be pieced together to predict the response of large, gross length scale materials, ranging in size from coating sample panels (4 x 6 inches) to airplane wings (tens of meters) to building rooftops (acre length scale). The accuracy of the gross length scale predictions is determined by the accuracy of the

individual components that reside in the lesser length scales. Thus, as problems get larger, greater care must be taken in generating reliable information at the smaller length scales.

The work in this dissertation demonstrates the development and connectivity of the individual length scale components discussed above. Once an operational multiscale framework is in place, the system may be traversed bidirectionally, as shown in Figure 1-1. The direct solution is the common approach, and starts at the smaller length scales and works upwards, addressing what a defined material's response will be at incrementally larger length and time scales. The inverse solution is less common, but represents the more useful approach as far as R&D and product development is concerned. Here, a desired response at the gross length-scale is stated, and the model framework is travelled "backwards," through incrementally smaller length scales, in order to decide what materials should be used to produce the desired response or effect. The quality, generality, and robustness of available inverse methods are a product of the number of quality and well-benchmarked direct methods.

1.4. Electromagnetic radiation interactions with objects

Electromagnetic radiation interactions with matter are a ubiquitous and unavoidable reality that is so common it is sometimes difficult to notice or otherwise give them much thought. Electromagnetic radiation occurs as a set of oscillating electric and magnetic fields that are travelling in concert and which arise naturally (objects emit radiation of all kinds) or are solar-generated (the sun emits photons that an object on the open ground experiences as 10^{27} solar photons per square centimeter flux per year).

There are many interactions that occur when electromagnetic radiation strikes a material. Gloss is defined as specular reflection at the surface of a material, where the angle of the light exiting

the surface is the mirror compliment to the normal of the angle of light striking the surface, shown in Figure 1-2.

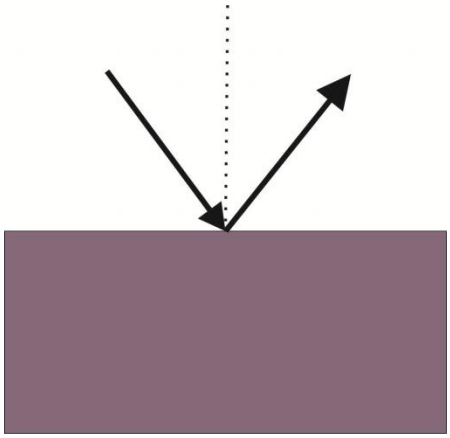

Figure 1-2. Specular scattering off of a perfectly smooth surface; the simplest example of surface scattering.

Mathematically, gloss is defined as the amount of light reflected specularly from a measured surface relative to the maximum amount of light that can be reflected from a perfectly flat surface, which is four percent of the total incident flux at angles of incidence near the surface normal. This four percent value will be discussed in detail later on. Gloss accounts for the shininess or mirror-like qualities of very smooth surfaces.

Any incident radiation that is not specularly reflected is by definition referred to as diffuse surface scattering. Once an incident ray is scattered, there may be some radiation that enters a material, where many additional interactions may occur. Diffuse reflection and scattering within the material are the transport mechanisms that incident radiation undergoes in a bulk material.

Absorption by chromophores in a material is usually responsible for the color of an object seen by an observer[8], while transmission and attenuation through an object impart qualities such as clarity, transparency, and cloudiness[9]. In short, electromagnetic radiation interactions account for and are responsible for the color, appearance, and visual properties of a material, and also construct

or determine the overall electromagnetic signature of an object which extends across the electromagnetic spectrum. This material signature is not limited to visible wavelengths observable by the human detector of choice and familiarity, the eye.

1.5. Electromagnetic radiation scattering and the geometric limit

Light scattering simulation modules typically represent one of the three available scattering regimes: Rayleigh scattering, Mie scattering, and geometric scattering[10, 11]. These regimes are based on a dimensionless size parameter, α, which describes the size of a scattering inclusion relative to the incident wavelength,

$$\alpha = \frac{\pi D_p}{\lambda} \qquad \text{Equation 1-1}$$

In Equation 1-1, D_p is the diameter of the scattering particle, and λ is the wavelength of the incident radiation. When $\alpha << 1$ for the system of interest, the scattering inclusion is much smaller than the wavelength of incident radiation, and Rayleigh scattering dominates. When $\alpha \approx 1$, the scattering inclusion is of the same order of magnitude as the wavelength of incident radiation, and Mie scattering dominates. Finally, when $\alpha >> 1$, the inclusion is much larger than the incident radiation wavelength, and scattering events can be computed in the geometric scattering regime, where Snell's law and Fresnel approximations reduce scattering event predictions to fairly straightforward equations.

A challenge in developing new light scattering simulation approaches is to develop a system that accounts for all length scales of scattering behavior. Additionally, achieving a system that can account for many length and time scales with minimal task switching or loss of computational efficiency is a requirement. Most systems of interest for appearance and electromagnetic signature design, such as vehicle or aircraft structural components, reside on lengths scales that are 5-10

orders of magnitude above the Mie limit, so improved multiscale approaches to the problem must be used. The hybrid geometric optics – finite element model presented in Chapter 4 of this dissertation represents an attempt at such a highly general, yet rigorous simulation protocol for multiscale light scattering prediction in coatings, composites, and polymeric materials.

1.6. Photon and electron interactions

All matter is composed of dipoles: explicit dipoles, implicit dipoles (through dipole-induced interactions), and dipoles that arise from dipole-induced / dipole-induced interactions.. When an oscillating electromagnetic wave front or field impinges on an object (say, a particle) and passes through that object, dipoles that comprise the object are induced and set to oscillate at a resonant frequency equal to the frequency of the incoming wave. The wave continues to move through the object and the entire particle is oscillating when the wave has finished passing through the particle. As the diploes have been oscillating they are emitting radiation that is of a wavelength complementary to the frequency with which they are oscillating, which equals exactly the wavelength of incoming radiation. These emissions are scattered outward from the particle and are taken to be the scattered electromagnetic radiation field. The emission emitted by a particle is different, from an individual photon perspective, from the incident radiation that causes that scatter event to occur. Indeed, the photon entering a particle is never the same photon exiting, even in the simplest case, as demonstrated by the Feynman diagram of the hydrogen atom shown here in a few pages. First, let us begin with a simple description of a Feynman diagram to elucidate the fundamental interactions between radiation and matter, or photons and electrons.

1.7. Feynman diagrams and light scattering

"All objects are graveyards and nurseries for radiation, but never its permanent abode."

- Craig Bohren[12]

Every interaction between light and matter can be reduced to photon and electron interactions. To decipher and improve our understanding of the odd dance that a photon performs on a surface, it is useful to consider Feynman diagrams for photon and electron interactions, and to relate understanding of these diagrams to real surfaces of interest. According to Feynman's interpretation, there are only three simple actions that light (photons) and electrons can perform: A photon can travel or transport from place to place; an electron can transport from place to place; and an electron can emit or absorb a photon[1]. All three of these interactions may be represented in a Feynman diagram. What's key to understand here is that when an electron absorbs and then reemits a photon, those photons are physically and distinctly different, so even in Feynman diagrams we are making some fairly broad generalizing assumptions.

The first Feynman diagram below (Figure 1-3) shows an electron travelling forwards in time until it reaches a point A and meets up with a photon that is also moving forwards (or "upwards," diagrammatically speaking) in time, and that photon is absorbed by the travelling electron at that point A.

On the second Feynman diagram (Figure 1-4) an electron is travelling forwards in time and at point A *emits* a photon, which is absorbed by a second electron at point B. These diagrams both represent simple cases of electron-photon interactions, that is, the absorption and emission of photons by travelling electrons.

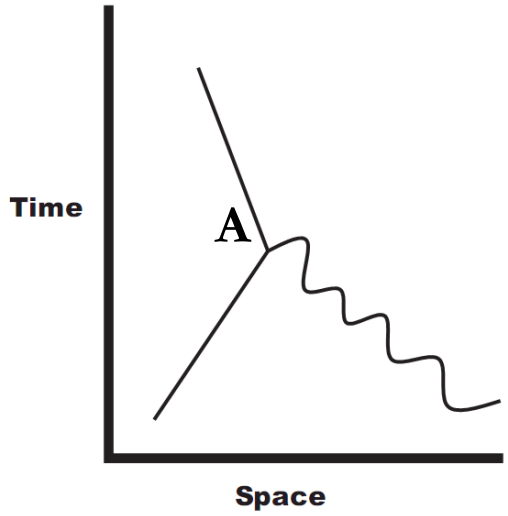

Figure 1-3. Feynman diagram showing an electron (straight line) absorbing or emitting a photon (wavy line) at point A.

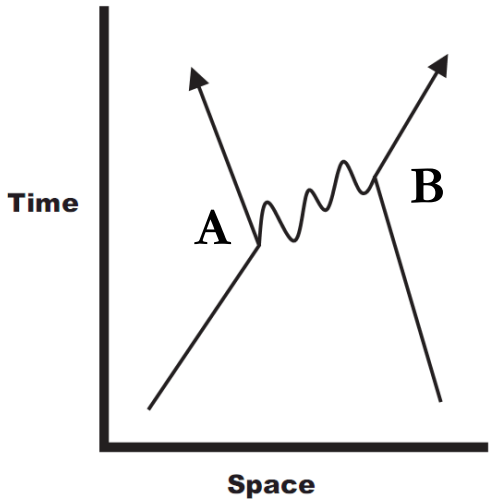

Figure 1-4. Feynman diagram showing an electron (straight line) emitting a photon (wavy line) at point A along with a second photon absorbing the same photon at point B.

The simplest occurrence of light scattering as a single event is a photon entering a physical system, in this case occupied by an electron that is bombarded or collides with the entering photon, and another, different photon leaves the system as a result of that bombardment. When tracking

photons, this is photon or light scattering. In the Feynman diagram shown in Figure 1-5, a photon is absorbed by an electron at A, the electron moves forward with that absorbed energy (equivalent to Planck's constant multiplied by the frequency of the absorbed photon), and at point B a *separate, second* photon is emitted by the electron, and both entities go along on their separate ways. There are really two entirely separate photons involved in this diagram, though physicists and laymen alike commonly "reduce" the complexity of the problem to indicate a single photon scattering "off" or "by" the electron.

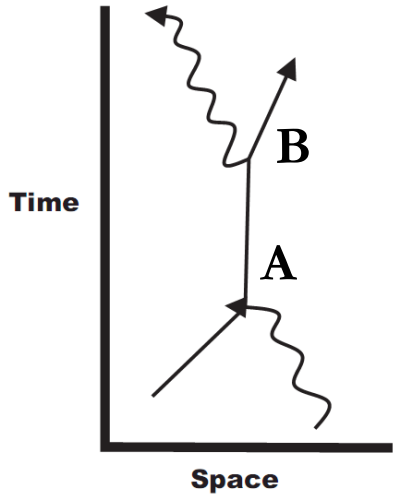

Figure 1-5. Feynman diagram showing an electron (straight line) absorbing a photon (wavy line) at point A, before traveling forwards in time and emitting a second, different photon at point B.

In the second simple light scattering Feynman diagram (Figure 1-6), a photon is emitted by an electron at point A, at which point that electron is then technically photon-deficient, before it absorbs another photon at point B. Light scattering is thus a phrase used to define a discrete series of events that occur over a small window of time. While multiple photons can be counted during the sequence of events, prior to and after the event one can locate a single photon and a single electron.

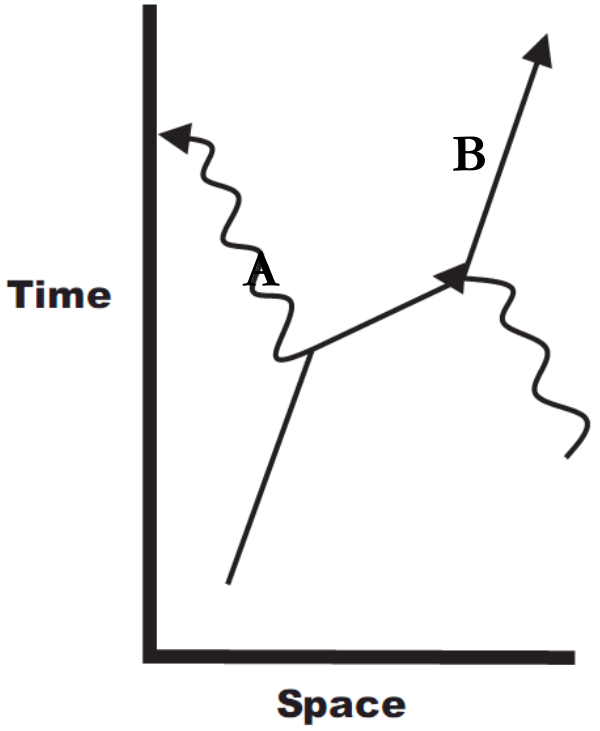

Figure 1-6. Feynman diagram showing an electron (straight line) emitting a photon (wavy line) at point A, before traveling forwards in time and absorbing a second, different photon at point B.

There is another possible, yet peculiar, case that one can draw with a Feynman diagram, where an electron emits a photon at point A and travels to point B, where it absorbs another photon. However, the travel from A to B is backwards in time. This time-travelling electron must have a positive charge to fundamentally exist, and so it's termed a *positron*, and it's a quick and easy example of an anti-matter particle. This positron example is not just for the sake of novelty; rather, it serves as a reminder that there is a possibility of all of the events that can possibly occur (and, indeed, all do occur!) within a material. The above diagrams illustrate all of light scattering phenomena using the most basic and fundamental processes. Stated another way, A and B are positron/electron collision points, where annihilation occurs and radiation is emitted as a photon.

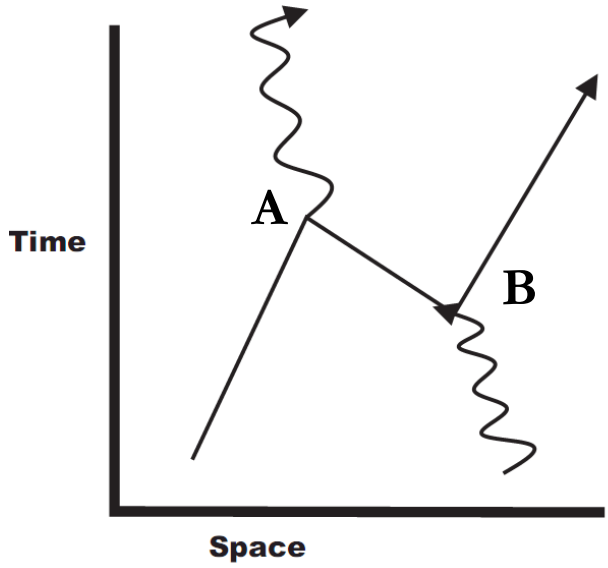

Figure 1-7. Feynman diagram showing a positron (straight line) travelling between points A and B.

And yet, Feynman diagrams for electrons and photons do little to shed any real or practical insight into electromagnetic radiation scattering that is happening on a material surface or at an interface in a bulk material. In order to gain insight here it is necessary to scale up the Feynman diagrams from an electron to an entire (!) hydrogen atom. The diagram in Figure 1-8 fixes a proton in Cartesian space and observes its paired electron as it oscillates around the proton.

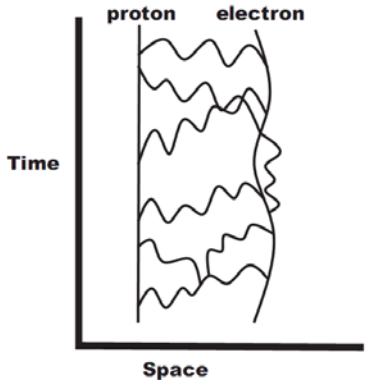

Figure 1-8. Feynman diagram of a hydrogen atom: an electron oscillates about a proton arbitrarily fixed in space. The electron is stabilized by the rapid and continuous exchange of photons (wavy lines) between the proton and the electron.

It's clear from the diagram that a great many random photon exchanges (or photon-electron "connections," indicated by the wavy lines) appear to be holding the electron in place, and indeed, this is the case. In the presence of an incoming photon, shown in Figure 1-9, the photon strikes the "outer shell" electron, and is absorbed by the electron (and, really, the entire hydrogen atom).

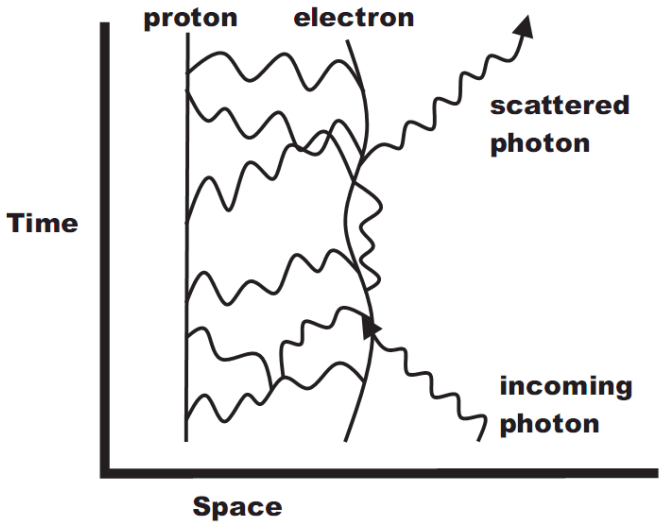

Figure 1-9. Feynman diagram of a hydrogen atom scattering an incoming photon: the outgoing scattered photon is an entirely different photon than the incoming photon.

After a finite amount of time has passed, a new photon is emitted from the hydrogen's electron as a scattered photon, yet *it is not the same photon that was absorbed by the electron an instant ago.* This is a scattered photon, and the simplest example of a photon striking a real material (albeit a tiny hydrogen atom). This simple process gets repeated a countless number of times in a real scattering situation. The combined scattering of light by many electrons is the phenomenon that accounts for the partial reflection in a layer of glass, as well as countless other familiar phenomena.

1.8. Direct versus inverse scattering approaches

Besides being able to predict the electromagnetic radiation behavior of complex composite materials that have features undetectable by the human eye, the question of direct versus inverse scattering formalism arises naturally when considering full system approaches to electromagnetic radiation scattering that involve the atmosphere, the surface of the material, the bulk material itself and any inclusions or heterogeneities in it, as well as the underlying substrate if applicable. The goal of many simulation approaches, especially when the simulated result is easily measurable (such as reflectance, color, emission, etc.) is to arrive at an ideal inverse case scenario, that is, a system is devised such that a novel material may be scanned, measured, or otherwise analyzed empirically in a laboratory setting and the output from such analysis may be interpreted via an inverse problem formalism in order to provide complex and detailed information about the sample.

In practice, properly applied inverse methods tell the experimenter information about an unknown sample. To develop more complex inverse methods, however, first a wide range of often disparate direct methods must be solved for. In a direct method approach to electromagnetic radiation scattering problems, the materials to be studied are defined in every way, geometrically, physically, and materially, and scattering results are calculated from that physical system that is represented in a modeling environment. Once a large enough range or set of direct problems has been solved for, the matrix of results may be statistically or numerically analyzed to produce or yield an improved inverse formalism through mathematical model development or instrumental design.

The bulk of the literature in this field is concerned with direct methods. Although inverse formalism development is the more scarce approach, it can often be used in more interesting ways than then the direct method counterpart. Designing materials that selectively absorb a spectral band of wavelengths or the design of finely engineered surfaces that scatter radiation predominantly in

one directional steradian from the surface are two recent examples of unique inverse solutions to the light scattering problem[13].

As mentioned, many interesting applications are provided by the inverse solution where one wants to measure the electromagnetic signature of an object or surface at a certain wavelength or range of wavelengths, and subsequently deduce information about that object from the resulting electromagnetic signature. While the application of inverse methods will generally yield valuable information about an object, the bulk of simulation theory and design is applied to the direct, or forward, application. Thus, it is prudent that simulation precede experimentation or prototyping, not only to provide general "lay of the land" guidance and property surface response maps, but also to assist in early iterations of inverse method development. As material selection becomes more advanced, and as these advanced materials become increasingly expensive, it will benefit the researcher to apply *in silico* computational methods to their project planning before materials and labor hours are needlessly expended in a physical laboratory setting. In this sense, computational methods are truly a green science that is being increasingly exploited across many fields and disciplines of science and engineering. The ideal relationship between experimentation and computational simulation is a symbiotic feedback loop, where simulation steers experimentation, method, and material development, and experimentation validates and improves the developing simulation approaches.

In many research situations simulation should precede experimentation. In the case of electromagnetic signature, for example, it is simple and straightforward to measure the electromagnetic response of a physical object or surface, but this is a reactive or responsive procedure and informs the user of information related to the sample only in as much depth and detail as the inverse method applied to that analysis was evolved technologically. Information is usually lost when applying an inverse method to experimental results. In other words, the

information gained about a sample after a strict empirical measurement is only as valuable or detailed as the inverse method that developed the analytical tool. This is only a one-off process, as well, so that the information obtained is useful or valid for only one specific physical specimen. There is no preternatural knowledge gained from the experiment. Simulation allows the materials scientist, composites engineer, or coatings formulator to fully explore a unique design space that may consist of highly costly or time-consuming variables, before expending physical resources on the task.

In that light, the purpose of this work is to broaden and expand the available knowledge concerning the light scattering behavior of composites, plastics, and surfaces that have at least one dimension on the nanoscale. These can range from finely polished or sandblasted plastic surfaces, such as simple epoxies or polyurethanes, to complex nanocomposite materials having varying degrees of anisotropy, isotropy, and randomness in their bulk inclusions or on their surfaces. To steer the state of the art towards more realistic models, the approaches and model formalisms presented here will lend themselves to many types of real materials that may comprise air voids, phase separation, nanoparticles of any shape, or larger particles such as traditional pigments or flakes (mica, color flop pigment). In this regard the models presented exhibit high generality, and may be adjusted to suit a wide range of engineering, scientific, and even biological materials. The inclusion scattering model employed here may even account for 4-dimensional inclusions, that is, scattering behavior of inclusions whose physical or material properties change over time, such as the Ostwald ripening of an air void in a wet polymer curing film or the debonding of a reinforcing fiber or nanoparticle embedded in a composite. The roughening of a surface over time is a 4D property that can be modeled here to simulate the effects of process engineering, deliberate texturing, or photodegradation during service life.

One important aspect of the direct solution that is not commonly stated is its applicability to the investigation of physically intractable problems. These are problems where an exact replication in a physical environment would be difficult if not impossible, but where the solutions and modeled behavior are nonetheless important in making engineering design decisions. An example of this in practice would be the simulated single and dependent scattering regime thresholds within a cluster of closely packed specialty pigments embedded in a polymer resin; it may be difficult and cost-inefficient to replicate that material exactly in a laboratory, but the simulated material system will still offer advice regarding optimum pigment geometry and dimensions, ideal pigment volume concentration for a given effect, and predicted formulation thresholds for the onset of undesirable dependent scattering, where pigment scattering cross sections overlap due to proximity. The astute modeler and materials simulator will continue to seek out situations such as this, where the direct computational solution can assist in making quick design decisions, without having to wait for fully-realized direct or inverse solutions to be developed.

1.9. The Maxwell equations for electromagnetic radiation

No contribution has been more meaningful to the study of electromagnetic radiation than that of James Clerk Maxwell, a Scottish mathematician and physicist who is credited with formulating classical electromagnetic theory with his set of partial differential equations now referred to as the Maxwell equations. Maxwell first presented his equations[14] in a four-part paper, "On Physical Lines of Force," in 1861 and 1862. Many first principles simplifications of light scattering phenomenon, such as Snell's law and Fresnel reflectance functions, are derived from the Maxwell equations, and the most accurate and precise solution to any scattering problem is still the coupled solution to the Maxwell equations, a task that is readily performed on today's modern computers and in commercially-available software packages such as COMSOL[15].

The Maxwell equations most commonly used today are the Heaviside couched Maxwell equations, and are individually referred to as Gauss's law for electric fields, Gauss's law for magnetic fields, Faraday's law, and the Ampere-Maxwell law[16-18]. Each of the Heaviside couched Maxwell equations are commonly shown in both integral and differential form, coupled variously through the divergence theorem and Stokes' theorem.

1.9.1. Gauss's law for electric fields

The integral form of Gauss's law for electric fields states that electric charge produces, intrinsically, an electric field, and the flux or flow of that field as it passes through any closed surface is proportional to the total charge contained within that field. Symbolically, it is written as Equation 1-2.

$$\oint \vec{E} \bullet \hat{n} da = \frac{q_{enc}}{\varepsilon_0} \qquad \text{Equation 1-2}$$

In Equation 1-2, $\vec{E}$ is the electric field vector, $\hat{n}$ is the unit vector normal to the surface, *da* represents an increment in surface area, q_{enc} is the amount of enclosed charge, and ε_0 is the electric permittivity of free space.

The differential form of Gauss's law for electric fields, Equation 1-3, implies that the electric field produced by an electric charge diverges from positive charge and converges upon negative charge.

$$\vec{\nabla} \bullet \vec{E} = \frac{\rho}{\varepsilon_0} \qquad \text{Equation 1-3}$$

In Equation 1-3, $\vec{\nabla}$ is the differential operator del, $\vec{E}$ is the electric field vector, ϱ is the charge density, and ε_0 is the electric permittivity of free space.

1.9.2. Gauss's law for magnetic fields

The integral form of Gauss's law for magnetic fields is given by Equation 1-4, and states that the total magnetic flux passing through any closed surface is zero.

$$\oint \vec{B} \bullet \hat{n} da = 0 \qquad \text{Equation 1-4}$$

In Equation 1-4, $\vec{\mathrm{B}}$ is the magnetic field vector, $\hat{n}$ is the unit vector normal to the surface, and *da* represents an increment in surface area.

The differential form of Gauss's law for magnetic fields is given by Equation 1-5, and implies that the divergence of the magnetic field at any given point is zero.

$$\vec{\nabla} \bullet \vec{B} = 0 \qquad \text{Equation 1-5}$$

1.9.3. Faraday's law

The integral form of Faraday's law is given by Equation 1-6. Faraday's law implies that changing the magnetic flux through a surface induces an electromotive force in any boundary path of that surface, and also implies that a changing magnetic field induces a circulating electric field.

$$\oint \vec{E} \bullet d\vec{l} = -\frac{d}{dt} \oint \vec{B} \bullet \hat{n} da \qquad \text{Equation 1-6}$$

In Equation 1-6, $d\vec{l}$ represents an incremental segment in the surface path being integrated. The differential form of Faraday's law is given by Equation 1-7, and states that a circulating electric field is produced by a magnetic field that changes with time.

$$\vec{\nabla} \times \vec{E} = -\frac{\partial \vec{B}}{\partial t} \qquad \text{Equation 1-7}$$

1.9.4. Ampere-Maxwell law

Finally, the Ampere-Maxwell law, given in its integral form in Equation 1-8 implies that an electric current or a changing electric flux through a surface produces a circulating magnetic field around any path that bounds that surface.

$$\oint \vec{B} \bullet d\vec{l} = \mu_0 \left(I_{enc} + \varepsilon_0 \frac{d}{dt} \int \vec{E} \bullet \hat{n} da \right) \qquad \text{Equation 1-8}$$

In Equation 1-8, μ_0 is the magnetic permeability of free space and I_{enc} is the electric current contained the closed space that is producing the circulating magnetic field. The differential form of the Ampere-Maxwell law is given by Equation 1-9, and states that a circulating magnetic field is produced by an electric current and by an electric field that changes with time.

$$\vec{\nabla} \times \vec{B} = \mu_0 \left(\vec{J} + \varepsilon_0 \frac{\partial \vec{E}}{\partial t} \right) \qquad \text{Equation 1-9}$$

In Equation 1-9, $\vec{J}$ is the electric current density vector that is producing the circulating magnetic field.

The Maxwell equations combine in many ways to solve for practically any electromagnetic problem known to man. The most relevant of these combinations is in forming the wave equation for a propagating electromagnetic wave. The Maxwell equations apply to electric and magnetic fields in matter as well as in free vacuum, so they can be applied to solving real world problems in a relatively straightforward manner. However, the great complexity and sheer magnitude of even the simplest scattering problems usually dictates that a computer code solve the Maxwell equations. In this work, the commercially-available software package COMSOL[15] is used to solve the set of Maxwell equations for various material and geometry combinations.

The wave equation for the electric field strength $E(z, t)$ for the system of a plane wave travelling along the z-axis is derived from the Maxwell equations, and is given in Equation 1-10.

$$E(z,t) = E_0 e^{-\left(\frac{w}{c}\right)kz} e^{i\left(\frac{w}{c}\right)nz} e^{-iwt} \quad \text{Equation 1-10}$$

In Equation 1-10, E_0 is the amplitude of the field strength, n is the refractive index of the medium the wave is travelling in, k is the extinction coefficient, w is the angular frequency of the wave, and c is the velocity of light in the medium. The exponential portion which includes k describes attenuation or dampening of the wave, while the remaining exponentials describe the free propagation of the wave through the material.

The intensity of the electromagnetic wave is proportional to the square of the amplitude, and the intensity decreases over distance when the wave passes through an absorbing medium, given by the relationship in Equation 1-11 known as Beer's law.

$$I(z) = I_0 e^{-\alpha z} \quad \text{Equation 1-11}$$

In Equation 1-11, α is the absorption coefficient defined in Equation 1-12 and z represents the distance travelled in the one-dimensional z-axis direction.

$$\alpha = (4\pi nk)/\lambda_0 \quad \text{Equation 1-12}$$

In the Equation 1-12, λ_0 is the vacuum wavelength of the incident radiation. The optical constants n and k are related to the complex dielectric permittivity, as in Equation 1-13, by the Equations 1-14 and 1-15 for n and k, respectively.

$$\epsilon = \epsilon_1 - i\epsilon_2 \quad \text{Equation 1-13}$$

$$n^2 = (\epsilon_1 + \sqrt{\epsilon_1^2 + \epsilon_2^2})/2 \qquad \text{Equation 1-14}$$

$$k^2 = (-\epsilon_1 + \sqrt{\epsilon_1^2 + \epsilon_2^2})/2 \qquad \text{Equation 1-15}$$

A complete and accurate approach to simulating electromagnetic radiation scattering by objects would treat every scattering event as an interaction between a moving wave front and a dipole object being impinged on, and would solve the Maxwell equations at every physical space and time step throughout the scattering situation. This approach would incur great computational expense, and would become an exponentially more difficult task as the complexity of the system increased. Luckily, assumptions and generalities can be made in many places in EM radiation scattering formalism, so that a very precise scattering model may be devised that treats or fully solves the scattering event with the Maxwell equations only when it is necessary, that is, when an object being impinged by incoming radiation is smaller than or close to the geometric limit, defined always by the incident radiation wavelength.

At many length scales a general particle theory of light may be used and light scattering may be treated by using ray tracing or other geometric approaches where light rays act as photon packets that move in straight lines between collision events. However, when scattering inclusions are of the size order smaller than the incident radiation wavelength the precise solution should be used. Here is a perfect example of the wave-particle duality of light in practice. When incident radiation (light) wavelength is very small compared to the size of the scatterer or object the light photons hit, interact with, or pass through, the interaction may be greatly simplified down to geometric basics and solved for using Snell's law for angle determination and Fresnel reflectance equations for transmission and reflection information. However, at inclusion size dimensions that are near or smaller than the incident wavelength, the particle from the previous case (a photon) now must be treated as a moving

wave front hitting an object. Here a wave approach is much more accurate. Thus, the Maxwell equations should be used to solve for this event.

When an object is larger than the geometric limit defined by scattering problem geometry, approximations may be used, such as the Fresnel approximation or Kirchhoff approximation, although, the accuracy of the final simulation result will be affected by using these approximations. As the size of the object approaches and then becomes smaller than the geometric limit the simulation should switch into numerically exact or finite element solutions to the Maxwell equations for the scattering scenario being solved for.

The hybrid model presented here will allow for size-dependent switching of the scattering algorithm to provide for the most accurate solution for a given problem or material of interest. This hybrid approach utilizes geometric ray tracing to track photons as they enter and travel through a material, and makes heavy use of the Fresnel approximation, where local scattering events are assumed to take place at perfectly flat interfaces. The assumption being made is that if a surface is investigated at the photon length scale, any rough surface or object looks perfectly flat in that photon-local region. In this perfectly or ideally flat surface approximation, incoming photons are scattered at an angle given by Snell's law, with a percent of incident weight absorbed into the surface given by Fresnel's laws. These approximations reduce an otherwise complex scattering problem down to a large and repeated number of relatively simple and straightforward calculations, assuming all the while that scattering surfaces or objects are large compared to the incident wavelength and the size of an individual photon.

There is of course another more fundamental approximation at work here. The quantum electrodynamics treatment of light scattering predicts that light scatters in all directions, even in the Snell/specular case, however the probability of finding a photon outside the specular angle is similar to the probability of finding a particle outside the classic particle-in-a-box thought experiment.

Another underlying assumption inherently incorporated into the ray tracing approach is that a scattered photon is the same as the incident photon, identity-wise; in reality the scattered photons are very different from the incident photons that triggered the scattering event.

1.10. Historical light scattering models

A discussion of light scattering is not complete without a presentation of the historical light scattering models, namely Rayleigh scattering and Mie scattering for particle scattering, and Bennett and Porteus scattering, Kirchhoff scattering, and Davies scattering models for rough surface scattering calculations.

1.10.1. Rayleigh scattering

Rayleigh scattering is the phenomenon of elastic scattering of radiation by usually large ensembles of particles, atoms, or molecules, which are all much smaller in size than the diameter of the incident wavelength (i.e. $\alpha<<1$)[10-12]. Although most commonly observed in gas phase materials, Rayleigh scattering can also occur in solids and liquids. The most famous application of Rayleigh scattering is to describe the blue appearance of the sky on Earth. The degree or intensity of Rayleigh scattering is inversely proportional to the fourth power of incident radiation wavelength ($\sim\lambda^{-4}$). Effectively, this means that shorter wavelengths (blues) are scattered more strongly than longer wavelengths (reds). The result is more scattering by short wavelength radiation in the atmosphere, which results in the common blue sky appearance. Because Rayleigh scattering is predominantly a gas-phase phenomenon, it will have little connection to the surface and bulk scattering solutions presented here.

1.10.2. Mie scattering

Mie scattering theory solves for the scattering behavior of particles on the same order of magnitude as incident radiation[19] (i.e. $\alpha \approx 1$). The computation is quick, and many codes and solutions are available in the literature[10, 11]. A caveat with Mie scattering treatment is that the scatterer should be perfectly spherical in geometry. In practice this relegates Mie scattering treatment to the solution of air bubbles in materials and extremely large ensembles of pseudo-spherical scatterers, where the deviations from perfectly spherical geometry are nullified by the law of averages during the solution. A discretized Mie formalism has been presented in the literature, which modifies the treatment for axisymmetric and irregularly-shaped particles[20, 21].

1.10.3. Bennett and Porteus rough surface scattering

Bennett and Porteus presented a model for the correlation between surface reflectance and gloss and surface roughness for materials with surface roughnesses 50 microinches (1270 nanometers)[22, 23]. The Bennett and Porteus scalar scattering theory model gives a straightforward prediction for reflectance change with surface roughness,

$$\frac{R_S}{R_0} = e^{-(4\pi\sigma_{rms}\cos\theta_0/\lambda)^2} \qquad \text{Equation 1-16}$$

In Equation 1-16, R_s is the specular surface reflectance, R_0 is the total reflectance (including diffuse components), σ_{rms} is the root mean square surface roughness, λ is the wavelength of incident radiation, and θ_0 is the incident angle of the impinging radiation. Croll and Hinderliter have modified the Bennett and Porteus model to account for statistical roughening of a surface [24-28], the treatment of which will be described elsewhere in this dissertation.

1.10.4. Kirchhoff scattering

Kirchhoff scattering gives the general solution to scattering of electromagnetic radiation by a rough surface, and serves as the basis for many advanced or evolved surface scattering models[29, 30]. The Kirchhoff solution is applicable for perfectly conducting, homogenous surfaces where the mutual interaction of surface irregularities, like shadowing and multiple surface scattering, is neglected. Although the Kirchhoff solution works fairly well for smooth dielectric surfaces, in modern coatings and composites science surfaces are rarely perfectly homogenous and flat. The increased emphasis on electromagnetic signature design for real, in-use materials has necessitated the inclusion of surface irregularity interactions. The model developed and presented in this work allows for heterogeneous and dielectric surfaces, and accounts for shadowing and multiple scattering events on the surface.

1.10.5. Davies scattering and Beckmann scattering

The Davies scattering solution was one of the first to make explicit use of statistically rough surfaces, that is, surfaces whose peaks and valleys are described by a continuous Gaussian process statistical distribution and correlation function[31]. Beckmann provided a similar treatment describing the surface as a Markov chain, where the surface is described by a stochastic matrix[32]. Both approaches have contributed greatly to the study of light scatter by rough surfaces, and have served as the basis for many evolved models and mathematical approaches[29].

1.11. Surface light scattering models

Many empirical and analytical first principles models have been produced to simulate and predict the scattering behavior of various surfaces. This section will introduce the reader to some of the more common models for each approach.

1.11.1. Empirical models

Empirical, or phenomenological, models do not make an attempt to predict scattering behavior starting with the basic laws of physics. The goal of an empirical model is to reduce the number of parameters so that easy comparisons between different materials and scattering scenarios may quickly be established. Empirical models typically focus on the most user-relevant aspects of light scattering phenomenon; diffuse and specular reflectance. Five empirical models will be briefly presented and reviewed here; Lambertian reflectance, Phong reflectance, Ward reflectance, Lafortune reflectance, and Ashikhmin-Shirley anisotropic Phong reflectance.

1.11.2. Lambertian reflectance

Lambertian reflectance describes light that is uniformly reflected in all directions. That is, it describes ideal diffuse reflectance behavior. Lambertian reflectance models do not result from the solution of the Maxwell equations; rather, they are approximations derived from the observed behavior of many different materials[33]. The effect of Lambertian reflectance in practice is a material whose diffuse appearance does not change with angle of incidence. The classic example often cited is the diffuse reflectance from Earth's moon.

1.11.3. Phong reflectance and Ward reflectance

The Phong reflectance model was developed for computing the radiance behavior of curved objects in digital rendering applications. Phong reflectance is a popular model that has served as a launching-off point for many models in the digital rendering community. Phong's goal in formulating his reflectance model was to skillfully communicate the 3-dimensional aspects of a rendered surface, and not to accurately simulate light transfer[34]. Phong's approach, while relevant

to the digital graphics community, is therefore not very useful to the applications of electromagnetic signature design and modeling presented here.

Ward's reflectance model is similar to Phong's in execution, though a parameter is introduced to account for the average slope of the microscopic surface roughness[35]. This allows for a prediction of reflection anisotropy at the global scale[33]. While still an empirical method, Ward's reflectance model represents an attempt to add actual material physical properties to a digital rendering and appearance simulation toolset.

1.11.4. Lafortune reflectance

Lafortune reflectance represents another variation on the theme established by Phong. The Lafortune reflectance approach is similar to that of Ward reflectance, in that both introduce physical terms to the model formalism. The Lafortune model is able to represent generalized diffuse reflectance, where the diffuse reflectance lobe exhibits some directionality, and can also predict backscatter of light towards the incident direction, both features that were missing in Phong and Ward models.

1.11.5. Ashikhmin-Shirley anisotropic Phong reflectance

The Ashikhmin-Shirley model of reflectance is yet another variation on Phong's work. This is the first empirical reflectance model in the appearance rendering and surface scattering prediction literatures to include a specific term for Fresnel reflectance[36]. Although the variations on Phong reflectance continue to add physics-based parameters to their formalism, treatment of scatter by real materials, both their bulk structures and their surfaces, is best accomplished through the use of analytical first principles models.

1.11.6. Analytical first principles models

Analytical first principles models attempt to replicate mathematically the complex scattering behavior that occurs on a material's surface, rather than treating the system like a strange black box that can be improved in small steps, as the empirical modelers would have it.

These first principles models apply basic physics and geometric concepts to surface scattering problems, and thus require explicit definition of the surface geometry and material composition. At the very minimum this requires knowing a surface's roughness profile or statistics, as well as the refractive index and extinction coefficient of the material or materials that comprise that surface.

The microfacet distribution model, the family of geometric optics approaches, Oren-Nayar reflectance, and Blinn and Cook-Torrance reflectance are all analytical first principles models that warrant mention in this discussion.

1.11.7. Microfacet distribution

The microfacet distribution approach attempts to represent a statistically rough surface with a distribution of microfacets, such that any point on the surface can locally be simplified to a flat plane that is tilted at some angle. The statistical representation of the entire microfacet ensemble is identical to that of the real surface being studied. The microfacet distribution approach allows for easy implementation of the Fresnel approximation of surface scattering, where each local surface scattering event is reduced to solutions of Snell's law and Fresnel's reflectance function. Indeed, the entire method of geometric optics for surface scattering is founded on the microfacet distribution model.

1.11.8. Geometric optics

The geometric optics approach models surface scattering behavior by reducing any real surface to a discrete or a statistical distribution of microfacets. It is assumed that the size dimensions of the microfacets will be large relative to the incident radiation wavelength. Given a distribution of microfacets overlaid onto a surface, ray tracing and tracking approaches are used in computational scripts to compute the scattering behavior for each incident photon or ray at each microfacet being bombarded by incident radiation. The individual results of the microfacet scattering events are summed to yield the global scattering event result.

When computing the local scattering event results at individual microfacets, two approaches can be applied, representing a choice of either Oren-Nayar reflectance or Blinn and Cook-Torrance reflectance.

1.11.9. Oren-Nayar reflectance

The Oren-Nayar reflectance model was developed in order to more properly simulate the appearance of front-lit matte ceramic objects. These objects, when simulated using Lambertian reflectance assumptions, appear too dark and do not align with empirical color measurements made on those objects. Oren-Nayar methods employ a Gaussian distribution of surface slopes, as in the Ward model, but scattering events at each microfacet are solved for in the diffuse, Lambertian scattering regime[37]. That is, one photon incident on a microfacet will produce multiple, diffusely scattered photons. This is in contrast to the Blinn and Cook-Torrance geometric optics approaches, where strictly specular scattering events are assumed to occur at each of the microfacet-photon interaction sites.

1.11.10. Blinn and Cook-Torrance reflectance

Blinn reflectance[38] and Cook-Torrance reflectance[39] are both popular analytical first principles models for geometric optics scattering simulations. Each assumes that the scattering event occurring at every microfacet is a perfect specular reflection, where one incident photon produces one scattered photon. Both models accurately predict the increase in specular reflectance as the angle of incidence increases.

The Cook-Torrance reflectance model[39] was the first analytical first principles method in surface rendering that made use of the Fresnel function for reflected and transmitted light, and thus made explicit use of the material parameters n and k. The result of this usage was that simulated plastic and ceramic materials had white highlights (when lit with a white light source), while metallic surfaces had highlights the color of the base metal. The presentation of the Cook-Torrance model in 1982 was a benchmark in reproducing real material appearance with computer graphics.

1.12. Volumetric and bulk scattering models

Volumetric, bulk, or inclusion scattering approaches are concerned with the treatment of large ensembles of scattering objects enclosed in a specified volume of material. Examples of such systems are gas bubbles in soda, pigment particles in organic coatings, and heterogeneous phases in copolymer blends. The material that comprises the surrounding matrix volume may be air, so that sand and lunar regolith also may be solved with volumetric approaches. For the purposes of this dissertation, volumetric and bulk scattering is any scattering that does not occur at coating or composite surfaces.

Two treatments to volumetric or bulk scattering deserve further discussion; classic Kubelka-Munk scattering theory, and its extension to a class of multiple layer models for reflection and transmission of radiation through pigmented systems.

1.12.1. Kubelka-Munk theory

Kubelka-Munk theory[40-42] is a popular light scattering prediction method for computing the diffuse reflectance of thin layers of pigments in a surrounding binder or medium such as an organic coating. The description of "thin" here does not apply to the incident wavelength, but rather the diameter of the overall object being studied, i.e. the thickness of the organic paint. Using Kubelka-Munk theory, the reflectance of a paint layer that is adequately hiding its substrate is given by Equation 1-17.

$$R = 1 + \frac{K}{S} - \sqrt{\frac{K^2}{S} + 2\frac{K}{S}} \qquad \text{Equation 1-17}$$

In Equation 1-17, $K = \sum K_i c_i$ and $S = \sum S_i c_i$. K_i and S_i are the fraction of light absorbed and the fraction of light scattered, respectively, per pigment i having unit weight fraction c_i. Values for K and S are generally measured from a series of prepared coating samples with known density, thickness, and material composition.

Although improvements have been made to the Kubelka-Munk model to account for surface roughness[43] and film nonuniformity[44], the theory remains a so-called two-flux theory, as all transport behavior is simplified to an "in-flux" and an "out-flux." In this formalism, material behavior or scattering characteristics besides hiding power and bulk film reflectance are hard to assess.

Dorsey and Hanrahan[45] extended the traditional Kubelka-Munk theory to account for nonhiding layers, so that a value for transmittance (T) is included in the calculations. For a nonhiding coating with thickness d, the reflectance R and transmittance T of the coating is given by Equation 1-18 and Equation 1-19, respectively.

$$R = \frac{\sinh(bSd)}{a\sinh(bSd) + b\sinh(bSd)}$$ Equation 1-18

$$T = \frac{b}{a\sinh(bSd) + b\sinh(bSd)}$$ Equation 1-19

In Equations 1-18 and 1-19, $a = \frac{S+K}{S}$ and $b = \sqrt{a^2 - 1}$. The coating may contain any number of pigments, as long as they are randomly dispersed within the same coating layer, as show in in Figure 1-10. The values *a* and *b* need not be known for the individual pigments included in the layer, as they are measured properties of the entire coating system.

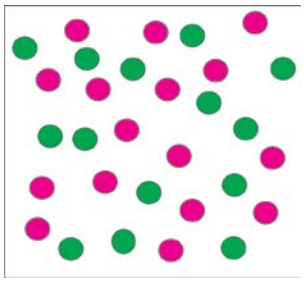

Figure 1-10. Modified Kubelka-Munk formalism allows for mixtures of different pigments within the same coating layer.

1.12.2. Multiple layer models

The Dorsey and Hanrahan variations of Kubelka-Munk theory may be used to predict the reflectance and transmittance of materials containing many layers, with each layer containing a different pigment or mix of pigments, as seen in Figure 1-11.

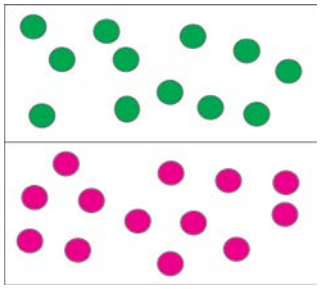

Figure 1-11. Modified Kubelka-Munk formalism allows for mixtures of different pigments within separate, stacked coating layers.

This is performed using composite values of *R* and *T*, as in Equation 1-20 and Equation 1-21.

$$R = R_1 + \frac{T_1^2 R_2}{1 - R_1 R_2} \qquad \text{Equation 1-20}$$

$$T = \frac{T_1 T_2}{1 - R_1 R_2} \qquad \text{Equation 1-21}$$

1.13. Monte Carlo methods and ray tracing approaches

When ray tracing approaches are combined with finite element simulations of scattering behavior where scatter cross section quadrature plays an important role in final scattering results, the very large number of random and repeated events inherent to the problem implies that a Monte Carlo approach may be used to increase the accuracy of the model.

Monte Carlo (MC) simulation is a system where random numbers (i.e. "computational dice-rolls") determine what the input will be for a given variable or set of parameters in an equation that is to be mathematically solved. By definition, the MC methods require more than one dice roll or solution to be used as an input. Thus, statistics plays an integral part of any MC simulation. In light scatter situations, MC formalism can be applied in a variety of areas: the incoming directions and weight of the photons may be pulled or called from a distribution using a dice roll, as can the first contact striking points on a surface. When a photon hits and interacts with a scattering object, of which the scattering distribution or cross section is known, the exiting photon, photons, or photon weights may be determined by a dice roll.

For surface scattering solutions, given a set of statistical surface parameters (roughness and autocorrelation function, for example), a number of statistically identical yet discretely different surfaces may be generated, their scattering behavior may be computed for a set of incident photons, and the results of each individual surface may be averaged to give the predicted scattering behavior

for a set of surfaces having those identical global statistical properties. Thus, the MC formalism generalizes the results from singular to general applicability. In that sense, MC methods are no more than the average of many events that are determined by random or statistical processes.

Lastly, MC practices may be used in devising a statistical scatter model, wherein a photon undergoes a dice roll at each arbitrary step in the material or simulation space to determine whether or not a scattering event takes place. In this case, the placement of inclusions or possible scattering sites is randomized by a MC process, while the overall statistical composition of the materials of interest remains as defined by the user (such as weight or volume percent loading of particles). The benefit of using MC methods is that they inherently become more precise as the number of dice rolls or events is increased. In many cases, a straightforward increase in computation time will improve the statistical significance of the results.

Similar to the central limit theorem in its statistical approach, Monte Carlo-based ray tracing methods use a large number of random and repeated events to simulate a specific process, that is, to obtain sample values for variables of a given problem. Random input values for problem variables are selected from probability distributions for each variable and a computer is used to calculate the results given a range of these initial variable distributions. Previous work with Monte Carlo simulation has predicted the erosion of a coating surface, where terrestrial solar flux was the initiator for polymer segment cleavage and removal [24-26, 28]. Although used for simulations of organic coatings, the generality of the model allows it to be applied to the study of erosion of any material due to a random process, such as rain or wind ablation or the type of water flow experienced by pipelines. The simulation methodology occurred in two separate steps. First, the Monte Carlo method was used to model changes in the surface topography and chemistry of the coating. Second, various published models or finite element methods were applied to the system with its new topography and chemistry in order to predict measurable macroscale properties such as gloss,

fracture toughness, electrical impedance response, UV visible spectroscopy, and solvent wetting angle, all of which are values averaged over a spatial region of the material's surface.

1.14. Finite element solutions of the Maxwell equations

In the case of an object being near or below the geometric limit along one of its length scales, a precise solution of the scattering problem mathematics is required in order to capture the complex wave nature of light in an interaction with an object of that size. Current state-of-the-art computers and finite element simulation programs that are commercially available (such as COMSOL) make it possible to perform accurate finite element solutions to the Maxwell equations for system geometries of any type, and are usually only limited by the researcher's creativity in designing the system to be studied.

The finite element method breaks down a physical system into a map of discrete points, or a mesh of nodes to use finite element parlance. The detailed mathematical solution to a set of governing equations defined by the user is solved at each node, the results are interpolated by various means between the nodes, and the results are summed and presented for the entire system. Finite element methods are a way of solving the complex math governing a system for a reduced set of data points instead of an entire surface. A system solved by finite element approaches is not restricted to any length scale regime. These systems might contain 100 mesh nodes for a spherical scatterer, or millions of nodes for a full-scale simulation of an airplane. Variable mesh engines for many finite element programs allow the user to specify a sensitivity of mesh; the program then automatically applies a fine mesh near areas of heterogeneity, interfaces, surfaces, inclusions, or user-defined areas of importance to improve the calculations around areas that are geometrically complex.

In the case of scattering by inclusions in a statistical scatter method, as presented in this work, the finite element solution may be solved once, either in a stand-alone production run, or at the beginning of a code or script written for the entire scattering problem of interest. The finite element solution presents a scattering profile or cross-section, which can be called by the master scattering script, which transports and tracks photons from scattering event to scattering event using a geometric optics ray tracing approach. This maximizes computational efficiency and increases accuracy.

1.15. A hybrid Monte Carlo-finite element approach to radiation transport simulation

While full solutions of the Maxwell equations can be used through an entire scattering simulation, to optimize computational efficiency a hybrid model will be employed. This combined geometric optics and finite element model makes use of geometric optics or a ray tracing approach to account for photons, and a finite element solution to the Maxwell equations to compute scattering behavior at interfaces or of objects whose size warrants a more thorough treatment to the scattering solution. Thus, in the course of a complete photon trajectory simulation, a photon may enter a material treated as a particle (geometric optics), interact with an inclusion or scatterer as a wave (finite element solutions), and proceed through the material as a particle photon (geometric optics again). This formalism exemplifies the nature of the wave-particle hybrid model for scattering behavior. Photons are accounted for individually or in sets in the code, and exiting photons are collected at positional "detectors" or histogram bins in the simulation space, the fineness of which is arbitrary, and is an adjustable parameter that will affect the precision of the overall simulation.

This hybrid scattering model is robust and exhibits high functional generality and also has many features that can be exercised to increase efficiency or increase precision. This hybrid

scattering approach can be used to accommodate many complex geometries, as well as many simple situations, and some examples of each will be demonstrated in this dissertation.

The simulation protocol could be used to predict scattering behavior of a real specimen that is measureable in a laboratory setting or, probably preferable as far as efficiency and theory development goes, the hybrid model approach may be used to deduce or predict patterns or trends exhibited by a novel material type or family.

1.16. Considerations in electromagnetic radiation transport modeling

There are many assumption and special considerations that should be taken into account during any modeling and simulation endeavor. Topics especially relevant to light scattering simulation are the polarization of light, absorption events, and single versus multiple scattering treatment.

1.16.1. Polarization of light

One important consideration when designing a light scattering model is how to treat or address polarization of light during the simulation. The polarization state of an electromagnetic wave represents the direction of the electric field of the wave. For most applications of electromagnetic scatter simulations the light will be assumed to be unpolarized. In many cases this is not an unsound assumption. Indeed, light from incandescent sources such as slide projectors and tungsten filament light bulbs is unpolarized.

In the case of multiple scattering in composites where many scattering events are bound to occur, the polarizing effect of a scattering event or the incoming polarization of the incident light is lost upon repeated internal scattering. This is due, counterintuitively, to the polarizing effect of a scattering event. Unpolarized light may be transformed into partially polarized light upon scattering.

An unpolarized beam is a mixture of two independent linearly polarized beams of the same intensity (e.g. horizontally and vertically polarized, though these directions may be different in real cases). Except for in the forward and backwards directions these two beam components are scattered differently by a small spherical scatterer. The difference in scattering is greatest at a scattering angle of 90 degrees to the incident normal, where the intensity of the scattered light vanishes for a horizontally polarized beam; thus, at this scattering angle the outgoing scattered light is entirely vertically polarized and is therefore linearly polarized. In this way, randomly, circularly, or unpolarized light may be polarized during a series of scattering event due to randomness effects and the law of averages. In reality, however, one instance of scattering causing polarization is effectively nullified by many scattering events that give no net polarization; the total effect being that most outgoing radiation from a composite that is undergoing electromagnetic radiation bombardment will be unpolarized. In order to simplify the treatment, the models presented here will neglect polarization, although polarization may be accounted for by making minor adjustments to the code and tracking degree and direction of polarization with each ingoing, scattered, and outgoing photon in the simulation.

1.16.2. Absorption effects

For the majority of these models only scattering effects are considered, although absorption effects like coloration and general attenuation through a material via Beer's law may be incorporated into further iterations of the model. Simple adjustments to the model can account for color and appearance effects, as demonstrated in later chapters of this dissertation. The model defines materials by a complex index of refraction and an extinction coefficient, so in many applications absorption may be accounted for by changing one value in the model input parameters. The bulk of the formalism development presented here will predominantly focus on scattering phenomenon,

that is, the geometric redistribution of entered electromagnetic radiation into other directions after a scattering event.

1.16.3. Single versus multiple scattering

Strict single scattering would require a universe devoid of everything except a single solitary scatterer and a beam of light, so the distinction between single and multiple scattering regimes is relative and not absolute. Here, multiple scattering is defined as a single photon engaging in multiple scattering interactions before it leaves the simulation or observation frame of reference. Multiple scattering is accounted for in this simulation scheme. Indeed, one of the metrics that is used for a rough surface analysis is the number of scattering events per tracked photon, which provides a direct measure of scattering multiplicity. In addition to multiple scattering, dependent scattering may be considered here due to the easy incorporation of fe methods, which simplify the computing of very complex scattering geometries by applying generalizing meshes to problem geometries. Dependent scattering results from two or more scatterers lying physically close in space so that the total scattering cross section that is affected by the impinging radiation is smaller than the sum of the individual scattering cross sections were the two entities sufficiently far apart. A separation distance of approximately 1.5 diameters or less is where dependent scattering effects begin to occur. This is an anti-synergistic effect that is a costly concern when formulating paints with high levels of expensive titanium dioxide pigment.

1.17. Industrially-relevant properties determined by radiation transport

Many industrially-relevant properties are determined by radiation transport within a material. Color, gloss, and appearance, as well as yellowness, whiteness, and tint indices are all indicators of

the transport properties of a coating or composite material. Iridescence and interference are two additional phenomena determined by radiation transport in materials.

1.17.1. Color, gloss, and appearance

The first and most general application of electromagnetic signature science and research is in the study of the color and appearance of objects. For example, industrial household paints (architectural house paints) that are formulations of clear polymer matrix resin or binder surrounding a distribution of titanium dioxide pigment particles that scatter light so that opaque color dominates. Regarding nomenclature, color is predominantly a bulk effect, while appearance is often taken to mean the surface effects, that is, how shadowy, shaded, glossy, or hazy the surface of the material appears. This is an important factor in the design of mirrored surfaces and car finishes where a high gloss is desirable. Surface roughness is also related in ways to icephobic properties and cleanability.

1.17.2. Yellowness, whiteness, and tint indices

Related to bulk scattering and color are yellowness, whiteness, and tint indices. Yellowness is often a result of photodegradation of polymer chromophores. These chromophores are usually organic compounds possessing an abundance of saturated bonds that become unsaturated during polymer degradation. The presence of unsaturated double-bonds in the material gives it its yellow color with aging. This degradation of polymer also has a negative effect on the mechanical properties of the material (consider a block of pipe of PVC that has been solarly photobleached and is now yellow and brittle).

1.17.3. Iridescence and interference

Many templated, engineered, or otherwise patterned surfaces are designed to produce iridescence or interference patterns. Coloration produced by partial reflection of white light by two surfaces in close contact is iridescence, for example, oil films on water puddles and peacock feathers, and these phenomena may accounted for in advanced applications of the hybrid model presented here.

1.18. Organization of the dissertation

This dissertation is organized into three main sections as shown in Figure 1-12.; Chapter 2 addresses scattering by a rough surface and various applications and uses of the model. Chapter 3 discusses the internal or bulk scattering by materials containing inclusions such as voids, particles, pigments, fibers, or heterogeneities in phase or composition. Chapter 4 combines the techniques presented in the first two sections to develop a hybrid geometric optics ray tracing and finite element model that is either applied statistically or discretely to predict the optical scattering behavior and electromagnetic signature of a wide range of composites and materials and across nearly any incident wavelength or spectral range.

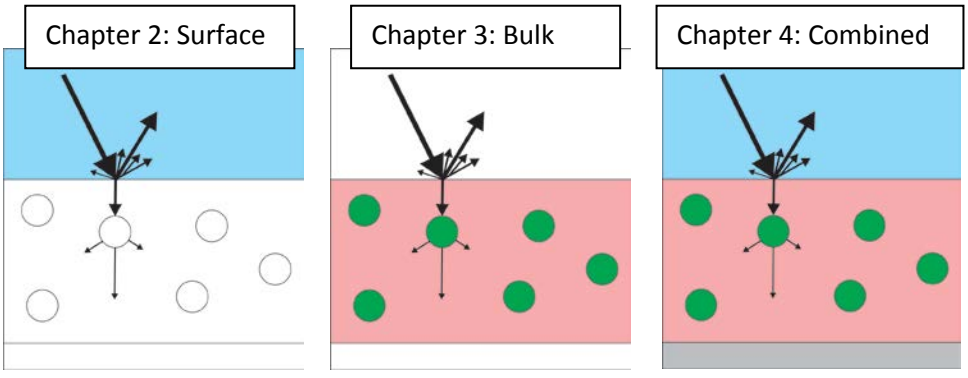

Figure 1-12. The dissertation addresses surface, bulk, and combined scattering.

Chapters 5 and 6 discuss engineering and commercial applications of the models presented here, as well as summarize the contributions and engineering significance of this work. A series of appendices include a transformation matrix that was not in the open literature until now, and annotated bibliography, and a list of publications and presentation given by the author related to this work.

1.19. References

1. Feynman, R.P., *QED: The Strange Theory of Light and Matter*. Princeton Science Library. 1985, Princeton, New Jersey: Princeton University Press.
2. Martelli, F., et al., *Light Propagation through Biological Tissue and Other Diffusive Media*. 2010, Bellingham, WA: SPIE Press.
3. Tishkovets, V.P., *Incoherent and coherent backscattering of light by a layer of densely packed random medium*. J. Quant. Spectrosc. Radiat. Transfer, 2007. **108**: p. 454-463.
4. Tishkovets, V.P., *Light scattering by closely packed clusters: Shielding of particles by each other in the near field*. J. Quant. Spectrosc. Radiat. Transfer, 2008. **109**(16): p. 2665.
5. Tishkovets, V.P. and K. Jockers, *Multiple scattering of light by densely packed random media of spherical particles: Dense media vector radiative transfer equation*. J. Quant. Spectrosc. Radiat. Transfer, 2006. **101**: p. 52-74.
6. *F-18, #13012170, iStockPhoto.com.*
7. *Tank, #18270382, iStockPhoto.com.*
8. Zollinger, H., *Color Chemistry: Syntheses, Properties, and Applications of Organic Dyes and Pigments*. 1987, Weinheim, Germany: VCH.
9. Nassau, K., *The Physics and Chemistry of Color: The Fifteen Causes of Color*. 2nd ed. 2001, New York, NY: John Wiley.
10. Bohren, C.F. and D.R. Huffman, *Absorption and Scattering of Light by Small Particles*. 1983, New York: John Wiley & Sons. 530.
11. van de Hulst, H.C., *Light Scattering by Small Particles*. 1957, New York: John Wiley & Sons, Inc.
12. Bohren, C., *Clouds in a Glass of Beer: Simple Experiments in Atmospheric Physics*. 1987, New York, NY: John Wiley & Sons.
13. Maradudin, A., ed. *Light Scattering and Nanoscale Surface Roughness*. Nanostructure Science and Technology. 2007, Springer.
14. Maxwell, J.C., *On physical lines of force*. The London, Edinburgh, and Dublin Philosophical Magazine and Journal of Science, 1861. **21**(4): p. 161-175,281-291,338-348.
15. COMSOL, *COMSOL Multiphysics RF Module User's Guide*. 2006, Burlington, MA: COMSOL AB.
16. Fleisch, D., *A Student's Guide to Maxwell's Equations*. 2008, Cambridge, United Kingdom: Cambridge University Press.
17. Jackson, J., *Classical Electrodynamics*. 1998, New York, NY: Wiley.

18. Schwartz, M., *Principles of Electrodynamics*. Dover Books on Physics. 1987, New York, NY: Dover.
19. Mishenko, M.I. and L.D. Travis, *Gustav Mie And The Evolving Discipline Of Electromagnetic Scattering By Particles*. BAMS, 2008: p. 1853-1861.
20. Rother, T. and K. Schmidt, *The discretized Mie-formalism - a novel algorithm to treat scattering on axisymmetric particles*. J. Electromag. Wav. Appl., 1996. **10**(2): p. 273-297.
21. Rother, T. and K. Schmidt, *The Discretized Mie-Formalism For Plane Wave Scattering On Dielectric Objects With Non-Separable Geometries*. J. Quant. Spectrosc. Radiat. Transfer, 1996. **55**(5): p. 615-625.
22. Bennett, H.E. and J.O. Porteus, *Relation Between Surface Roughness and Specular Reflecance at Normal Incidence*. J. Opt. Soc. Am., 1961. **51**(2): p. 123-129.
23. Bennett, J.M. and L. Mattson, *Introduction to Surface Roughness and Scattering*. 1989, Washington, D.C.: Optical Society of America.
24. Croll, S. and B. Hinderliter, *A framework for predicting the service lifetime of composite polymeric coatings*. J. Mater. Sci., 2008. **43**: p. 6630-6641.
25. Croll, S.G. and B.R. Hinderliter, *Statistical approaches for predicting weathering degradation and service life*. Prog. Org. Coat., 2006. **55**: p. 75-87.
26. Hinderliter, B. and S. Croll, *Monte Carlo Approach to Estimating the Pjotodegradation of Polymer Coatings*. JCT Res., 2005. **2**(6): p. 483-491.
27. Hinderliter, B.R. and S.G. Croll, *Simualtions of Nanosclae and Macroscopic Propert Changes on Coatings and Weathering*. JCT Res., 2006. **3**(3): p. 203-212.
28. Hinderliter, B.R. and S.G. Croll. *Predicting Coating Failure using the Central Limit Theorem and Physical Modeling*. in *The Fifth International Conference on Advances in Corrosion Protection by Organic Coatings*. 2009. Christ's College, Cambridge.
29. Beckmann, P. and A. Spizzichino, *The Scattering of Electromagnetic Waves from Rough Surfaces*. 1963, Oxford: Pergamon 503.
30. Tsang, L., et al., *Scattering of Electromagnetic Waves: Numerical Simulations*. 2001, New York, NY: John Wiley & Sons.
31. Davies, H., *The reflection of electromagnetic waves from a rough surface*. Proc. I.E.E., Pt. III, 1954. **101**: p. 209-214.
32. Beckmann, P., *A new approach to the problem of reflection from a rough surface*. Acta Techn. CSAV, 1957. **2**: p. 311-355.
33. Dorsey, J., H. Rushmeier, and F. Sillion, *Digital Modeling of Material Appearance*. 2008, New York: NY: Elsevier.
34. Phong, B.T., *Illumination for computer generated pictures*. Commun. ACM, 1975. **18**(6): p. 311-317.
35. Ward, G.J., *Measuring and modeling anisotropic reflection*, in *Proceedings of the 19th annual conference on computer graphics and interactive techniques*1992, ACM Press: New York: NY. p. 265-272.
36. Ashikhmin, M. and P. Shirley, *An anisotropic Phong BRDF model*. Journal of Graphic Tools, 2000. **5**(2): p. 25-32.
37. Oren, M. and S.K. Nayar. *Generalization of Lambert's reflectance model*. in *Proceedings of the 21st annual conference on computer graphics and interactive techniques*. 1994. ACM Press.
38. Blinn, J.F. *Models of light reflection for computer-synthesized pictures*. in *Proceedings of the 4th annual conference on computer graphics and interactive techniques*. 1977. ACM Press.
39. Cook, R.L. and K.E. Torrance, *A reflectance model for computer graphics*. ACM Transactions on Graphics, 1982. **1**(1): p. 7-24.
40. Kubelka, P., *New contributions to the optics of intensely light-scattering material, part I*. J. Opt. Soc. Am., 1948. **38**: p. 448.

41. Kubelka, P., *New contributions to the optics of intensely light-scattering material, part II*. J. Opt. Soc. Am., 1954. **44**: p. 330.
42. Kubelka, P. and F. Munk, *Ein beitrag zur optik der farbanstriche*. Z. Tech. Physik., 1931. **12**: p. 330.
43. Murphy, A.B., *Modified Kubelka-Munk model for calculation of the reflectance of coatins with optically-rough surfaces*. J. Phys. D: Appl. Phys., 2006. **39**(2006): p. 3571-3581.
44. Bierwagen, G.P., *Estimation of Film Thickness Nonuniformity Effects on Coating Optical Properties*. Col. Res. Appl., 1992. **17**(4): p. 284-292.
45. Dorsey, J. and P. Hanrahan. *Modeling and rendering of metallic patinas*. in *Proceedings of the 23rd annual conference on computer graphics and interactive techniques*. 1999. ACM Press/Addison-Wesley.

CHAPTER 2. SIMULATION OF LIGHT SCATTERING BY ROUGH SURFACES

"I want to emphasize that light comes in this form – particles. It is very important to know that light behaves like particles, especially for those of you who have gone to school, where you were probably told something about light behaving like waves. I'm telling you the way it *does* behave – like particles."

- Richard P Feynman[1]

2.1. Introduction

The scattering behavior of electromagnetic radiation by surfaces is an unavoidable material property that is directly responsible for a material's gloss, and contributes to important aspects of the overall color and appearance, electromagnetic signature, and, on the macroscale, the tactile and macrophysical properties of the surface such as texture, smoothness, and the ability to be cleaned. This chapter describes work using 2-dimensional and 3-dimensional ray-tracing models that are used to produce a wide range of property trends that describe the scattering behavior of randomly rough surfaces. This surface scattering simulation will be coupled with a bulk scattering simulation to produce the hybrid multiscale approach presented in Chapter 4. This chapter begins with a discussion of surface light scattering principles, before example output of a 3-dimensional ray tracing model for light scattering by a rough surface is presented. Extension to color and appearance prediction is made where possible.

2.2. Surface roughness and real materials

Most every real surface has a degree of roughness attributed to it, with the exception of a pure liquid, which even then won't be perfectly or ideally flat due to a vapor phase at the interface and atomistic roughness that is inherent to any real surface. For many applications that level of concern is unwarranted and a liquid surface may be considered “perfectly” flat. Diamond polished surfaces have roughnesses of around ten nanometers, while realistic and practical "smooth" engineering surfaces can have roughnesses ranging from tens to hundreds to thousands of nanometers. Besides the scale of surface roughness, which can be measured by a statistic known as rms (root mean square) roughness, the distribution of the surface peaks and valleys is critical to surface scattering behavior as well. There are two measures of peaks and valley distribution that will be considered here. The first is the shape of the distribution of peaks and valleys of the rough surface, which generally is described as being either fractal or Gaussian. The second measure is the autocorrelation length or function which is a measure of how far the peaks are spread out on a rough surface. In choosing a statistical distribution to use for simulations the classic situation calls for a Gaussian distribution. It’s been shown that sandblasted surfaces, photodegraded polymer surfaces, ocean waves, leveling paint that has been freshly sprayed, and other common surfaces are Gaussian in nature[2].

2.3. The four percent reflection scenario

The four percent surface reflection scenario is a good place to begin discussing surface scattering. This scenario supposes a perfectly and ideally flat surface being impinged upon by a ray or incident beam of light. In fact, no surface can be utterly, entirely flat, as even liquid surfaces have

a liquid-vapor interphase at their boundary, which exhibits atomic roughness. For example, Figure 2-1 shows the atomic roughness and interphase present at a simulated water / argon interface.

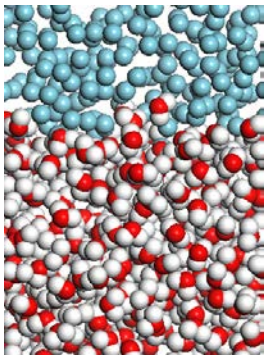

Figure 2-1. The atomic roughness at an interface commonly assumed to be perfectly flat; water under a thick layer of argon gas (picture from author's personal work).

For this scenario we assume a local surface that is perfectly flat, and, in fact, it makes it easier to think of the surface of not even being composed of atoms at all! Imagine a boundary or plane across one direction of this thought-experiment space that is being envisioned. The refractive indices of the materials forming this interface are around 1.0 and 1.5, as in an air/polymer interface. Assume the surface is the topmost surface of a slab of dielectric material, such as a polymer, it doesn't matter what the composition is. In fact, this is an important idea. For this scenario all that matters are the indices of refraction and the extinction coefficients of the materials in the system, as well as the geometry of the system. A detector is placed in the material such that this detector catches and counts any and all photons entering the material; the direction here is irrelevant. Assume a collimated beam of light is impinging on the surface at an angle of θ to the surface normal. This is diagrammed in Figure 2-2.

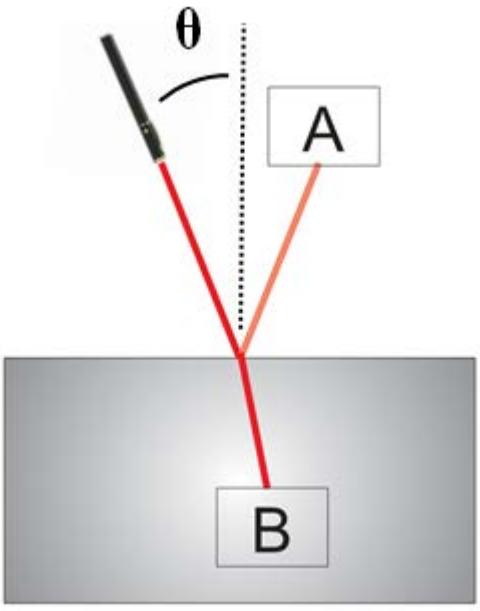

Figure 2-2. The Four Percent Reflection Scenario. Four percent of the photons from the laser reach detector A, the balance reach detector B.

In this scenario some interesting things happen. On average, if we fire a great many number of photons at the surface in this collimated beam, 96 percent of them will hit the detector embedded within the material, while the balance, 4 percent, will strike a detector that is placed outside of the material, above the surface of interest, and at an angle equal to the incident angle, reflected across the global surface normal. This 4 percent reflection is the ideal, maximum, mirror-like specular reflection portion of scattered light that is the product of surface scattering on an infinitely and perfectly smooth surface. It's important to note here that if detectors (photomultipliers) are placed at these locations and the clicks at the detector are recorded when photons hit the photomultipliers; it will become apparent that the clicks are more spaced out chronologically in the specular detector, yet they are the same magnitude of volume as clicks in the bulk material detector. Furthermore, for every 100 photons fired onto the surface, 96 hit the internal detector and 4 hit the external detector, but the clicks are inseparable from each other, a piece of proof here for the particle theory of light,

because if light behaved like a wave here the clicks would decrease in decibel level as "weaker" waves hit the photomultipliers, but this is not the case. In practice this could be demonstrated with a laser pointer aimed at an angle onto a flat surface; a dimmer reflection of the incident laser beam will appear in the specular area where a detector might be expected. What is curious about this experiment is that all that can predicted from this is the *probability* of where photons will go; one can't say with any certainty if a particular photon will embed in the material or end up at the external detector. This is an example where probability and statistics cannot be avoided, and must be incorporated into any thorough treatment of the problem.

Light scattering by a flat surface and the prediction of specularly scattered or transmitted photons is an excellent example of a circumstance in science that is not always repeatable at the individual action or event scale; the experiment produces different results (i.e. reflected or transmitted) when you run the experiment multiple times. All that can be predicted, with any degree of certainty, is that four out of every one hundred photons fired at the surface will reflect specularly; the remainder will be transmitted.

This strange feature of partial reflection forced physicists away from making absolute predictions into a realm of science that is based on probability, statistics, and distributions of event occurrence likelihood. There is no way to predict whether a specific photon will be reflected or transmitted by a surface; we can only state the probability of one event or the other occurring. This hold true for internal scattering events as well. The scattering profile for a pigment, for example, may be calculated using finite element approaches, but that represents a moving, statistical, wave front impinging and passing through the pigment, not a single photon scattering "through" or "off" or being scattered "by" a pigment. In truth, even surface reflected photons don't really "bounce" off the surface in a perfectly elastic collision; photons travel from one electron to another in a complex

dance (to paraphrase Feynman[1]), or chain of events, and reflection and transmission processes are the sum total of these events taken and represented as a simple and single event.

Indeed, even if a photon could be tracked individually as it approached and interacted with a surface, one would see that another, different, and entirely new photon exits the surface. So the assumptions are more than just probability-based; one actually has to (wrongly) assume that a photon keeps its original identity as it is passed from electron to electron in a material. Luckily, this assumption has little impact or meaning to large scale events that occur above the atomic length scale.

2.4. Surface scattering theory and analysis: radiative properties

Light incident on a surface is either reflected or absorbed, the latter of which can ultimately result in transmission in some cases. The bidirectional reflectance distribution function, or BRDF, is a numerical format used to describe and quantify the angular weighting of reflected and scattered light in a surface scattering event, and is given by Equation 2-1[3].

$$\rho''_{\lambda}(\Omega_s, \Omega_i) = \frac{\pi}{\cos\theta_s}\left(\frac{d\Phi_s}{d\Omega_s} / \frac{d\Phi_i}{d\Omega_i}\right) \qquad \text{Equation 2-1}$$

In the BRDF equation, θ_s is the angle of scattered light, Φ_i and Φ_s are the incident and scattered radiant powers and Ω_i and Ω_s are the incident and scattered solid angles, all respectively noted.

The bidirectional reflectance can be integrated over the entire hemisphere that resides on the

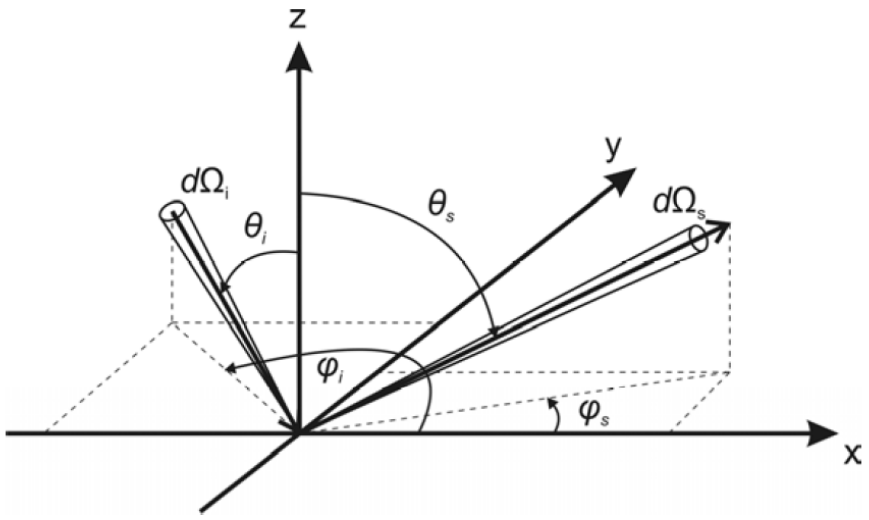

Figure 2-3. The BRDF defined over a flat x-y plane. The incident (subscript *i*) and scattered (subscript *s*) light portions are located in the solid angles dΩ, and are specified by the zenith (θ) and azimuth (φ) angles.

surface above the scattering event to yield the directional hemispherical reflectance, defined in Equation 2-2[3].

$$\rho'_\lambda(\Omega_i) = \frac{1}{\pi}\int_0^{2\pi} \rho''_\lambda(\Omega_s, \Omega_i)\cos\theta_s d\Omega_s \qquad \text{Equation 2-2}$$

The directional hemispherical reflectance is a simple way to assess and quantify the general diffusive scattering properties of a surface, as well as the materials absorbance, as one can readily define a direction hemispherical absorbance as in Equation 2-3.

$$A'_\lambda(\Omega_i) = 1 - \rho'_\lambda(\Omega_i) \qquad \text{Equation 2-3}$$

2.5. Surface roughness terminology

Every surface may be defined as having surface characteristics that are either isotropic (without direction) or anisotropic (with direction)[2, 4, 5]. Isotropic surfaces are generally characterized as being random. These surfaces have no distinguishable "lie" or "direction" to their surface features. Examples of isotropic material surfaces are polished metals, common polymer and paint surfaces, and surfaces that have undergone a significant amount of roughening due to weathering, photodegradation, or any process of chemical etching or treatment that is performed without a mask or template. Anisotropic surfaces have a recognized direction or pattern to their surfaces. This class of surfaces includes surfaces that are generated by certain machining processes, or materials that have a directionally-preferential exposure or weathering regime, as well as surfaces that are sanded or brushed in a prescribed number of directions such that a continuous pattern is formed. Surfaces with well-defined texture as can be found demonstrated with self-assembling polymers that wrinkle or phase separate under certain specific processing conditions.

2.6. Specular reflectance: closed form solution

The use of reflectance measurements embodies a non-destructive method of assessing the progression of surface damage to a coating. Coatings are often employed to improve or change the appearance of a substrate, so service lifetime in this case may be determined by, and in some applications defined by, deterioration in gloss. A correlation between the parameter used to define coating failure and change in reflectance could be employed to infer the estimated remaining lifetime of the coating via gloss measurement. Standardized gloss measurements average reflectance over a spectrum of visible wavelengths, however, specular reflection is, in general, spectrally nonselective.

The specular reflectance based on the model of Bennett and Porteus[6] is given in Equation 2-4 for normal incidence:

$$R_s = R_0 \exp[-(4\pi\sigma)^2/\lambda^2] \quad \text{Equation 2-4}$$

In Equation 2-4, λ is the wavelength of incident radiation and σ is the standard deviation of the surface from its mean level. The central limit theorem yields the standard deviation in the surface topology and predicts how surface roughness progress with time:

$$Roughness = \sigma_{rms} = \varepsilon\sqrt{N} = \varepsilon\sqrt{Kt} \quad \text{Equation 2-5}$$

In Equation 2-5, ε indicates the characteristic size of a molecular fragment that is removed, *N* is the number of events, *t* is time, and *K* is the rate parameter associated with the quantum efficiency for removal for that material[7, 8]. Equation 2-5 may be further simplified to:

$$\sigma_{rms} = \varepsilon\sqrt{Kt} = \sqrt{\varepsilon^2 Kt} = \sqrt{kt} \quad \text{Equation 2-6}$$

For Equation 2-6, *k* is the new rate parameter and has units of (length)^2/time. Applying Equation 2-6, which relates the roughness to time, into Equation 2-4 generates a formula that shows the reflectance as a function of the exposure time:

$$R_s(t) = R_0 \exp\left(-\left(\frac{4\pi}{\lambda}\right)^2 ({\sigma_{initial}}^2 + kt)\right) = R_0 \exp\left(-\left(\frac{4\pi\sigma_{initial}}{\lambda}\right)^2\right) \exp(-\left(\frac{4\pi}{\lambda}\right)^2 kt)$$

Equation 2-7

Scaling the reflectance as a function of time to the initial measured reflectance gives Equation 2-8:

$$\frac{R_s(t)}{R_s(t=0)} = \exp\left(-\left(\frac{4\pi}{\lambda}\right)^2 k't\right) \qquad \text{Equation 2-8}$$

In this case, the central limit theorem in combination with the approximation of Bennett and Porteus yields a simple exponential decay of reflectance with weathering exposure. The initial unweathered reflectance (R_s/R_0) of the coating material could be used to arrive at an estimate of the starting roughness.

The same methodology can be applied to coatings composed of multiple phases[8, 9]. We will consider here the case where the secondary phase is harder than the matrix and degradation only occurs in the polymer, the softer phase. The reflectance is given by Equation 2-9:

$$R_s = \left(1 - f_{pigment}\right)R_o^{polymer}\exp[-\left(4\pi(cos\theta)\sigma_{polymer}\right)^2/\lambda^2]$$
$$+f_{pigment}R_o^{polymer}exp[-\left(4\pi(cos\theta)\sigma_{pigment}\right)^2/\lambda^2]$$

Equation 2-9

In Equation 2-9, *f* is the projected area fraction of the subscripted material. For a material like a coating that has a projected area fraction that evolves with time, another correlation for projected area fraction needs to be given or measured. Conversely, the method allows an estimate of the projected area fraction as a function of time to be derived from the reflectance of the surface and knowledge of the substituent's reflectances, given in Equation 2-10:

$$\frac{R_s}{R_t} = \left(1 - f_{pigment}\right) \exp\left[\frac{-\left(4\pi\sigma_{polymer}\right)^2}{\lambda^2}\right] + f_{pigment} \frac{R_0^{pigment}}{R_0^{polymer}} \exp\left[\frac{-\left(4\pi\sigma_{pigment}\right)^2}{\lambda^2}\right]$$

Equation 2-10

2.7. Applying surface scattering simulation to degradation simulation results

The Monte Carlo degradation simulation predicts surface erosion over time, including the exposure and subsequent loss of 300 nanometer diameter pigment particles near the surface, as seen in Figure 2-4. In this simulation, ablation of surface polymer material was more labile for removal by three orders of magnitude than that of pigment material[10].

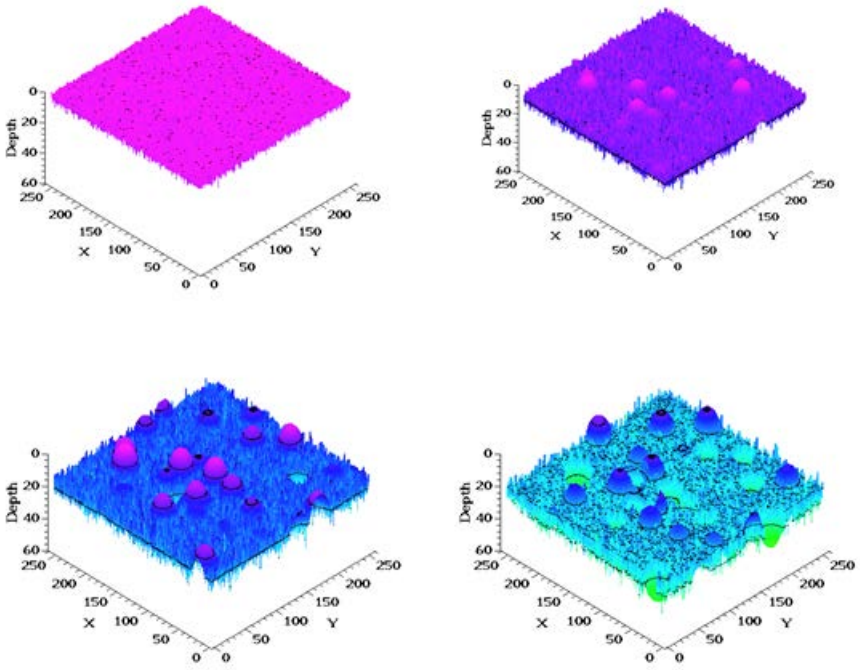

Figure 2-4. Output from the Monte Carlo degradation simulation. The surface of the coating is roughened as coating erodes and exposed pigment particles are removed. Units shown are 10s of nanometers and are expanded in the Z-axis.

The simulation predicts a short period of time when the distribution of exposed pigment particles is not evenly distributed between all degrees of exposure (the extremes being a pigment particle just tangent to the air-exposed surface and a pigment particle barely held at its beltline just prior to release from the coating). The exposed pigment area increases initially as the polymer-rich topmost layer of coating erodes, as seen in Figure 2-5. Once a statistically representative cross section of the interior of the coating is exposed, however, pigment area fraction remains statistically constant.

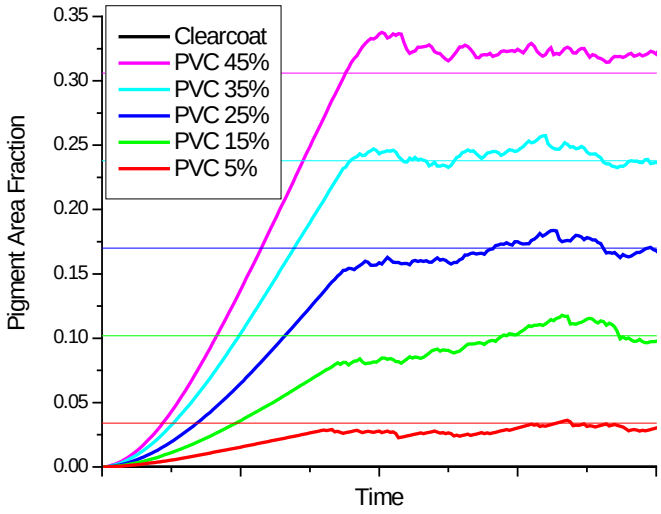

Figure 2-5. The Monte Carlo degradation simulation predicts an exposed pigment area that increases initially before leveling off. Notice that the exposed area fraction is always less than the pigment volume concentration.

Figure 2-6 shows the results of Fresnel reflection coefficient calculations applied to two of the surfaces generated in the Monte Carlo photodegradation simulation. To do so, an effective surface refractive index is computed for each surface, using simple averaging of the surface fractions of pigment (n=2.4) and polymer (n=1.5). Slight changes can be seen in the reflectance at near-

normal angles of incidence, where increasing pigment concentration in the material (and thus on the surface) leads to higher reflectivity.

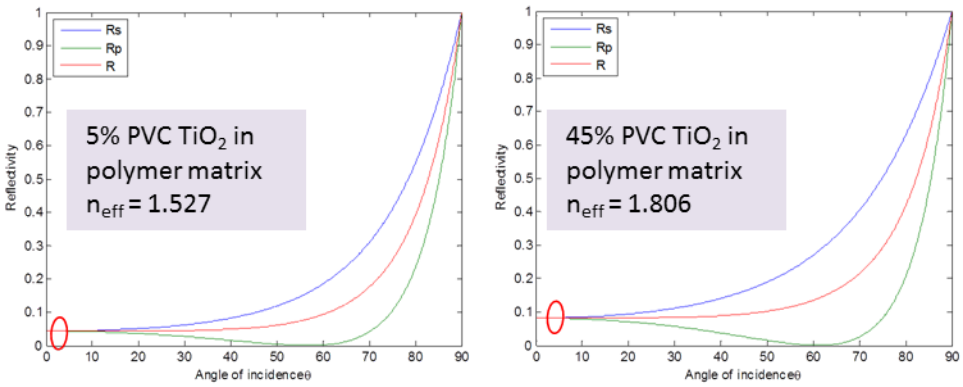

Figure 2-6. Predicted reflectance of two simulated photodegraded surfaces containing mixtures of polymer and titanium dioxide pigment. Reflectance at near normal incident angles is increased as the effective refractive index of the surface increases due to increasing pigment portion. Rs, Rp, and R, are the reflectivities of s-polarized, p-polarized, and their average-value circularly-polarized light, respectively.

2.8. Geometric optics ray tracing simulations of rough surface scattering

For 3-D simulations of surface scattering the geometric optics ray tracing approximation is used, where individual photons are tracked as they propagate or transport from one physical location to another physical location in a given simulation space. The transport paths of the individual photons are assumed to be linear in nature when a photon is travelling between two points. This paradigm embodies the particle theory of light, which works very well when problem geometries are very large compared to the incident wavelength of radiation.

To simplify matters and reduce the approximation to a series of relatively straight-forward calculations, the Fresnel approximation is employed at photon/surface interaction points, where every local photon strike point (a surface or interface of any kind) is assumed to occur at a perfectly flat surface. In fact, this approach reduces every scattering event to a straight forward specular

reflection event, where the outgoing photon's trajectory angle is determined by Snell's law, and the proportion of light absorbed or reflected internally is provided by Fresnel's reflectance equations.

2.8.1. Snell's law

The solution of the Maxwell equations at a perfectly flat surface results in Snell's law, Equation 2-11, for the angles of incidence and refraction when radiation impinges on the interface between two materials having two different refractive indices, such as air and water or air and polymer. The solution to Snell's law is straightforward and easily incorporated into a numerical computer code.

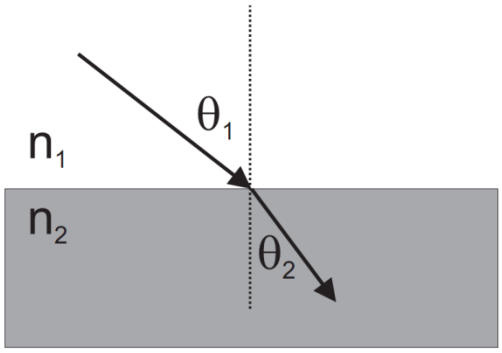

Figure 2-7. Geometry of a simple Snell's law calculation.

$$\frac{\sin\theta_2}{\sin\theta_1} = \frac{n_1}{n_2} \qquad \text{Equation 2-11}$$

2.8.2. Fresnel's reflectance equations

The solution of the Maxwell equations also provides the fractions of light reflected and transmitted at scattering interfaces, in a set of equations known as Fresnel equations, given as Equation 2-12. The Fresnel equations are complicated, algebraically, but only require careful number crunching to solve for the scattering event when values of incident angle and material refractive index and extinction coefficient are provided. The solution to the form provided below gives $R_{specular}$,

the portion of reflected radiation that leaves the surface without being transmitted. The portion transmitted into the material n_2 is therefore 1-$R_{specular}$. The form presented here is from Dorsey et al.'s Digital Modeling of Material Appearance[11].

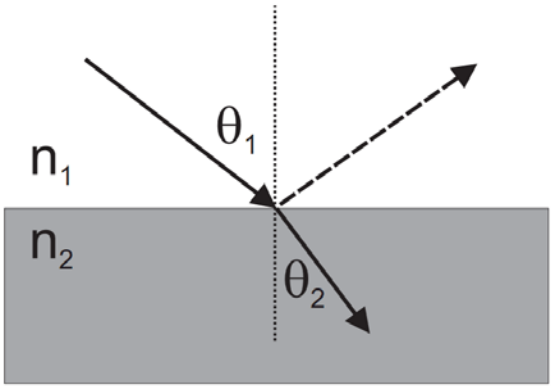

Figure 2-8. Geometry of a simple Fresnel reflection coefficient calculation.

$$R_{specular} = F(\theta) = 0.5\left(1 + \frac{a^2+b^2-2\sin^{-1}\theta\tan\theta+\sin^2\theta\tan^2\theta}{a^2+b^2+2\sin^{-1}\theta\tan\theta+\sin^2\theta\tan^2\theta}\right)\left(\frac{a^2+b^2-2\cos^{-1}\theta+\cos^2\theta}{a^2+b^2+2\cos^{-1}\theta+\cos^2\theta}\right)$$

$$2a^2 = \sqrt{(n^2-k^2-\sin^2\theta)^2+4n^2k^2} + n^2 - k^2 - \sin^2\theta$$

$$2b^2 = \sqrt{(n^2-k^2-\sin^2\theta)^2+4n^2k^2} - (n^2 - k^2 - \sin^2\theta) \qquad \text{Equation 2-12}$$

2.8.3. Generating a rough surface

To compute 3D surface scattering behavior for a set of statistical surface parameters (rms roughness and autocorrelation length), a surface is generated, initial strike points or locations are chosen, a number of photons and photon starting positions are defined, photons begin to be fired at the surface, and the fired photons are tracked as they move, progress, or scatter through the material using the above mentioned formalism. Because statistical parameters are defined and discrete surfaces are generated from those parameters, improved results can be obtained by generating multiple surfaces that are each discretely unique yet statistically identical; scattering simulations are

performed on each unique surface and the results are averaged to give scattering properties for a general surface defined by the initial statistical parameters rms and acf. This is an analytical first principles model that incorporates Monte Carlo randomization into its final result.

2.8.4. Defining and generating Gaussian random rough surfaces: unidirectional 1-D Gaussian rough surface

A random rough surface defined by the function $z = \zeta(x, y)$ is described statistically by the height probability function, $p(\zeta(x, y))$, and the autocovariance function, $C(\tau)$. The height probability functions describes the average peak and valley deviation about an average reference level, while the autocovariance function describes the laterally spread, placement, or frequency of the peaks and valleys that comprise a rough surfaces.

Thomas[2] has shown that the Gaussian assumption is valid in most cases, provided the roughness at any single surface point is not the result of a purely one-off event. This holds true for most common and real surfaces such as coatings, polymers, and composites that experience normal service conditions, such as photodegradation, and handling (i.e. abrasive wear).

The Gaussian height probability function is defined by Equation 2-13.

$$p(\zeta) = \frac{1}{\sigma\sqrt{2\pi}} e^{\frac{\zeta^2}{2\sigma^2}} \qquad \text{Equation 2-13}$$

In Equation 2-13, σ is the root mean square height, which is equivalent to the standard deviation of the collection of surface heights. The autocovariance function is assumed to be Gaussian in this dissertation, and is given by Equation 2-14.

$$C(\tau) = [\zeta(x_1)\zeta(x_2)] = \sigma^2 exp\left(-\frac{|x_1 - x_2|^2}{\tau^2}\right) \qquad \text{Equation 2-14}$$

In Equation 2-14, x_1 and x_2 are surface points and τ is the correlation length determining the distribution of separations between these surface points.

One-dimensional Gaussian rough surfaces may be generated using the Spectrum method outlined by Thorsos[12]. A Fourier transform is applied to the autocovariance function above to yield the power spectral density function, Equation 2-15.

$$W(k_x) = \mathrm{F}_T[C(x)](k_x) = \frac{\sigma^2\tau^2}{4\pi}\exp(-\frac{k_x^2\tau^2}{4}) \qquad \text{Equation 2-15}$$

F_T indicates the Fourier transform in Equation 2-15, and k_x is the spatial frequency domain variable. The power spectral density function, $F(k_{xm})$ relates to the discrete Fourier transform of the surface height function through the relationship defined in Equation 2-16.

$$F(k_{x_m}) = 2\pi L\sqrt{W(k_{x_m})}\begin{cases} \frac{N(0,1)+iN(0,1)}{\sqrt{2}} & m \neq 0, \frac{N}{2} \\ N(0,1) & m = 0, \frac{N}{2} \end{cases} \qquad \text{Equation 2-16}$$

In Equation 2-16, k_{x_m} is defined as $2\pi m/L$, where L is the length of the surface and N(0,1) is a normal distribution with unit variance and zero mean value. The final Gaussian height function, $z = \zeta(x)$ is now realized by taking the discrete inverse Fourier transform of k_{x_m}.

$$z = \zeta(x) = \frac{1}{L^2}\sum_{m=-N/2}^{m=\frac{N}{2}-1} F(k_{x_m})\exp(ik_{x_m}x) \qquad \text{Equation 2-17}$$

Using Equation 2-17, one-dimensional Gaussian surfaces are able to be generated. Figure 2-9 shows the surface profile of a Gaussian surface having rms of 10 nanometers and autocorrelation length of 1 micron. The surface was generated along 100 microns of non-rough path length, using 1024 date points for surface construction.

Figure 2-9 also displays some statistics of the generated rough surface. The height distribution is plotted against a standard Gaussian profile of height distributions, and the actual rms height is calculated (0.010448 microns, compared to 0.01 microns entered into calculation). The rms height is by definition equivalent to the standard deviation sigma value for the surface, while the mean surface height for this example is -0.00178 microns, or 1.78 nanometers. Skewness of the height distribution is slightly positive (0.054) indicating that the right tail of the distribution is longer than the left (i.e. the distribution is right-skewed). The kurtosis of the surface is 2.758, and represents the pointedness of the distribution. In this case the kurtosis is strong, and is representative of a leptokurtic distribution with large peaks around the mean and thin peaks around the tail. The autocorrelation function is plotted against the lag length, and indicates an actual correlation length of 1.0264 microns, compared to the value of 1.00 micron entered into the calculation. The difference between the generated surface points and the input (model) parameters is given by the comparison between black (data) and red (model) traces.

2.8.5. Defining and generating Gaussian random rough surfaces: bidirectional 2-D Gaussian rough surface

The mathematical process of defining and generating a 2-D rough surface is similar to the 1-D case presented earlier; however the math is now extended in two directions, typically x and y, and the distribution properties are interpolated to fill in the heights (presumably z-axis values) in the x-y plane.

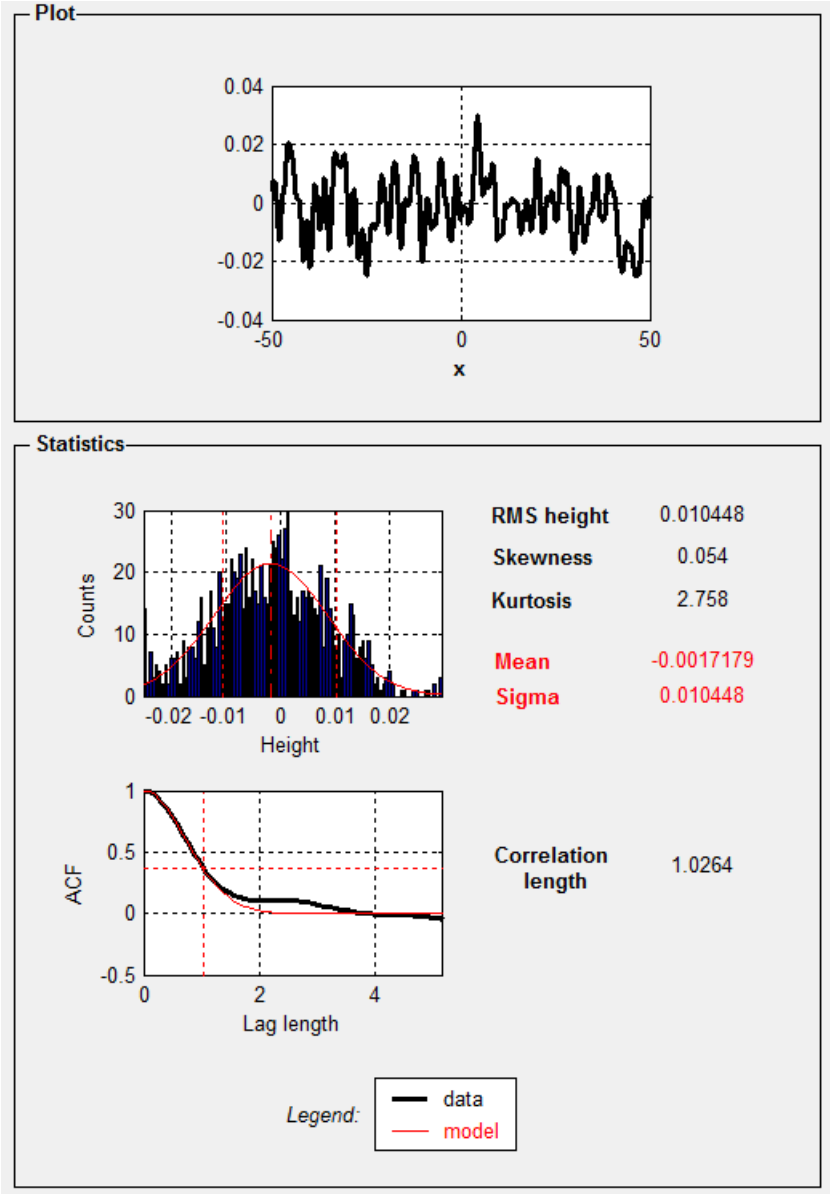

Figure 2-9. Representative output and surface statistics in a 1-D Gaussian rough surface generation. The autocorrelation length was entered as 1 micron, and the rms roughness was entered as 10 nanometers.

Two-dimensional rough surfaces are defined as $z = \zeta(x, y)$ and are characterized by having correlated height distribution function and autocovariance function, termed HDF and ACF, respectively.

The HDF for a Gaussian surface is given by Equation 2-18.

$$HDF = p_h(\zeta) = \frac{1}{\sqrt{2\pi\sigma^2}} \exp(-\frac{\zeta^2}{2\sigma^2}) \quad \text{Equation 2-18}$$

The ACF for a 2-D Gaussian surface is given by Equation 2-19.

$$ACF = C(x,y) = exp\left(-\frac{x^2}{\tau_x^2} - \frac{y^2}{\tau_y^2}\right) \quad \text{Equation 2-19}$$

In Equation 2-19, τ_x and τ_y are the correlation lengths in the x and y directions, respectively. The assumption that the surface is isotropic effectively means that τ_x and τ_y are equivalent or close to equivalent.

The slope distribution function (SDF),$p_s(\zeta)$, is derived from the HDF and ACF and is thus also a Gaussian function.

$$SDF = p_s(\zeta_x, \zeta_y) = \frac{1}{2\pi w_x w_y} \exp(-\frac{\zeta_x^2}{2w_x^2} - \frac{\zeta_y^2}{2w_y^2}) \quad \text{Equation 2-20}$$

In the SDF, ζ_x and ζ_y are the surface slopes in the x and y directions, respectively. The rms slopes are given by w_x and w_y.

Once the above functions are defined for a proposed surface, the 2-D generation occurs using the method given by Garcia and Stoll[13]. A discrete and uncorrelated mesh of points located in the x-y plane, $\zeta_u(x,y)$, is generated using a Gaussian random number generator, and then correlation is achieved by applying a Gaussian filter to the resultant height distribution, as demonstrated in Equation 2-21.

$$F(x,y) = \frac{2}{\tau\sqrt{\pi}}\exp\left(-\frac{2(x^2+y^2)}{\tau^2}\right)$$ Equation 2-21

The final 2D surface $z = \zeta(x,y)$ is then defined as Equation 2-22, and is generated using a Fast Fourier Transform (FFT) algorithm written in MATLAB[14].

$$z = \zeta(x,y) = \iint_{-\infty}^{\infty} F(x-x', y-y') \times \zeta_u(x',y')dx'dy'$$ Equation 2-22

Figure 2-10 shows the 2D Gaussian surface generated with 500 surface points in a 20 x 20 micron space, with rms roughness of 10 nanometers and autocorrelation length of 1 micron. As seen in the 1-D case, the generated rms height and correlation length are close to the values entered into the algorithm. Due to the large number of surface points used, skewness is low and kurtosis is high. Correlation lengths in the x and y directions are identical, typical of an anisotropic, random surface.

2.8.6. Features of the surface scattering model

This surface scattering formalism makes use of and improves through parameterization and enhanced variables a set of scattering codes originally written by David Bergström for his doctoral dissertation[14-16]. Bergström's work involved laser absorption by metal surfaces, and made no attempt to exercise his models against adjustable indices of refraction or spectral wavelength effects; his study focused primarily on the relationships between absorbance and surface slope for metal processing applications.

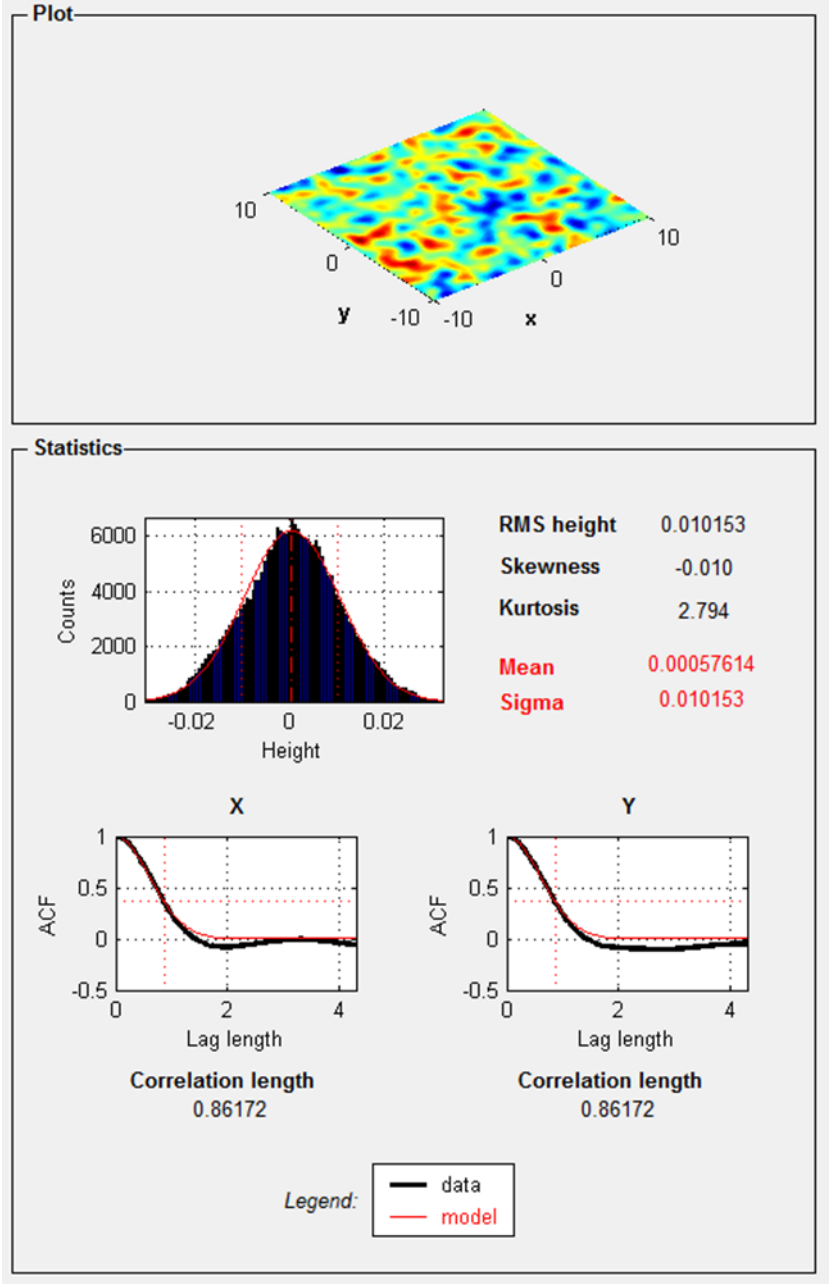

Figure 2-10. Representative output and surface statistics in a 2-D Gaussian rough surface generation. The autocorrelation lengths were both entered as 1 micron, and the rms roughness was entered as 10 nanometers.

The primary feature of this surface scattering model is the high generality of the code. The surface of interest can be defined, materialistically, by a complex refractive index only, requiring only two known values or characteristics of the surface for roughness inputs, the refractive index η and

the coefficient of extinction k, and all of these values are known for regular polymers or can be predicted for novel or poorly characterized polymers[17]. These material properties, defined with the surface roughness statistics, inform the entire model, and so many unique or regular materials may be investigated here; metals, ceramic, dielectrics, and heterogeneous blends to name a few.

A question that must be addressed when defining rough surfaces discretely from global statistics is whether the surface is built along a Gaussian distribution of peaks and valleys, or whether a fractal dimension is used to describe the statistical spread of surface features. While, historically, Gaussian distributions have been used, as they describe well surface formed by a large number of random and repeated events (sand-blasting, orbital polishing, ocean waves, photodegradation), it has recently become *de rigueur* to model surfaces using fractal dimensions. As such, there is a lively debate in the literature as to which surface is most representative for a rough random surface. Luckily, this modification can be rewritten into code fairly simply, and, for the majority of surface peaks, there is great overlap in Gaussian and fractal distributions of surface peaks so that the distinction is effectively not as important as it may initially seem. For the following studies a Gaussian distribution is used. Given a set of surface statistics, the discrete points on the surface are generated using the Spectrum method presented in the literature[12].

Another feature of the model presented here is the incorporation of spectral dispersion of the material index of refraction into the model, which accounts for the small yet real and measurable change in refractive index of dielectric materials across a range of incident radiation wavelengths. This is due to the difference in incident wavelength and resonant frequencies of the bound oscillating charges in the materials. The magnitude of dispersion is small, but not negligible, for common polymers. In the model the incoming photon wavelength is entered into a mathematical model for refractive index dispersion specific to the material of interest. The dispersion-corrected index is then used for that material in the remainder of the simulation.

2.9. Random rough surfaces and surface statistics

The graph in Figure 2-11 shows the surface profile at discrete points along one dimension of a three-dimensional surface having correlation length of 1 micron and rms roughness values of 10 nm and 100 nm. Note that the jagged peaks in the spectrum arise from sampling. Indeed, the straight lines between peaks only serve to visualize the connection between points in this graph.

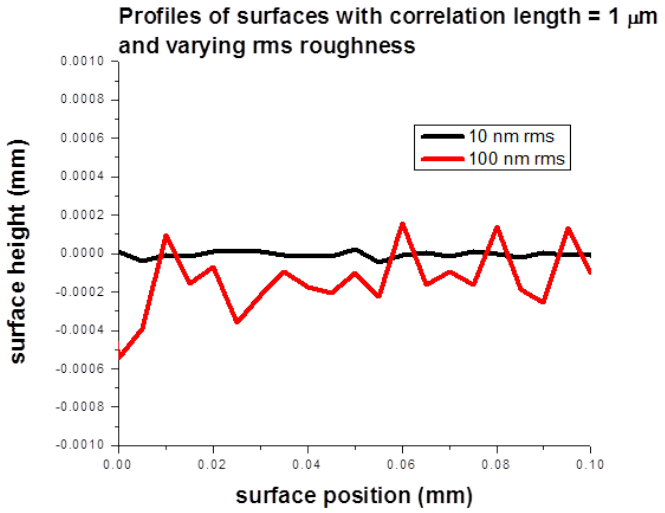

Figure 2-11. Profiles of generated surfaces with rms roughness of 10 and 100 nanometers. Each profile has the same autocorrelation length of 1 micron.

In reality, the facets (or regions between two points on the surface) are not expected to be straight lines. The relationship between rms roughness and correlation length is clearly seen in this graph. While the magnitude of the peaks and valleys is greater for the 100 nm rms sample, the distance between peaks and valleys, indicated by points on the surface, is equal in both cases, representative of surface having equal correlation length, related to the spatial spacing of the peaks and valleys.

2.10. Spectral dispersion of refractive index

Dispersion of a material's index of refraction is a result of differences between incident radiation wavelength and resonant frequencies of the bound charges in the material. The magnitude of dispersion for polymers and glassy materials is much lower than the observed dispersion in metals, but isn't negligible, and should be accounted for simulations of color and appearance. The model used here defines the energy and thus the wavelength of incident radiation by the values of index of refraction and the extinction coefficient for the surface being bombarded by that specific energy, thus, spectral dispersion of polymer index of refraction is accounted for, and, indeed, defines the incident wavelength. This allows for a more general overall model, in that fewer variables are used as inputs. When the index of refraction of a polymer surface is measured at different wavelengths, a set of dispersion coefficients may be obtained and used in a modified Cauchy's equation to generate values of refractive index across a spectral range.

The graph in Figure 2-12 shows the typical index of refraction dispersion curve for the dielectric material PMMA from wavelengths 380 to 780 nanometers.

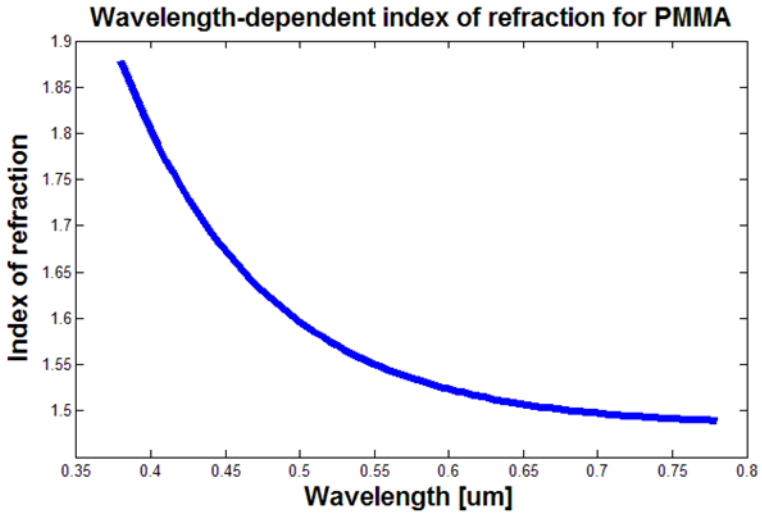

Figure 2-12. Wavelength-dependent dispersion of PMMA refractive index generated using a modified Cauchy expression. Wavelength scale along the x-axis is presented in microns (μm).

This spectral dispersion is determined from a modified Cauchy expression for predicting the spectral dispersion of refractive index in plastic materials[18]. The modified Cauchy expression, Equation 2-23, is incorporated in the geometric ray tracing code so that the index of refraction called by the program for a material at any scattering event location is informed by the incident radiation wavelength at that local point.

$$n_\lambda^2 = A_1 + A_2\lambda^2 + \frac{A_3}{\lambda^2} + \frac{A_4}{\lambda^4} + \cdots \qquad \text{Equation 2-23}$$

In the modified Cauchy expression, A_i are calculated dispersion coefficients at various wavelengths, and these can be found in open literature for many different materials of interest[18].

2.11. Generating surfaces and input parameters for use in geometric optics ray tracing simulations

The surface plots in Figures 2-13 and 2-14 show the 3D representations of two renderings of the same surfaces presented in the above Figure 2-11, where correlation length is 1 micron and rms is either 10 nanometers or 100 nanometers. The area shown is 1 mm^2, and the vertical scales have been adjusted for each figure to enhance comprehension. Note the same visual relationships as in the Figure 2-11 where the peaks and valleys are equally spaced on both surfaces, and the only difference in their construction is the height of peaks and valleys.

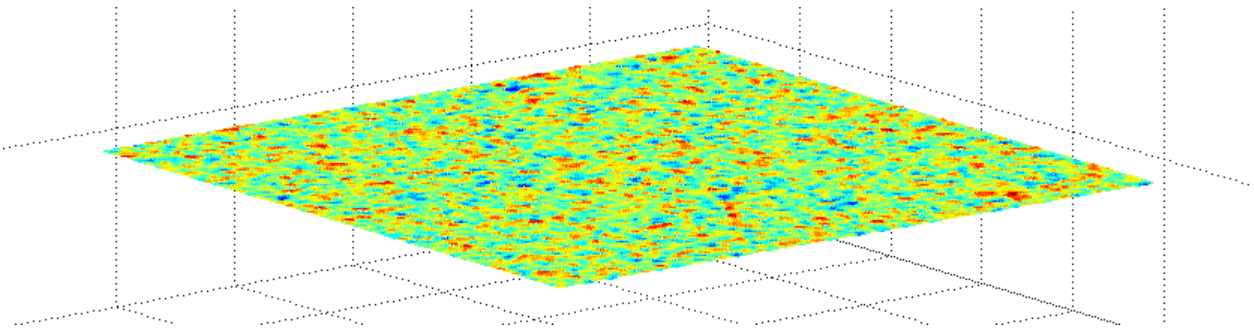

Figure 2-13. A Gaussian surface having autocorrelation length of 1 micron and rms roughness of 10 nanometers. Dimensions of the surface are 0.1 mm x 0.1 mm.

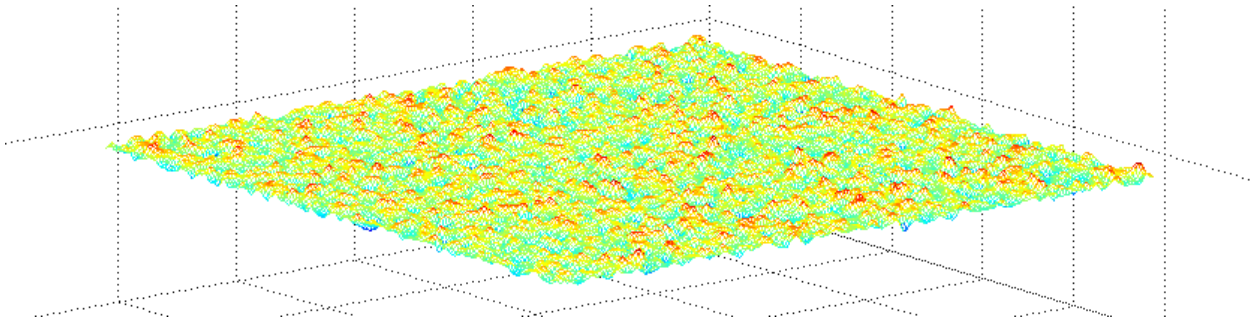

Figure 2-14. A Gaussian surface having autocorrelation length of 1 micron and rms roughness of 100 nanometers. Dimensions of the surface are 0.1 mm x 0.1 mm. Note the same spacing of peaks and valleys as in the smoother surface in Figure 2-13; both surfaces have equivalent autocorrelation length.

To demonstrate the 3D surface scattering model inputs and representative outputs, a case study for a rough PMMA surface is provided here. The material of the surface being impinged on is a dielectric polymer of methyl methacrylate, PMMA, and the dispersion-altered index of refraction equation is given by Equation 2-23 and Figure 2-12. The surface roughness range is user-defined as ranging from 0 to 2 microns, while the correlation length is kept constant in this example as tau = 1 micron, and trends may be elucidated by keeping the correlation length constant and adjusting the rms, or vice versa. The simulation area is user-defined as 1 mm^2.

The wavelength of incident radiation may be chosen by the user and, indeed, may be any value that correlates to a real wavelength, from x-rays to radio waves. Here, a set of five wavelengths is chosen, representative of the visible spectrum of EM radiation; 380, 480, 590, 680, 780. The 590 nm value is chosen to closely emulate the sodium d-line, which is 589.29 nm, and is the green laser commonly incorporated into hand-held gloss measurement devices, such as an over-the-counter Byk-Gardner color measurment device. The other values are chosen to correlate with the range

commonly used in visible absorbance measurements, 380-780 nanometers. A range of common incident angles is chosen, 0 (head-on), 20, 45, 60, and 85 (grazing) degrees. All these incident angles are commonly used in coatings and materials appearance measurements. The 0 degree angle is an especially interesting case, because at an incident angle of 0 degrees, no matter how rough the surface is, no part of the surface is invisible (or hidden in shadow) to the incoming photons.

The total number of surface points is arbitrary and is chosen by the user, in this case 40,000 points distributed equally across the surface of the material. The number of first strike points is equal to the number of photons fired at each surface. Here, the number of first strike points is 1600. To obtain statistically meaningful results for the surfaces described by the parameters rms and correlation length, five separate surface realizations will be performed for each combination of rms and correlation length; the results from the five surfaces will be averaged to yield a Monte Carlo value of average scattering properties for each surface type.

2.12. Geometric optics ray tracing simulations: steps and results

The geometric optics approximation is a ray tracing method of scatter prediction and is arguably the most common approximation approach used to approach radiative transfer calculations. The geometric optics approximation of ray tracing is commonly used in rough scattering simulations[19-23], primarily due to its simple theory and relatively light computational expense, as compared to the more analytical numerical integration techniques that are required for more rigorous treatments[24-28].

Generally, the geometric optics approximation is regarded as valid when the incident wavelength-normalized correlation length, τ/λ, and also the incident wavelength-normalized surface roughness, rms/λ, are both larger than unity, representing surfaces safely above the geometric limit.

The geometric optics approximation incorporates multiple scattering events into its solutions, and can therefore predict diffuse scattering behavior when a surface becomes very rough and multiple scattering begins to occur. The geometric optics approximation is thus able to predict forward, diffuse, and retro-reflectance.

The geometric optics approximation is computationally less expensive than other exact solutions of electromagnetic scattering theory, since the matrices in electromagnetic scattering integrals are not needed to be solved. The geometric optics approximation requires about one hundredth the CPU memory and one fifth the time to solve, as compared to the exact solution and is a suitable approximation for many rough surfaces having varying surface feature parameters[19].

In the limit of a perfectly smooth surface, only one scattering event takes place, and the geometric optics approximation reduces to the Fresnel approximation solution of specular scattering.

The geometric optics approximation model employed in this work is an extension of two- and three-dimensional codes first reported by Bergström, which are available online[14-16]. Bergström[15] investigated the fundamental light absorption mechanisms of laser-machined metals in order to determine the optimum processing conditions and parameters for laser processing of metals. To do so, he used ray-tracing methods to analyze the influence of surface topography on light absorption. Bergström found that at normal incidence, surface absorbance has a threshold at an rms/τ surface slope value, after which it increases sharply due to the onset of multiple surface scattering[15]. Therefore, the codes by Bergström do not include any angular range, nor do they allow for spectral scattering (by an incident wavelength range) to be considered. Because the color and appearance (and, indeed, the entire electromagnetic signature) of an object is so wavelength- and angle-dependent, the model developed in this thesis incorporates these variables will be superior to

previously reported work in the literature, and will provide a new approach to the existing models that are currently available.

The geometric optics approximation model used here predicts the bidirectional reflectance distribution function (BRDF) for the scattering of a two- or three-dimensional rough surface of a well-defined rms and correlation length with an arbitrary surface index of refraction and extinction coefficient. Figure 2-15 shows a schematic of a typical scattering geometry. The steps used in the geometric optics approximation simulation are as follows, and are similar ray-tracing models presented elsewhere in the literature [14-16, 20, 29, 30].

First, random rough surface profiles with Gaussian peak and valley distributions are generated by using the Spectrum method outlined by Thorsos[12] and surface derivatives, tangents, and slope values are calculated for each node or point on the surface.

The angle of incident radiation is specified, and a number of first reflection points are chosen. The number of first reflection points may be less than, equal to, or greater than the number of surface points, and can be randomly or equidistantly distributed along the surface or surface profile.

After first reflection points are chosen, local strikeability tests are performed to ensure the surface area chosen by the computer code is not masked in shadow and therefore unreachable by the incident photon. To do this, the angle of the tangent plane to the surface point is compared to the angle of the incident photon; if the photon is incident at an angle larger than the tangent plane angle, the surface area is not accessible by the photon and a new first strike point is chosen.

A shadowing test is then performed to determine whether irregularities or large surface features will cause areas of the surface to be "unseen" by the incident photon. This test becomes more important as more oblique angles of incidence are used.

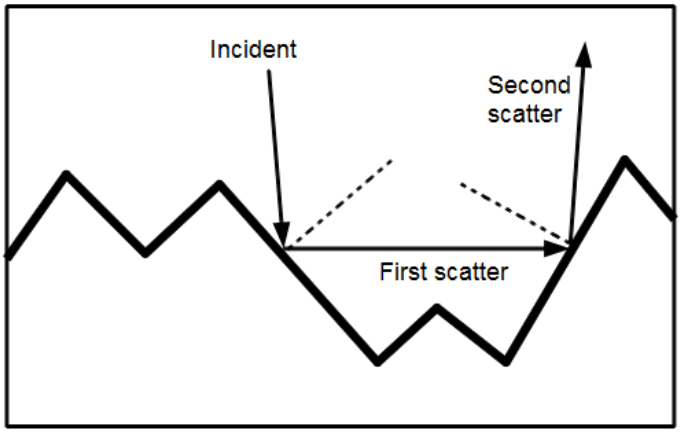

Figure 2-15. Rough surface scattering geometry where multiple scattering occurs on a microfaceted surface.

The incident angle is compared to the angles of the ratio of differential changes between the first reflection point and any other point on the surface (all points to the left if the ray is incident from the left and vice versa). If the ray is incident at an angle larger than any ratio of differential changes then the reflection point is shadowed and another first reflection point is chosen.

Next, strikeability and shadowing tests are performed at each chosen first reflection point until a point satisfies both tests, meaning it is not shadowed and is strikeable by the incident photon. Employing the Fresnel approximation that all local scattering events occur on a locally perfectly flat plane, the angle of the scattered ray is calculated using Snell's Law. To account for absorption or extinction, the energy of the scattered photon is calculated as the energy of the incident photon multiplied by the Fresnel coefficient for a surface material with a given index of refraction, extinction coefficient, and local angle of incidence.

The presence or absence of a second reflection point is determined by comparing the local topology around the first reflection point to the outgoing photon scattering angle, similar to the shadowing test performed earlier.

If a new reflection point is located for the scattered photon, that photon becomes an incident ray and the scattering process (including any possible successive reflections) is continued until the photon leaves the surface. A new first reflection point is then selected and the ray-tracing process continues until all first reflection points and number of incident photons has been accounted for.

After all first reflection points have been addressed, the scattering energy at each scattering angle is divided by the total amount of energy incident on the surface, which is the defined as the differential reflection coefficient. The BRDF is then calculated by dividing the differential reflection coefficient by the cosine of the outgoing scattering angle and the size of the scattering region $d\Omega_s$, in radians, and multiplying by π.

If more statistically accurate results are desired, the above steps are repeated for a set of different randomly generated rough surfaces having the same surface roughness parameters (rms roughness and correlation length), and results from each simulation are averaged into the final result.

To obtain results that can predict color and appearance, the geometric optics approximation ray tracing procedure may be performed on a range of incoming photon energies (i.e. wavelengths) and across a range of incident angles. Furthermore, a variety of combinations of surface roughness and correlation length may be used, in order to obtain relationships between roughness and appearance.

2.13. Regions of geometric optics validity for rough surface scattering simulation

Tang et al.[19] studied geometric optics approximation results and compared their validity to the exact electromagnetic theory solutions of electromagnetic radiation scattering and provided regions of roughness/correlation length where the geometric optics approximation is valid. In general, and in previous literature, it's believed that the geometric optics approximation should only

be applied when τ/λ and σ/λ are both >>1. This is said to be the geometric limit of surface scattering modeling. However, Tang et al. demonstrated (Figure 2-16, below) that the approximation is valid in some cases even when τ/λ and σ/λ are less than unity. Surfaces having values of $\sigma/\tau > 4.0$ are not valid for use with geometric optics approximation, and in these cases, more rigorous electromagnetic theory solutions should be used. In any case, the incident angle, the ratio of roughness to correlation length, and the ratio of roughness to wavelength all have a strong influence on the validity of the model being applied. Figure 2-16 was drawn by tracing curves of acceptance criteria E_{SR} and E_d for different values of σ, τ, and incident angle. The directional energy criterion, E_d, is defined as the ratio of the difference in directional reflected energy predicted by the exact solution and by the geometric optics approximation within a specific angular region. Comparison of different models led to an accepted validity cut-off value of $E_d = 0.2$, so the approximation may be used when $E_d < 0.2$. Similarly, E_{SR} is the ratio of the difference in energy predicted by the approximate solution relative to the energy predicted by the exact solution, and when $E_{SR} < 0.2$, it can be said that the results from the approximation and from the exact solution are in agreement, and the geometric optics approximation is valid.

In general, Tang et al.[19] have shown the ray tracing approximation using geometric optics is valid and thus corresponds well to the exact analytical solution for situations where $\text{rms}(\cos(\theta_0)/\lambda > 0.17$, where θ_0 is the angle of incidence relative to the global surface normal, and for surfaces with rms/τ less than 2.0.

2.14. Results from geometric optics ray tracing simulations of surface scattering

Some of the representative outputs of the simulation performed with the above input parameters are provided below.

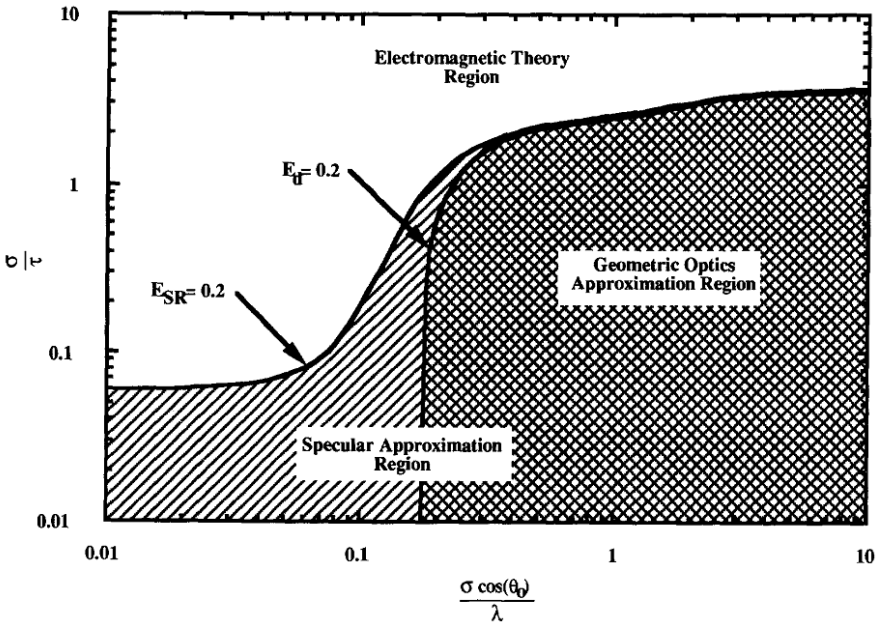

Figure 2-16. Regions of validity when using the geometric optics approximation. Reproduced from [19].

2.14.1. Mean hemispherical reflectance as a function of roughness and incident angle

The first plot shown in Figure 2-17 presents trends in mean hemispherical reflectance as a function of roughness and angle if incidence, as rms increases and correlation length is held constant at 1 micron. The wavelength of incident radiation in Figure 2-17 is 590 nanometers, corresponding to green light, sodium d-line. In Figure 2-17, the mean hemispherical reflectance is plotted as a function of varying rms roughness and angle of incidence. The mean hemispherical reflectance is diffuse and therefore non-directional, that is, it is a measure of all the radiation that leaves the surface as opposed to being transmitted into it. The mean hemispherical reflectance, at every value of rms roughness, increases with increasing angle of incidence, as expected from a simple extrapolation of Fresnel reflectance plots. The mean hemispherical reflectance also decreases with increasing roughness due to a greater amount of shadowing on the surface that effectively serves to trap photons and force them to transmit into the surface after repeated surface scattering or

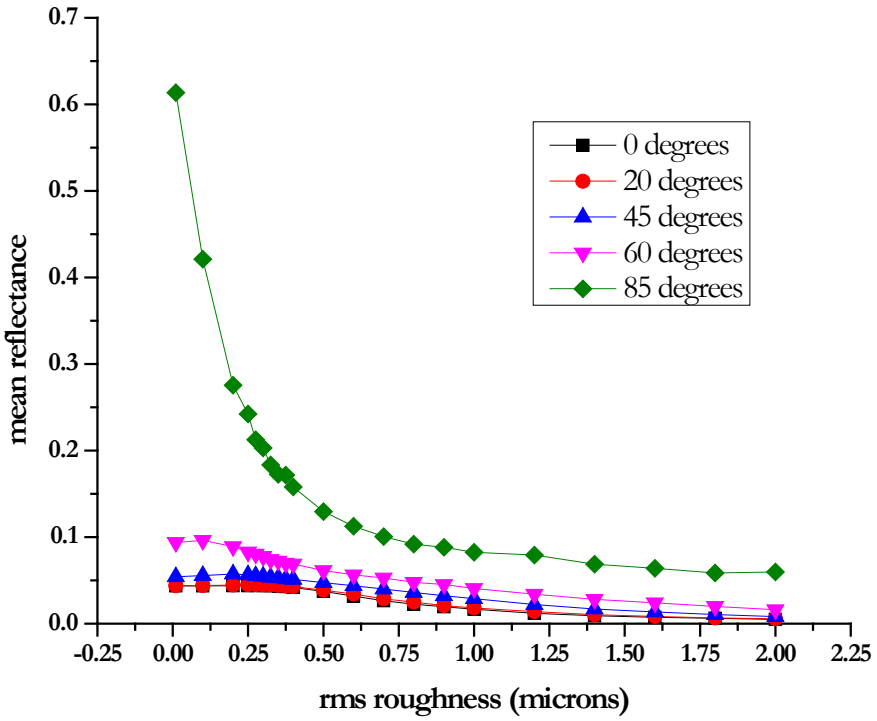

Figure 2-17. Mean hemispherical reflectance as a function of roughness and angle of incident radiation. Surface is PMMA. Incident wavelength is 590 nanometers. Autocorrelation length is fixed at 1 micron.

"bouncing" interactions. It's important to note that the decrease in mean hemispherical reflectance is not linear across rms or surface slope, or changing angle of incidence. That is to say, the decrease in reflectance with increasing roughness cannot be predicted using a simple linear relationship, nor can the decrease in reflectance as angle of incidence decreases and approaches the surface normal.

2.14.2. Proportion of surface caught in shadow

One can use the results from a geometric optics simulation to assess not only scattering properties, but also characteristics of the surface, such as the amount or proportion of the surface effectively caught in shadow due to surface roughness. Figure 2-18 displays the amount of

shadowing or proportion of the surface caught in shadow for PMMA with varying rms roughness and a fixed correlation length with incident radiation of 590 nanometers at various incident angles.

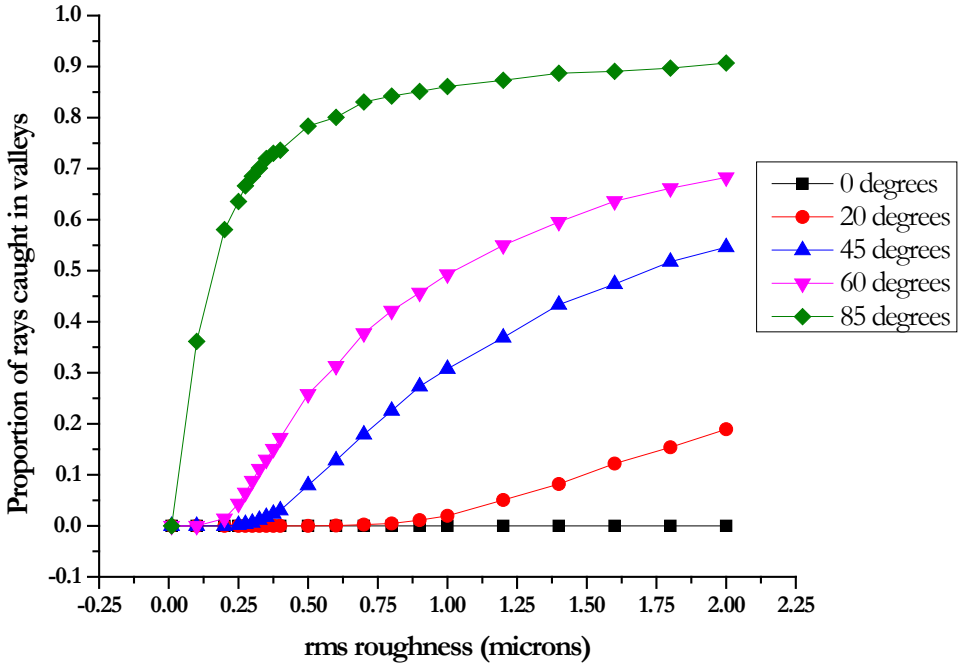

Figure 2-18. Proportion of surface caught in shadow as a function of surface roughness and increasing incident angle. Surface is PMMA. Incident wavelength is 590 nanometers. Autocorrelation length is fixed at 1 micron.

Here, "caught in shadow" means not strikeable by, or masked to, an incoming photon. The rays caught in shadow will increase both as rms increases and as incident angle increases. At high angles of incidence there is greater chance that an incoming photon will strike a very steep facet on the surface and will scatter out or "fly out" of the simulation space.

Figure 2-18 indicates that as long as the incident radiation is head-on, at 0 degrees, none of the surface is caught in shadow. This is not a surprising result, but serves as a good check on the validity and soundness of the chosen geometric optics code. The relationship between increasing angle of incidence and increasing proportion of surface caught in shadow is interesting in that it is

non-linear, and the onset of quick increases in shadowing proportion occurs at increasingly smooth surface values as angle of incidence increases. That is to say, very little surface roughness is needed to shadow the majority of the surface for an incoming photon with a near-grazing 85 degree angle of attack. This is also an intuitive result, but one that is difficult to quantify without using geometric optics simulation.

The shadowing results in Figure 2-18 have been compared to the shadowing function derived by Brockelman and Hagfors [21], as well as to the shadowing function corresponding to Beckmann scattering theory [8]. Brockelman and Hagfors derive a shadowing function, R(θ), which accounts for facets of the surface that are tilted but are not in fact in shadow due to the parallel alignment of the incident radiation. These favorably oriented surface features will serve to reduce the amount of surface effectively in caught in shadow. This is in contrast to the Beckmann shadowing function, S(θ), which is independent of the tilt of any particular surface features, and which may overestimate the effect of shadowing by rough surface features.

Figure 2-19 shows the comparison between the shadowing results presented here and the shadowing functions developed by Brockelman and Hagfors (S(θ)) and Beckmann (R(θ)). The results are plotted as the proportion of the surface caught in shadow, corresponding to 1-S(θ) and 1-R(θ) in the historical models, as a function of the unitless value L/h_{rms}, the ratio of autocorrelation length to rms surface roughness. Results from the same model are presented using the same color, and results from the same incident angle of radiation are indicated by identical marker geometries. No data for 85° incident angle was available for the Brockelman and Hagfors simulation.

Figure 2-19 indicates that the shadowing results presented here fall between the shadowing functions put forth by Brockelman and Hagfors and by Beckmann. At each value of incident angle, the Beckmann shadowing function overestimates shadowing and the Brockelman and Hagfors shadowing function underestimates shadowing, as compared to the new results from the current

model. It is believed that the individual treatment of individual local microfacet geometry and tilt during the ray tracing algorithm here leads to a more robust method for shadowing prediction and quantification. The concept is the same as that provided by Brockelman and Hagfors, though increased computing power has improved the accuracy of the results.

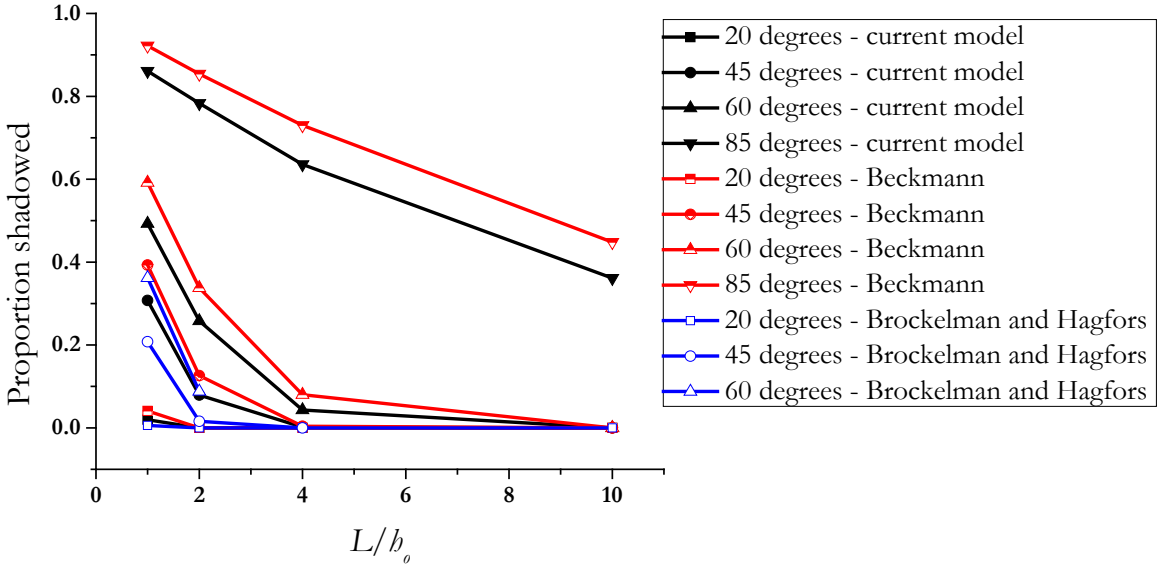

Figure 2-19. Comparison of the surface shadowing results in Figure 3 to those produced by the shadowing functions derived by Brockelman and Hagfors and by Beckmann. Data from both historical models is taken from reference [21].

These results barely represent a tiny fraction of the output possible with a fully-realized surface scattering modeling approach. A forthcoming paper by the authors will investigate further results in more depth [22].

2.14.3. Spectral mean hemispherical reflectance

Figure 2-20 displays the mean hemispherical reflectance of a rough PMMA surface with varying rms roughness, a constant correlation length of 1 micron, an angle of incidence of 45 degrees, and varying incident wavelength across the visible spectral range.

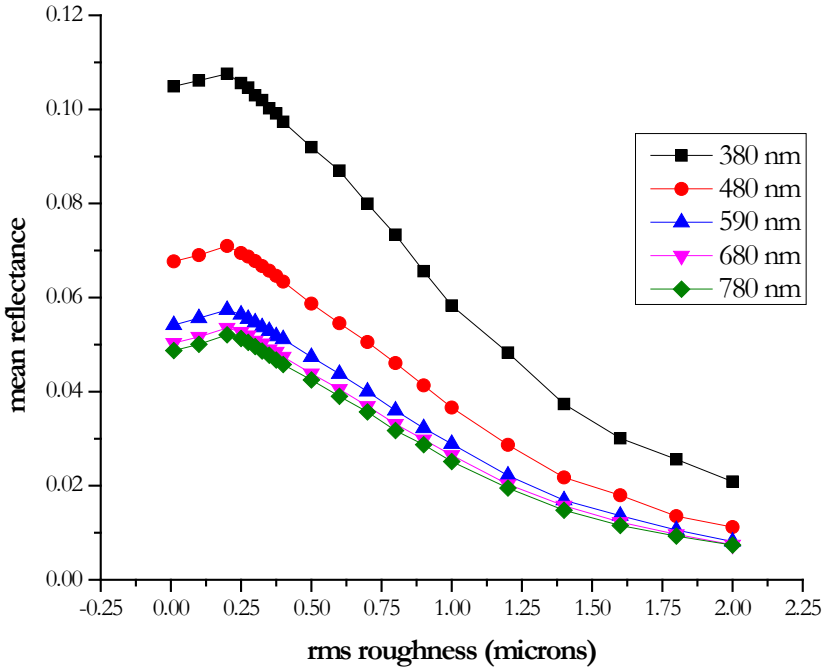

Figure 2-20. Mean hemispherical reflectance as function of surface roughness and incident radiation wavelength. Surface is PMMA. Global angle of incidence is 45 degrees. Autocorrelation length is fixed at 1 micron.

Figure 2-20 indicates that hemispherical reflectance increases initially with roughness as rms increases from 0 to 250 nm, which is the region in which the geometric optics approach used here is not valid, and another method for rough surface scattering must be employed. The hemispherical reflectance decreases steadily from roughness values of 250 nm onwards as the rough surface features move further beyond the geometric limit which is determined by the incident radiation

wavelength. It is important to note that the decreasing reflectance decreases not linearly with wavelength, but instead decreases at different rates for different wavelengths of incident radiation. Interestingly, though, the percent of spectral reflectance decrease is wavelength independent, which will be shown shortly. This is perceived to a viewer as a color change or shift with roughness. This is an actual color change, not simply a lightening or darkening of a surface with increasing or decreasing roughness.

Figure 2-21 displays the mean hemispherical reflectance of a rough PMMA surface with varying rms roughness, a constant correlation length of 1 micron, but with an angle of incidence of 0 degrees, normal to the surface, and with varying incident wavelength across the visible spectral range.

Figure 2-21 shows trends similar to those in the 45 degree incident angle case, shown in Figure 2-20. Interestingly, when the decrease in spectral reflectance is normalized by the smooth surface reflectance value, the plots of reflectance decrease versus surface roughness are identical, regardless of the wavelength of incident radiation involved. As seen in Figure 2-22, it appears that only surface roughness and angle of incidence affect the amount of reflectance shift.

The overlaid plots in Figure 2-22 may be averaged for each incident angle of interest, and polynomial fits may be applied to construct equations that predict the percent decrease in reflectance as a function of surface roughness and incident angle. Figure 2-23 shows the plots for materials being impinged on by 0 degrees (normal) and 45 degrees incident angle radiation. It is important to note that the effects of incident radiation wavelength have dropped out of the equations. The spectral reflectance shift is only dependent on roughness and incident angle.

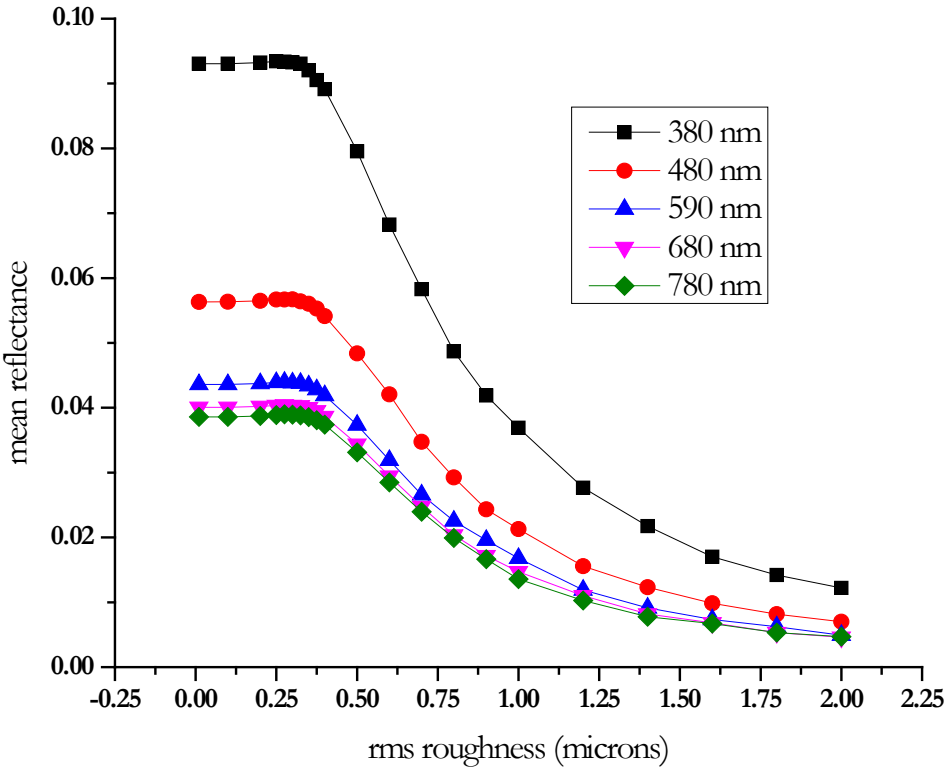

Figure 2-21. Mean hemispherical reflectance as function of surface roughness and incident radiation wavelength. Surface is PMMA. Global angle of incidence is 0 degrees. Autocorrelation length is fixed at 1 micron.

The equation for normal incidence in Figure 2-23 was applied to the empirical spectral reflectance data of an orange epoxy puck having nominal, diamond polished surface roughness (i.e., the surface is "flat"). A simulated roughness of 500 nanometers was applied to the spectral reflectance data using equations derived from Figure 2-23, and a rough hemispherical reflectance spectrum was generated, shown along with the empirical data in Figure 2-24.

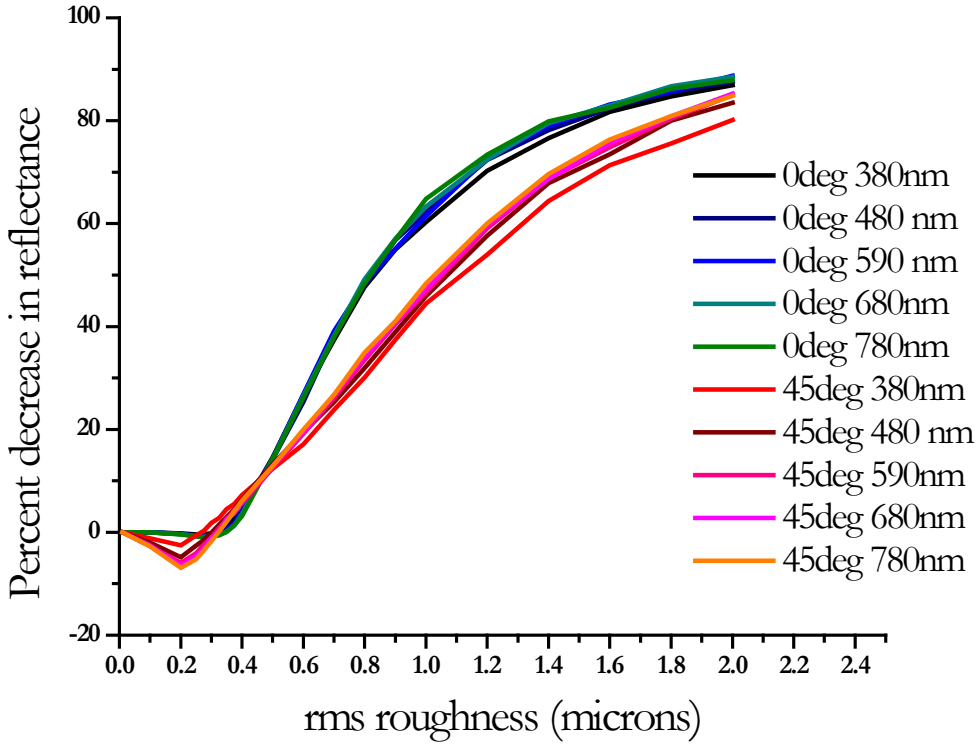

Figure 2-22. Wavelength-independent decrease in reflectance with increasing rms surface roughness. Only surface roughness and angle of incidence affect the amount of reflectance shift.

Color matching and visualization codes presented in Chapter 5 are now ably used to construct color patches that represent the color change with roughening, as the sample is illuminated from the top (0 degrees or normal incident radiation) with a virtual light source C and modeled using the 1964 standard observer functions. The output is shown in Figure 2-25, and the darkening of the material is clearly seen when comparing the real, flat, surface to the simulated, rough surface. Thus, geometric optics simulations can be used to predict the color shift of materials and surfaces as they undergo surface roughening reactions such as photodegradation.

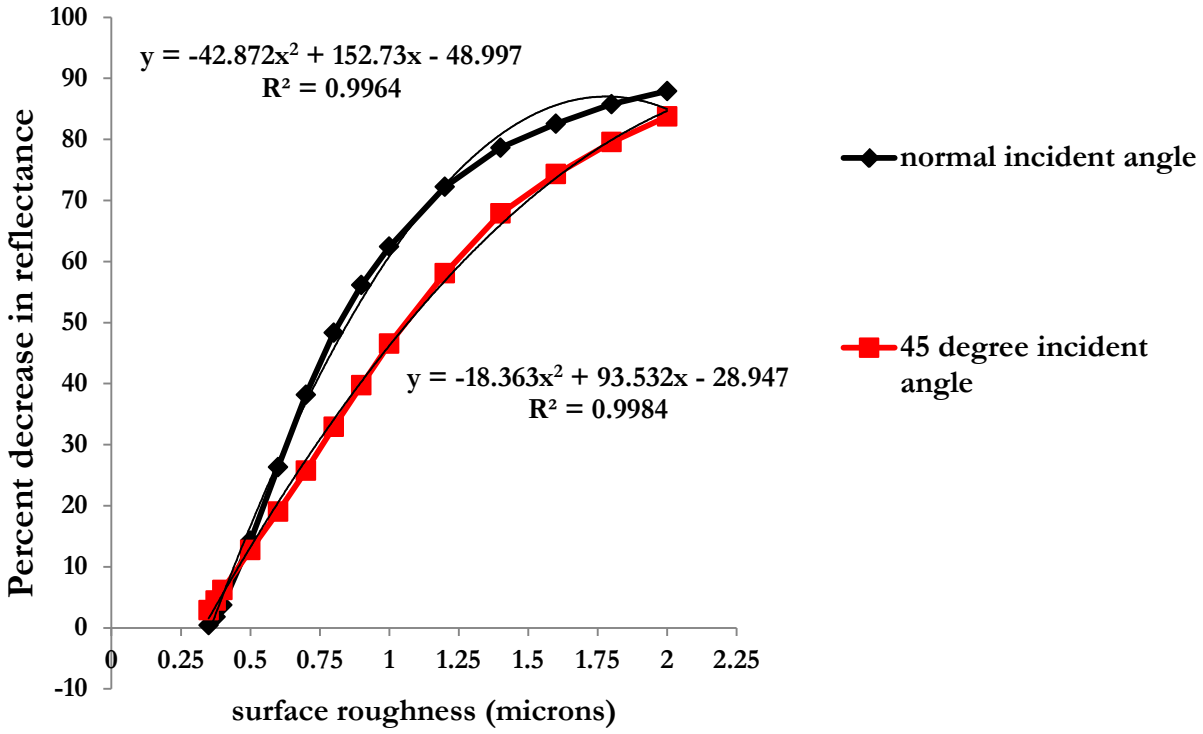

Figure 2-23. Developing equations that predict the percent decrease in reflectance as a function of surface roughness and incident angle. Magnitude of wavelength-independent decrease in reflectance with increasing surface roughness.

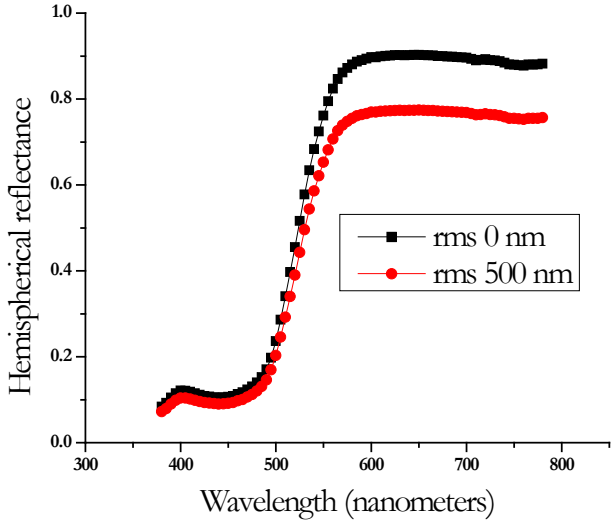

Figure 2-24. Using measured, nominally-rough reflectance data to predict the rough reflectance spectrum. Predicted reflectance change with applied roughness using the geometric optics approximation.

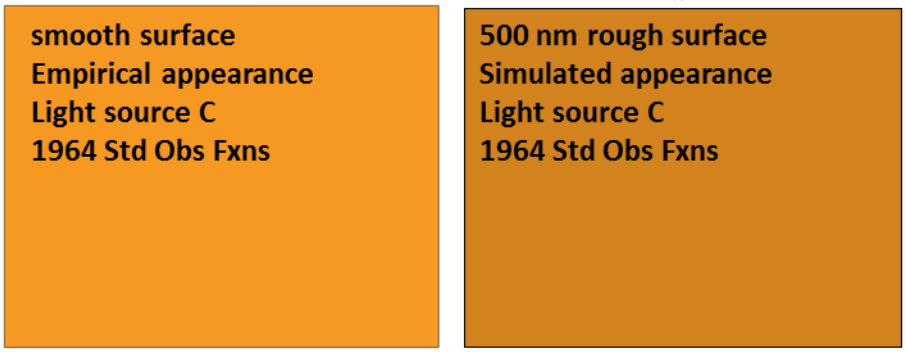

Figure 2-25. Using measured, nominally-rough reflectance data to predict the rough reflectance spectrum and generate color patches of the predicted color response after roughness is applied to the surface.

2.14.4. Number of scattering events per ray

Figure 2-26 displays the average number of scattering events per ray before exiting the simulation space or dying from extinction (low power cutoff) on a rough PMMA surface with a constant correlation length, an incident radiation wavelength of 590 nm and increasing rms roughness and angle of incidence.

In Figure 2-26 the average number of scattering events per ray always increases with increasing roughness (and increasing slope). The number of scattering events per ray is generally lower at increasing angle of incidence, which is caused by the prevalence of photon "fly out" where a near-grazing photon strikes a very steep but slightly tilted surface or facet on the rough surface and back scatters as a fly-out photon. At lower angles of incidence the photons are easier to "trap" in hills and valleys and so the number of scattering events generally is greater.

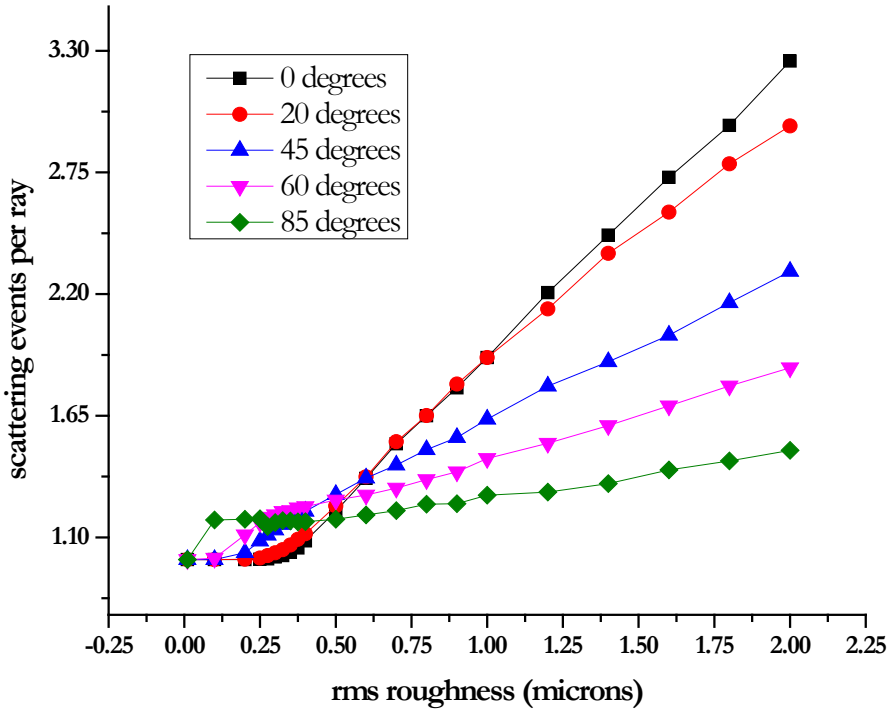

Figure 2-26. Average number of scattering events per incident ray as a function of surface roughness and incident angle. Surface is PMMA. Incident wavelength is 590 nanometers. Autocorrelation length is fixed at 1 micron.

2.15. Comparison of geometric optics surface scattering model to historical models

To assess the general validity of the geometric optics ray tracing codes presented here, comparison has been made for single and multiple surface cases against three codes available in the literature[29, 31]: the Kirchhoff approximation method, the method of moments, and the small perturbation method.

The Kirchhoff scattering solution approximates the surface scattered electromagnetic fields using the tangent plane approximation [31]. When using the tangent plane approximation, the scattered fields at any local surface point are approximated as the fields that would emanate from a

tangent plane existing at that surface point. As it such, it is necessary that the points on the surface have large radii of curvature relative to the wavelength of the incident radiation. Thus, the Kirchhoff approximation is a common approach for modeling the scattering behavior of rough surfaces.

The method of moments is a numerical technique which is commonly used in light scattering simulations. The method of moments applied to scattering mathematics provides a full matrix equation which can be solved numerical by matrix inversion[29]. In the set of method of moments codes available in the literature, Green's function supply the mathematical basis for the derivation of integral equations to be solved[31].

When surface variations are very small compared to the incident wavelength and the rough surface slopes are small in magnitude, the small perturbation method may be used to compute the scattering profile from the surface. The small perturbation method uses the Rayleigh hypothesis to define the reflected and transmitted fields as upward and downward traveling waves, respectively. After applying appropriate boundary conditions, the scattered fields can be calculated from the diffraction integral for the surface of interest[31].

To compare the performance of the current geometric optics model with the three examples listed above, an exemplar two-dimensional rough surface was defined. The exemplar surface was 15.1 microns long and had an rms value of 29.5 nm and an acl value of 206.5 nm. The surface was comprised of 256 surface points and was given properties equivalent to PMMA under air. The incident wavelength was 590 nm. The global angle of incidence in all simulations is 30 degrees. Example codes and numerical output from the codes is provided in Appendix B.

Using the formalism of Tsang et al.[29], the bistatic scattering coefficient $\sigma(\theta_s)$ is defined so that:

$$\frac{P_s}{P_{inc}} = \int_{-\pi/2}^{\pi/2} d\theta_s \sigma(\theta_s) \qquad \text{Equation 2-24}$$

Thus, the bistatic scattering coefficient is the directional or angular component of the portion of incident light that is scattered after interaction with a rough surface.

Figure 2-27 shows the bistatic scattering coefficient plotted against scattering angle for various models. The results in Figure 2-27 are for a single representation of the exemplar surface above. A strong pronounced specular reflectance peak at 30 degrees can be seen in the method of moments (MoM) data set, while the Kirchhoff approximation (KA), small perturbation method (SPM), and the current geometric optics approach (GOA) give no specular reflectance peak when one surface is simulated.

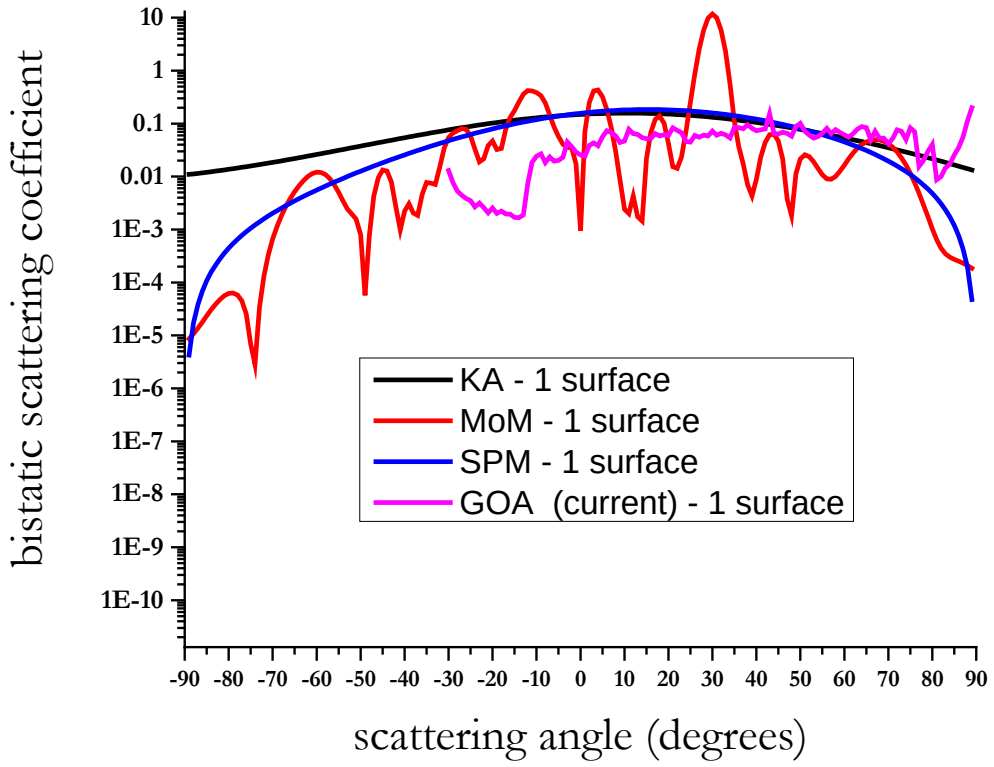

Figure 2-27. Comparison of the angle-dependent bistatic scattering coefficient for the current geometric optics approximation model (GOA) with Kirchhoff approximation (KA), method of moments (MoM), and small perturbation method (SPM) approach. The results in the figure are for a single generated surface.

The current GOA model provides no data in the -90 to -30 degree range, the backscattered domain, because not enough photons are fired to accumulate hits in that vicinity.

Figure 2-28 shows the comparison between the four model types when the bistatic scattering coefficient results are averaged over 100 statistically identical surfaces that are generated and each subjected to light scattering treatment.

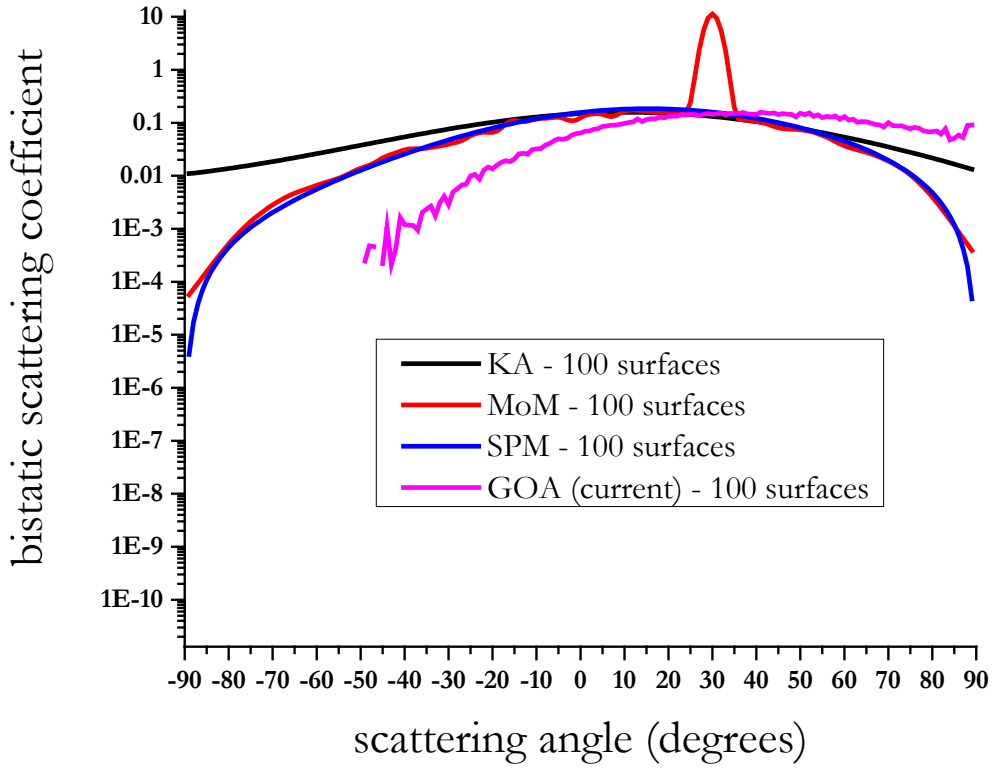

Figure 2-28. Comparison of the angle-dependent bistatic scattering coefficient for the current geometric optics approximation model (GOA) with Kirchhoff approximation (KA), method of moments (MoM), and small perturbation method (SPM) approach. The results in the figure are for 100 generated surfaces all having identical statistical parameters rms and acl.

In Figure 2-28, the general noise level in the MoM and GOA results has been smoothed by the averaging of scattering results over 100 randomly generated surfaces having identical statistical

roughness and autocorrelation length values. Here, the dominant specular reflectance peak from the MoM calculation is the most prominent feature, though the specular reflectance peak can be seen in all four data sets when the data is plotted against a linear scale, as shown in Figure 2-29.

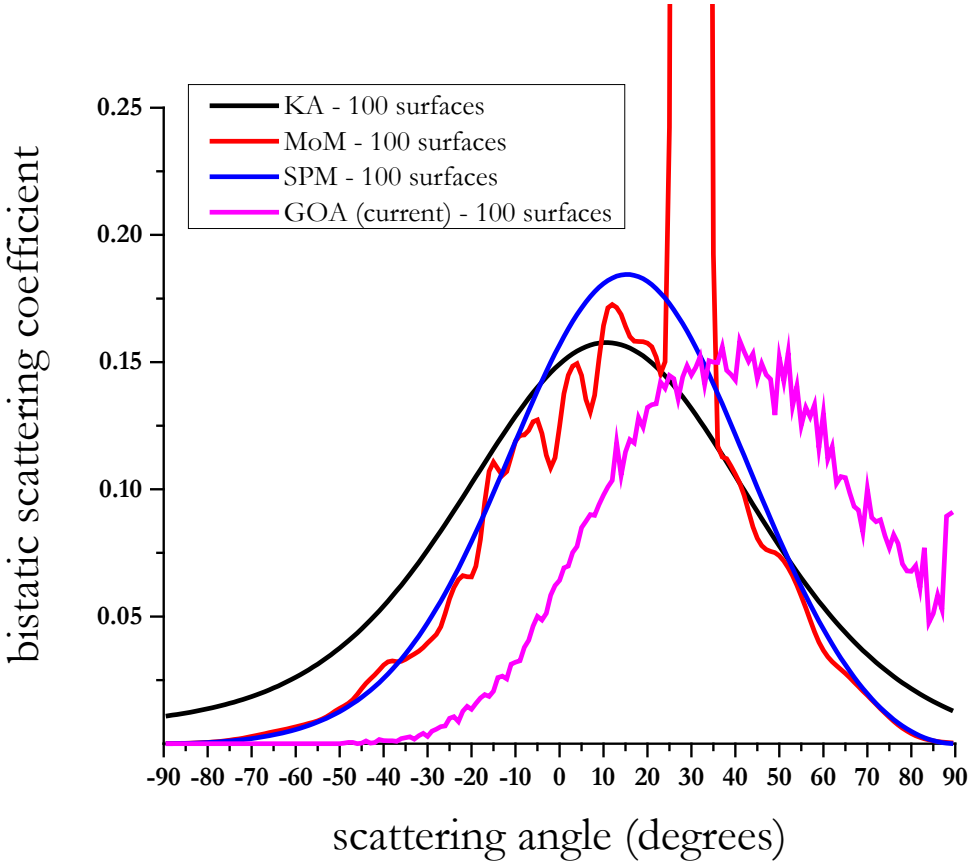

Figure 2-29. Comparison of the angle-dependent bistatic scattering coefficient for the current geometric optics approximation model (GOA) with Kirchhoff approximation (KA), method of moments (MoM), and small perturbation method (SPM) approach. The results in the figure are for 100 generated surfaces all having identical statistical parameters rms and acl. Note the switch to a linear scale on the y-axis.

In Figure 2-29, the similarities between the different scattering approaches are more readily seen. While all methods give scattering profiles of the same general, Gaussian shape, only the MoM and GOA results show a strong presence near the specular reflectance peak, 30 degrees, as would be expected for a surface with only nominal surface roughness such as the one modeled here. In the

MoM case, the specular reflection is observed as a strong peak centered at 30 degrees, while the data from the current GOA model shows a Gaussian scattering profile centered near the specular peak at 30 degrees. From these figures it can be concluded that the present GOA model has some validity with regards to historical models such as Kirchhoff approximation, small perturbation method, and method of moments. The comparison of future versions of the present model against these historical benchmarks will continue to provide insight and guidance towards the general overall improvement of the multiscale code.

2.16. Further reading

The reader interested in learning the basics of surface scattering approaches has much seminal literature to choose from. For starters, one is directed to the classic book by Beckmann and Spizzichino[32], as well as the primer by Bennett and Mattson[4]. Tsang, Kong, and Ding[29] provide excellent examples of numerical approaches to light scattering problems, and Stover[33] presents the science from the perspective of the quality control and inspection of silicon wafer production, where nearly imperceptible surface irregularities may indicate a bad production run. The collection edited by Maradudin[5] is a well-organized overview of the problem and theory of surface scattering, composed with an eye towards surfaces having nanoscale surface roughness. Finally, the doctoral thesis and related papers by Bergström[15] are concise presentations of surface scattering solutions given by geometric optics approaches and bidirectional reflectance distribution function formalism. Bergström's codes are wonderful starting places for those looking to run simulations before writing their own code.

2.17. Summary of surface scatter model

The surface model is capable of simulating the appearance of surfaces provided by diffuse reflection under a variety of different light sources as an example of source metamerism. The model can also successfully predict specular reflectance change with increasing surface roughness. The model also quantifies hemispherical surface reflectance and quantifies its degrees of change spectrally with increasing surface roughness or slope, that is, different incident energies die off at different rates (the reflectance changes are not constant across the wavelength spectrum), the reflectance at 380 nm falls most significantly (this is in the violet range), and this can be related to color change and fading of a surface with exposure, abrasion, or other mechanical or photodegradation means. The surface scattering model is also able to quantify the degree of shadowing with increasing roughness and varying incident angle. The model also tracks the number of average scattering events per photon, which always increases with surface roughness, assuming that the incident photon angle of incidence is greater than non-zero. In general, however, higher angles of incidence cause fewer scattering events due to photon "fly out" after single scattering events at very steep surface facets that are high on the surface in relative altitude.

Obvious extensions of this portion of the multiscale framework would consider non-isotropic surfaces, such as those produced by machining and production processes such as sanding or abrading, surfaces with multiple roughness scales, and surfaces with exponential or fractal surface roughness patterns.

2.18. References

1. Feynman, R.P., *QED: The Strange Theory of Light and Matter*. Princeton Science Library. 1985, Princeton, New Jersey: Princeton University Press.
2. Thomas, T.R., *Rough Surfaces*. 2nd ed. 1999, London: Imperial College Press.
3. Modest, M., *Radiative Heat Transfer*. 2nd ed. 2003, New York, NY: Elsevier Science.

4. Bennett, J.M. and L. Mattsson, *Introduction to Surface Roughness and Scattering*. 1989Washington, D.C.: Optical Society of America. 110.
5. Maradudin, A., ed. *Light Scattering and Nanoscale Surface Roughness*. Nanostructure Science and Technology. 2007, Springer.
6. Bennett, H.E. and J.O. Porteus, *Relation Between Surface Roughness and Specular Reflecance at Normal Incidence*. J. Opt. Soc. Am., 1961. **51**(2): p. 123-129.
7. Croll, S.G. and B.R. Hinderliter, *Statistical approaches for predicting weathering degradation and service life*. Prog. Org. Coat., 2006. **55**: p. 75-87.
8. Hinderliter, B.R. and S.G. Croll. *Predicting Coating Failure using the Central Limit Theorem and Physical Modeling*. in *The Fifth International Conference on Advances in Corrosion Protection by Organic Coatings*. 2009. Christ's College, Cambridge.
9. Croll, S. and B. Hinderliter, *A framework for predicting the service lifetime of composite polymeric coatings*. J. Mater. Sci., 2008. **43**: p. 6630-6641.
10. Hinderliter, B. and S. Croll, *Monte Carlo Approach to Estimating the Pjotodegradation of Polymer Coatings*. JCT Res., 2005. **2**(6): p. 483-491.
11. Dorsey, J., H. Rushmeier, and F. Sillion, *Digital Modeling of Material Appearance*. 2008, New York: NY: Elsevier.
12. Thorsos, E.I., *The validity of the Kirchhoff approximation for rough surface scattering using a Gaussian roughness spectrum*. J. Acoust. Soc. Am., 1988. **83**(1): p. 78-92.
13. Garcia, N. and E. Stoll, *Monte Carlo Calculation for Electromagnetic-Wave Scattering from Random Rough Surfaces*. Phys. Rev. Lett., 1984. **52**(20): p. 1798-1801.
14. Bergstrom, D. *MySimLabs*. 2009 4/16/2009 [cited 2010 May 7th]; Available from: www.mysimlabs.com.
15. Bergstrom, D., *The Absorption of Laser Light by Rough Metal Surfaces*, in *Department of Applied Physics and Mechanical Engineering*2008, Lulea University of Technology: Lulea, Sweden. p. 209
16. Bergstrom, D., D. Powell, and A.F.H. Kaplan, *A ray-tracing analysis of the absorption of light by smooth and rough metal surfaces*. J. Appl. Phys., 2007. **101**: p. 113504.
17. Bicerano, J., *Prediction of Polymer Properties*. Plastics Engineering, ed. D. Hudgin. 2002, New York: NY: Marcel Dekker, Inc.
18. Kasarova, S.N., et al., *Analysis of the dispersion of optical plastic materials*. Opt. Mater., 2007. **29**: p. 1481-1490.
19. Tang, K., R.A. Dimenna, and R.O. Buckius, *Regions of validity of the geometric optics approximation for angular scattering from very rough surfaces*. Int. J. Heat Mass Transfer, 1997. **40**(1): p. 49-59.
20. Tang, K. and R.O. Buckius, *The geometric optics approximation for reflection from two-dimensional random rough surfaces*. Int. J. Heat Mass Transfer, 1998. **41**(13): p. 2037-2047.
21. Tang, K., P. Kawka, and R.O. Buckius, *Geometric optics applied to rough surfaces coated with an absorbing film*. J. Thermophys. Heat Trans., 1999. **13**: p. 169-176.
22. Schott, P., N. de Beauccoudrey, and C. Bourlier, *Reflectivity of one-dimensional rough surfaces using the ray tracing technique with multiple reflections*. Int. Geoscience and Remote Sensing Symp., 2003. **7**: p. 4214-4216.
23. Zhu, Q., *Modeling and measurements of the bidirectional reflectance of microrough silicon surfaces*, 2004, Georgia Institute of Technology.
24. Celli, V., et al., *Some aspects of light scattering from randomly rough metal surfaces*. J. Opt. Soc. Am. A, 1985. **2**: p. 2225-2239.
25. Maradudin, A.A., et al., *Enhanced backscattering of light from a random grating*. Annals of Physics, 1990. **203**: p. 255-307.
26. Gil, J. and M. Vesperinas, *Light scattering from random dielectric surfaces*. J. Opt. Soc. Am. A, 1991. **8**: p. 1270-1286.

27. Tran, P. and A.A. Maradudin, *The scattering of electromagnetic waves from a randomly rough 2D metallic surface.* Opt. Commun., 1994. **110**: p. 269-273.
28. Pak, K., et al., *Backscattering enhancement of electromagnetic waves from two-dimensional perfectly conducting random rough surfaces based on Monte Carlo simulations.* J. Opt. Soc. Am. A, 1995. **12**(11): p. 2491-2499.
29. Tsang, L., et al., *Scattering of Electromagnetic Waves: Numerical Simulations.* 2001, New York, NY: John Wiley & Sons.
30. Brewster, M.Q., *Thermal Radiative Transfer and Properties.* 1992, New York: John Wiley.
31. Tsang, L., J.A. Kong, and K.-H. Ding, *Scattering of Electromagnetic Waves: Theories and Applications.* 2000, New York, NY: John Wiley & Sons.
32. Beckmann, P. and A. Spizzichino, *The Scattering of Electromagnetic Waves from Rough Surfaces.* 1963, Oxford: Pergamon 503.
33. Stover, J.C., *Optical Scattering: Measurement and Analysis.* 1995, Bellingham, WA: SPIE Press.

CHAPTER 3. SIMULATION OF LIGHT SCATTERING BY EMBEDDED OBJECTS OR INCLUSIONS

3.1. Introduction

This portion of the hybrid model for multiscale material scattering simulation considers the various phenomena that a photon experiences after it has been transmitted by a rough or flat surface above an enclosed volume of interest, for example a bulk composite, a bulk polymer matrix, a body of water in the ocean, or a slab of skin that consists of many dermal layers. After a photon incident on the system of interest has a surface interaction or interactions, the refracted or internally-transmitted photon enters the bulk of the object, wherein numerous inclusions boundaries and interphases necessitate the solving or consideration of very many scattering events in order to compute a total or inclusive scattering profile for the material. This is due primarily to the large number of photon / electron interactions that naturally occur at each inclusion or boundary. This is caused by the difference in refractive index between bulk compositions and inclusion composition.

Internal or bulk scattering is a major component of the diffuse contribution to electromagnetic signature, and thus, an improved understanding of the phenomenon and its factors will allow controlled tailoring or fine-tuning of the internal scattering properties. This in turn will lead to improved customization of electromagnetic signatures, as well as improved uses of the inverse formalism, such as enhanced and more informative non-destructive evaluation and remote sensing applications related to electromagnetic radiation scatter.

3.2. Inclusions in real composites, coatings, and other material systems

There are multiple forms of inclusions that must be considered in real composites, nanocomposites, coating systems, biological systems, and even extraterrestrial systems such as asteroid belts and lunar regolith. Inclusions of interest to nanocomposite and coating materials are generally pigments, fibers, nanoparticles or macroscale fillers. These all represent "designed" or "expected" inclusions, while air voids are inclusions that are generally undesirable and are signs of poor formulation or in-service degradation, such as fiber debonding in a composite that results in an air void, or incomplete pigment covering by polymer resin so that a coating is globally or locally above its critical pigment volume concentration, an example of coarseness in pigment distribution. There are also heterogeneities present in these materials. These are likewise either by design, as in the case of certain copolymer materials, such as thermoplastic elastomers like PP/SEBS (polypropylene/styrene–ethylene–butylene–styrene), or are the result of poor compatibilization or incomplete surface stabilization of otherwise stable phases in a formulation.

When taking all electromagnetic signature contributors into account, there are also molecular hindered amine light stabilizers (HALS) and other internal absorbers or chromophores that will interact with incident radiation. Globally within a bulk material Beer's law must be accounted for, where material extinction coefficients tend to cause a propagating radiation beam to attenuate to extinction as it passes through the material.

3.3. Mechanisms of bulk material light scattering

The electric field of an incident or impinging wave exerts various forces on the elementary charges in the matter that comprise the scatterer or inclusion. This force sets the charges into oscillatory motion with the same frequency as that of the incident field that is driving them and they

thus radiate EM radiation of that frequency. Light scattered by molecules or particles is therefore a form of excited electromagnetic radiation. All objects emit radiation whether they are exposed to an external source of radiation or not, so it's sometimes useful to separate the scattered field from the background field in order to deduce patterns or trends in the scattered field. This removes the background emission radiation that is inherent to every real-world scattering problem.

The electric field of a light wave illuminating a single scattering entity excites the elementary charges of which it is composed and the oscillating charges consequently radiate or scatter light, the magnitude of which is not, in general, the same in all directions. The average direction that the scattered radiation travels in is dependent upon, among other things, the size of the scatterer relative to the independent radiation wavelength and refractive index distribution within the material if it possesses heterogeneities or anisotropy, along with the degree of symmetry in the scatterer's topology.

In perhaps the simplest scattering scenario, a dipole is illuminated by a beam of light, so the two charges that make up the dipole are set into oscillatory motion at the same frequency as the incident wave. Charges in oscillatory motion, indeed, in any motion, radiate electromagnetic waves because of the finiteness of the speed of light. Real scattering situations will involve millions upon millions (and more!) of these diploes, but the scattering phenomenon underlying each case or scenario is the same; a charge or set of charges is set into oscillatory motion by a wave passing by or through them, and the oscillatory nature of the "triggered" or "excited" charges will cause them to radiate emission that is of the same frequency as the incident radiation. Thus, light is created and scattered as incident radiation impinges on an object in its path.

3.4. Scattering event frames of reference and the geometric limit

There are three cases or general scenarios to consider when discussing and determining which method of scattering event solution is to be used, either geometric optics or finite element approaches. These cases are the ideal flat surface, the real surface, and the nanoscale region surface.

The ideal flat surface is a surface whose dimensions in the area of scattering interest are much larger than the geometric limit. A flat surface has infinite aspect ratio, locally, compared to the incident wavelength, so these scattering events may be reduced to simple Snell and Fresnel calculations, even in the event of radio waves with wavelengths in the kilometer range. This is a fair assumption to make in the case of x-ray scattering by a liquid mercury surface, or radio wave scattering by the surface of the moon. In the geometric optics approximation approach to rough surface scattering presented in Chapter 2, all surface scattering events are reduced to a frame of reference where a flat surface geometries and the Fresnel approximation may be used to solve for the scattering event solution, represented below in Figure 3-1.

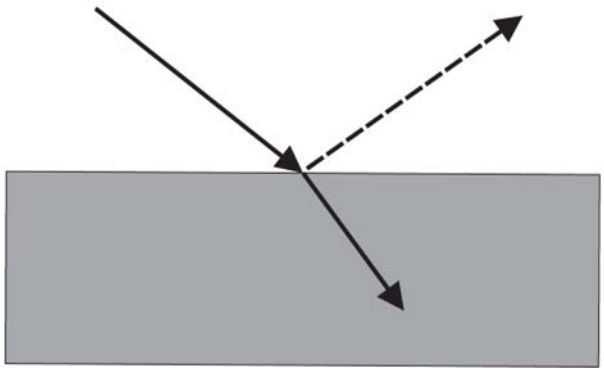

Figure 3-1. A simple scattering frame of reference where the Fresnel approximation holds true and the length scale of interest is much larger than the geometric limit imposed by the incident radiation wavelength.

The second size region of interest concerns what can be termed "real surfaces" and the surface of a large, micron-sized (or many micron-sized) filler particle is representative of this

scenario, shown in Figure 3-2. The dimensions of a surface on a "real surface" approach the geometric limit depending on incident radiation wavelength. Here the Fresnel approximation of an ideal flat surface may still be used in many cases, although accuracy may be hindered by such an approach. In these systems the surface is ideally flat *somewhere* or at every local point of interest, but the surface slopes are different, irregular, or not consistent with a truly or ideally flat surface which would by definition have either one unchanging surface slope value at each and every location on the surface. In general, however, this particle treatment of light may still be used to solve for scattering events on many real surfaces.

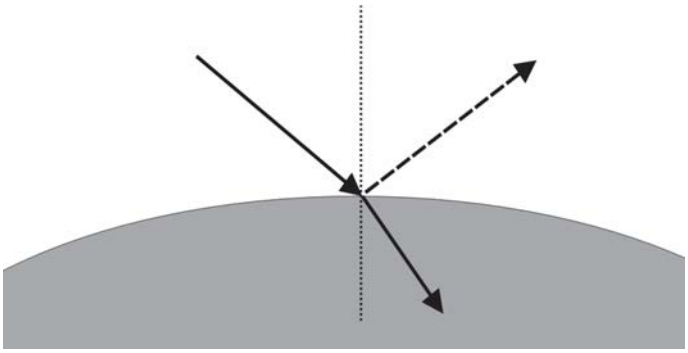

Figure 3-2. Real surfaces have local curvature of varying degrees, but in some cases the Fresnel approximation still holds and calculation is simplified. These surfaces have scattering features that reside in the same order of magnitude as the geometric limit.

Finally, there are the nanoscale regions where geometric approaches are not appropriate, shown in Figure 3-3. Scatterers in the nanoscale region are generally at or near, below, or well-below the geometric limit defined by the incident wavelength of radiation. In this situation ray tracing approaches fail due of their lack of proper treatment and simplifying assumptions, and the most proper or prudent approach is the full treatment of the Maxwell equations. In this size regime, an incoming photon is felt or experienced by the scatterer not as a single photon or point source, but rather as a moving wavefront that impinges on the scatterer.

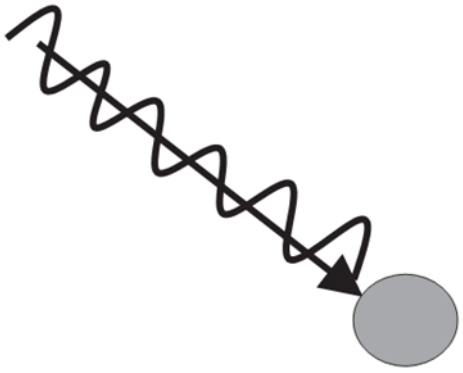

Figure 3-3. A nanoscale scattering frame of reference where the scatterer length scale is near, below, or well below the wavelength of incident radiation. Here, particle approaches to light may not be used, and the best treatment relies on wave solutions using the Maxwell equations.

Scatterers much smaller than the incident wavelength of radiation scatter nearly the same in all directions. The average scattering angle -- the angle between the incident and scattered photons - is 90 degrees: that is, as many photons are scattered into a hemisphere of directions about or centered about the forward direction as are scattered into a hemisphere centered about the backwards direction. This is why Mie calculations give a scattering angle of 90 degrees in many cases, which in a single event describes sideways scattering, when, in actuality, scattering is more or less evenly distributed about the circumference (2D) or surface area (3D) of the scatterer in all directions.

3.5. Scattering events and geometric complexity

Just as the length scale of surface roughness must be considered, the local complexity of the scatterer geometry must be considered, as well, when picking a solution method.

As mentioned previously, the flat surface reflection represents the simplest scattering event geometry, and employs simplifications such as Snell's law and Fresnel reflection equations to solve

the scattering problem. These cases, schematized in Figure 3-4, are easy to solve and relatively straightforward.

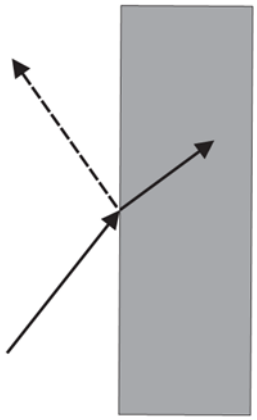

Figure 3-4. A scattering situation with little or no geometric complexity is easy to compute.

Next in scattering topology complexity is the ideal, spherical particle, Figure 3-5, which represents a medium level of complexity and may be solved for using approximate theories such as Mie theory. These approximations may be used when the system of interest represents a very large ensemble of spherical scatterers, or when geometric irregularities serve to cancel each other out, so the net average geometry of an inclusion is statistically represented by a sphere.

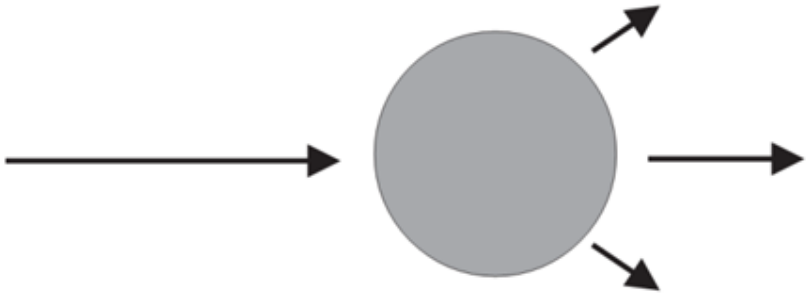

Figure 3-5. A spherical scatterer has medium geometric complexity and simplified expressions are available to solve for certain cases.

Lorenz-Mie scattering theory is the analytical solution of the Maxwell equations for the scattering of electromagnetic radiation by a perfect sphere. Many codes are available in the literature that quickly and efficiently solve for such scattering events.

Given a sphere's size index ($x=2\pi r(n/\lambda)$), a variable that accounts for the radius of the sphere, the wavelength of the incident light, and the relative refractive index of the sphere in its surrounding medium, Lorenz-Mie theory provides a continuous prediction of angle-dependent scattering, as well as various Mie "efficiencies," namely the extinction, scattering, absorption, and backscattering coefficients. In a simulation of scattering by a composite containing many spherical scatterers, Lorenz-Mie angle-dependent scattering may be addressed at each particle and summed into the global scattering result. Use of Lorenz-Mie theory as a scatter source for inclusions comes with its benefits as well as a major caveat. The use of a size index that scales the sphere size by the size of the wavelength means that spheres of any arbitrary size may be used, thus, Lorenz-Mie allows for generating scatter sources for inclusions below the geometric limit in length scale. The caveat is that Lorenz-Mie theory, in its simplest form, will only give an accurate scattering profile for spherical particles, and most pigments, nanoparticles, and composite inclusions are indeed not spherical. However, Rother and Schmidt have developed a discretized Mie-formalism, or DMF, which is essentially the solution of the Helmholtz equation performed by using the Method of Lines (MoL). Their treatment extends the Lorenz-Mie methodology to be applied to axisymmetric particles, such as shifted spheres and ellipsoidal particles. For more complex axisymmetric inclusion or particles, as well as statistically randomly shaped particles, finite element methods that solve for the Maxwell equations at discrete mesh nodes overlaid onto the system geometry must be used to generate the scatter profiles.

Lastly, the irregular (yet very real) asymmetrically shaped particle which represents a difficult scattering situation, shown in Figure 3-6. Here, it is of course still possible to break down or reduce

the geometry into a very large number of flat surfaces that may be addressed using Snell and Fresnel equations, but the arduous task quickly becomes overwhelming. It's much simpler, and more accurate, to solve the system of the Maxwell equations, which appears a hassle at first, but represents the most prudent approach in the long run. Especially with modern finite element computer software packages that automate the calculation and solving, the Maxwell equation treatment is most desirable for systems containing these irregular but very real scattering geometries.

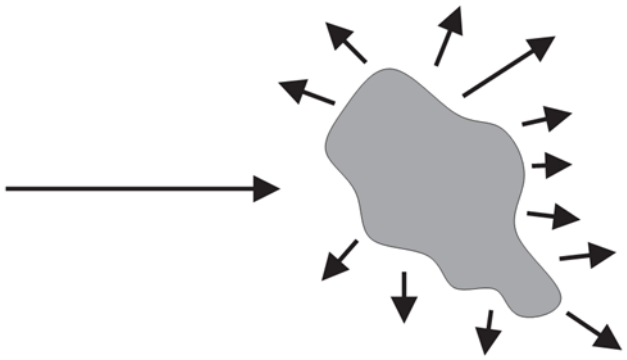

Figure 3-6. Real particles exhibit high asymmetry, and are best solved for using a complete, analytical solution to the Maxwell equations.

3.6. Finite element solutions of the Maxwell equations for electromagnetic radiation transport

Finite element analysis of the propagation of electromagnetic waves is a commonly used technique for understanding the scatter and radiation transport behavior of electromagnetic waves. Several limitations of the simulation of systems with complex geometry and large length scales include difficulty in finite element convergence and immense computer memory requirements. One solution is to use the ray tracing techniques to track electromagnetic waves from distance sources until the wave impinges on a region containing an inclusion of size scale less than the tracked wave wavelength. This smaller subregion can be solved with finite element techniques to generate a new set of scatter photons that enter the simulation frame of reference on the outer surface of this

subregion and continue to be followed using the ray tracing technique until they again intersect a region containing subwavelength particles, or the ray reaches a detector.

The finite element program employed is COMSOL Multiphysics. The RF (radiofrequency) module is employed since the scale of the electromagnetic wave is on the same length scale as the scatter source. The Poynting vector (or energy flow) is used to scale the incoming photon weight to generate the outgoing photon source for photon tracking methods. The boundary source is exported from the finite element simulation and a new ray tracing trajectory is initiated. The detected photons out of the ray tracing simulation include those that never intersect a region that contains small particles added to those that are generated by the finite element solution on the surface of the region containing the small particles.

In the solution of the Maxwell equations for a sphere embedded in a dielectric medium, the effect of the magnetic portions of the equations are zero, except for in the case of particles with non-unity magnetic permeability, such as iron or certain nickel alloy materials[1]. These materials are of interest in more esoteric coatings applications, such as the detecting of active corrosion processes with nanoparticles or pigments of said composition, which lose permeability as they oxidize and can serve as *in situ* quantifiers or indicators of corrosion onset.

This method of coupling ray tracking to finite element scattering predictions offers several advantages. The proportion of the measured light that is actually scattered by the various small particles can be tallied. This allows the quantification of the impact of the particles on the overall system scatter response. Additionally, the finite element solution generates detailed electromagnetic fields that may be of interest when investigating the impact of changing the shape or composition of inclusions within the scattering subregion, coupled with the global ray tracing result to quantify how that affects the overall system response.

The exemplar polymer nanocomposite used to calibrate and qualify our model will be a generic polymer coating containing a narrow slab of specifically placed, aligned, and cylindrical nanofibers, each located in its own subregion to be analyzed by finite element analysis, as shown in the cartoon in Figure 3-7. The region containing nanofibers is sandwiched between to polymer layers having the same composition of the polymer in the composite layer. The entire polymer composite is adhered to a substrate and is open to air on the topside. The nanofibers may be fully embedded in polymer matrix, or will be partially or fully delaminated within the matrix. In the case of delaminated fibers, air voids will exist between the matrix and the fiber. Delamination of reinforcing fibers in polymer composites greatly reduces the mechanical strength and integrity of the material. Thus, a working knowledge of the relationship between angular-dependent scattering by a composite and the electromagnetic signature produced by embedded, partially delaminated, or fully delaminated inclusion regions in the material will provide a means of non-destructive evaluation for such materials, and may lead to a detection method that predicts material failures before catastrophic failure occurs.

Figure 3-8 shows representative scattering output from a solution of the Maxwell equations for electromagnetic scattering by a 2-dimensional circle representative of a circular fiber or sphere cross-section.

Here the scattering inclusion is 300 nanometer diameter SiC fiber embedded in PMMA, an exemplar fiber-reinforced nanocomposite material, where the indices of refraction for SiC and PMMA at an incident radiation of 590 nm (used here as incident radiation energy) are 2.55 and 1.55, respectively.

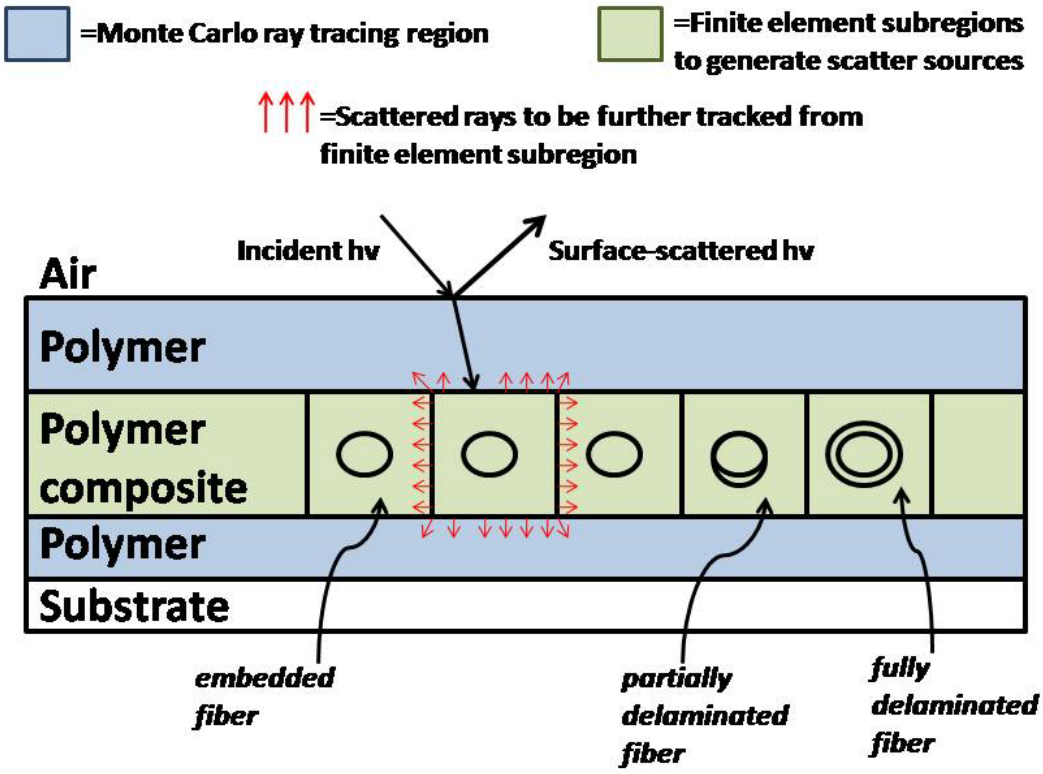

Figure 3-7. The exemplar composite system used to verify the model contains regions of pure polymer and regions of polymer composite containing nanofibers which may be fully embedded, partially delaminated, or fully delaminated. Finite element simulations predict the scatter in the composite region, while Monte Carlo ray tracing simulates the radiation transport in other regions of the system. First presented at TMS 2010[2].

When an incident photon impinges on the nanoscale scatterer, the photon is seen or felt by the scatterer as a moving wave front. After the scattering simulation, integration is performed around the circumference or enclosing surface of the finite element simulation space to determine the outgoing rays and their respective weights. The accuracy and fineness of this quadrature procedure will have a direct effect on both the computing time and the accuracy of the final scattering results for the bulk composite materials.

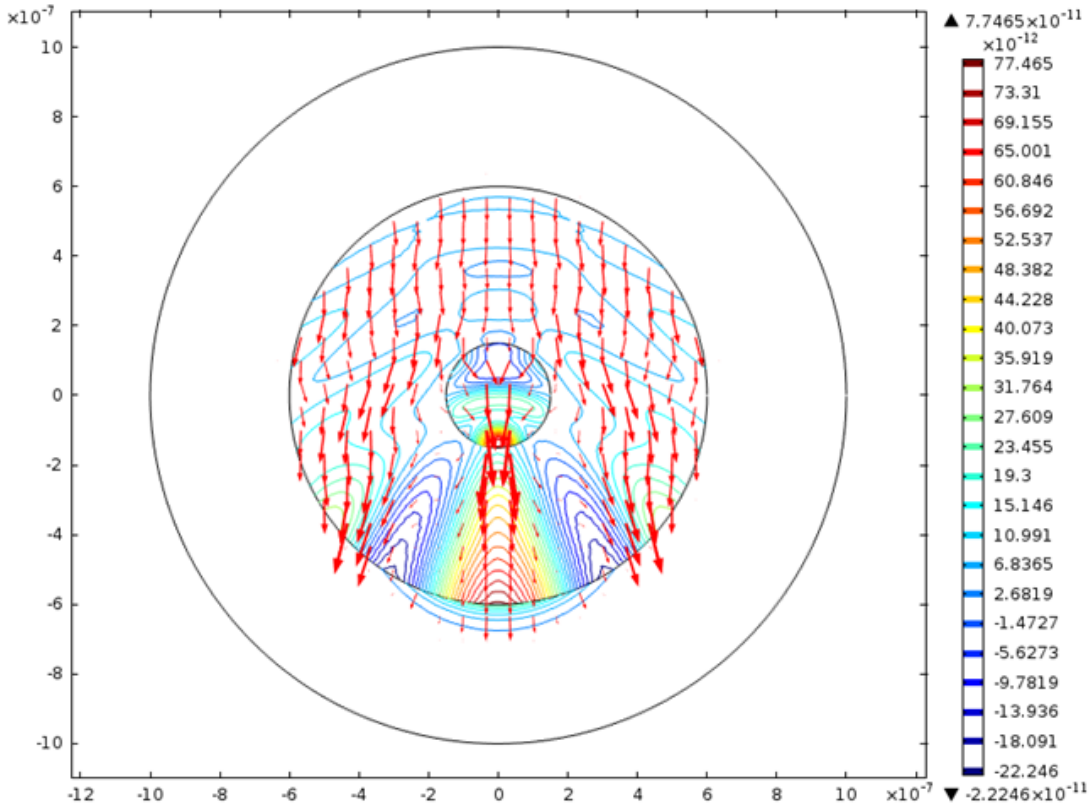

Figure 3-8. Representative scattering output from a finite element simulation of light scattering by a circular SiC nanofiber embedded in PMMA. The arrows and contour map in the figure represent the time averaged power outflow in W/m^2, and are used in the quadrature step of the multiscale hybrid simulation to generate scattered outgoing rays. The axis dimensions are given in meters.

The scattering by a nanoscale scatterer below the geometric limit is a complex process, where ray tracing approaches and simple solutions to Snell's law fail in their simplicity. This is because the impinging wave is not a point source like a photon on a large flat surface, and the scattering event is not a snapshot in time like a large scale ray tracing simulation is reduced to. Rather, here, the size and time scales are small enough that one can observe the scattering event happen as an electromagnetic wave approaches, reaches, passes through, and leaves a nanoscale scatterer. Events like internal wave interference and eddy currents must not be avoided at this scale

of observation. During this entire event the scattered field caused by the scatterer and wave interaction is being formed and also propagated out into the matrix simultaneously.

The outer circle boundary in Figure 3-8 is a Perfectly Matched Layer (PML). The PML minimizes unphysical reflections of the scattered electromagnetic wave is it leaves the model domain. That is, the PML prevents internal reflections in the finite element region that would result from the model domain being surrounded by a real physical wall. This allows for the extrapolation of scattered radiation into other domains, either in the finite element domain or in the geometric domain. For the PML to properly perform its function, it must be far enough away from the scatterer included in the domain, usually a certain fraction of the incident wavelength, as well as the characteristic length of the evanescent wave outside of the PML. That is to say, the PML should not be large enough to capture any appreciable decrease in amplitude that an attenuating wave travelling through a medium might exhibit due to Beer's law. The radius of the outer circle of the PML does not have any significant effect on the simulation, as long as appropriate meshing densities are met; approximately 5-6 mesh elements wide.

In short, the PML ensures that the scattered field from an inclusion or scatterer is almost completely transferred out of the local simulation space before what remains of it reflects on the exterior boundaries of the model, allowing a near-unity field to be carried out of the finite element domain and into the geometric optics regions of the complete model.

In light scattering simulations pertaining to coatings science, it is almost always the scattered field that is of interest. Indeed, the scattered field is what gives rise to color and appearance phenomenon such as gloss, color, and haze. If computing for the incident field that passes through the domain and isn't affected by the scatterer is unnecessary, then computational time may be saved by only computing the scattered field. In COMSOL solution analysis, the scattered field is called the relative electric field. The total electric field is always available, and for the scattered-field

formulation this is defined as the sum of the scattered field and the "non-scattered" or "non-interacting" incident field.

So effectively, for nanoparticle scattering, carrying over the scattered field calculation only (i.e. the relative electric field), is in practice equivalent to treating a wave source as a point source impinging on the particle (actually, a point source having the width equivalent to the diameter of the scatterer.

Electromagnetic analysis on a macroscopic scale is an issue of solving the Maxwell equations given an appropriate set of boundary conditions. Solving the Maxwell equations can become quite a complicated task when a material is heterogeneous, anisotropic, nonlinear, or dispersive. With heterogeneous materials, such as coatings or composites, the constitutive parameters vary with the spatial coordinates so that different field properties dominate the material in different locations of the material's structure.

3.7. Varieties of scattering inclusions

Many varieties of inclusions or scatterers can be studied quite simply by switching out or adding lines of code to the overall model that refer to or call the scattering profiles of finite element simulations that contain said unique inclusions. For example, the scattering profiles in Figure 3-9 are for a pearlescent pigment that is 300 nm long-axis length mica coated with TiO_2 and is a representative example of a pearlescent pigment. Previous literature studies only use a flat multilayer model to simulate or predict multilayer pigment scattering properties[3]. This present approach incorporates real curvature geometry that exists on length scales below the geometric limit. Here, in Figure 3-9, the color flop may be observed as the angle of incident radiation increases from 0 to 20 to 70 degrees, where at 70 degrees incident light is no more being scattered than it is being transmitted.

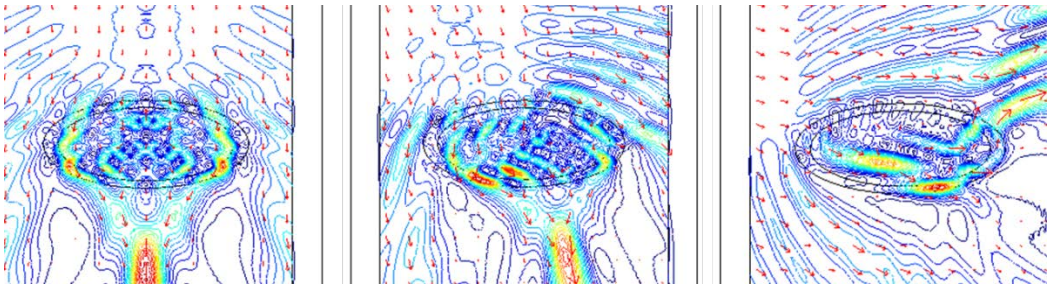

Figure 3-9. Simulated scatter response for a 300 nanometer mica flake coated with titanium dioxide, being impinged on by 590 nm incident radiation at 0 (left), 20 (center) and 70 (right) degree angles of incidence.

Appearance and scattering behaviors are very angle-dependent, and this method provides a way to characterize single pigment angular dependence to deduce trends in composition and to optimize the geometry of pigment in the manufacturing process, and also provides a means for incorporating this new, complex geometry or layered composition into a full-scale model for EM radiation transport. Utilizing finite element methods allows for incorporation or switching of the scattering solutions of very complicated pigments (structure or composition), as well as complicated orientations, groupings, spacings, or clustering of these pigments. In Figure 3-9 above, contour and arrow plots are time averaged power outflow.

Air voids are a common nuisance in many coatings and composite applications. These may be simulated by any number of gaseous void geometries included in the simulation space. A useful application of air void scattering is to include the presence of voids near fibers or pigments to simulate changes in electromagnetic signature before and after fiber debonding or onset of the critical pigment volume concentration, when there is no longer sufficient polymer binder to completely wet the embedded pigment. Both situations are undesirable, and both may be easily addressed by finite element simulations. Such incorporation may lead to improved non-destructive evaluation and assessment methods.

Finally, heterogeneous phases in copolymer blends may also be investigated using finite element approaches, given the refractive index of the separate phases are nonequivalent. Coupled with molecular and coarse grained simulation tools like dissipative particle dynamics approaches for phase separation of material blends, this approach may lead to another new class of non-destructive interrogation and assessment methods.

3.8. Extension of the inclusion scattering approach to 3D inclusions

The finite element solution approach to inclusion scattering is best performed when the inclusions have enough symmetry to afford a 2D representation, such as systems of unidirectionally-aligned fibers or spherical pigments where only one plane or "face" of a scattering solution is sufficient to probe the electromagnetic response. In situations where a full solution is desired, either for accuracy or for completeness, the finite element approach may be extended to three spatial dimensions, and the 3D scattering output may be entered into the global ray tracing code.

Here, a gold nanoparticle 200 nanometers in diameter is placed in a PMMA slab,. The 3D scattering profile is generated for parameterized wavelength values ranging from 380-780 nanometers. Due to the high degree of symmetry in the case of a spherical scatterer, the solution needs to be computed for only a portion of the total geometry. In this case a quarter sphere is used. Figure 3-10 shows the spherical sphere embedded in surrounding polymer matrix, which is in turn surrounded by a perfectly matched layer (PML) which prevents unrealistic internal reflections from occurring within the simulation space.

The model solves for the scattered field,. The background electric field is entered by the user. In this case the background plane wave is moving in the positive x-direction, and the electric field is polarized along the z-axis.

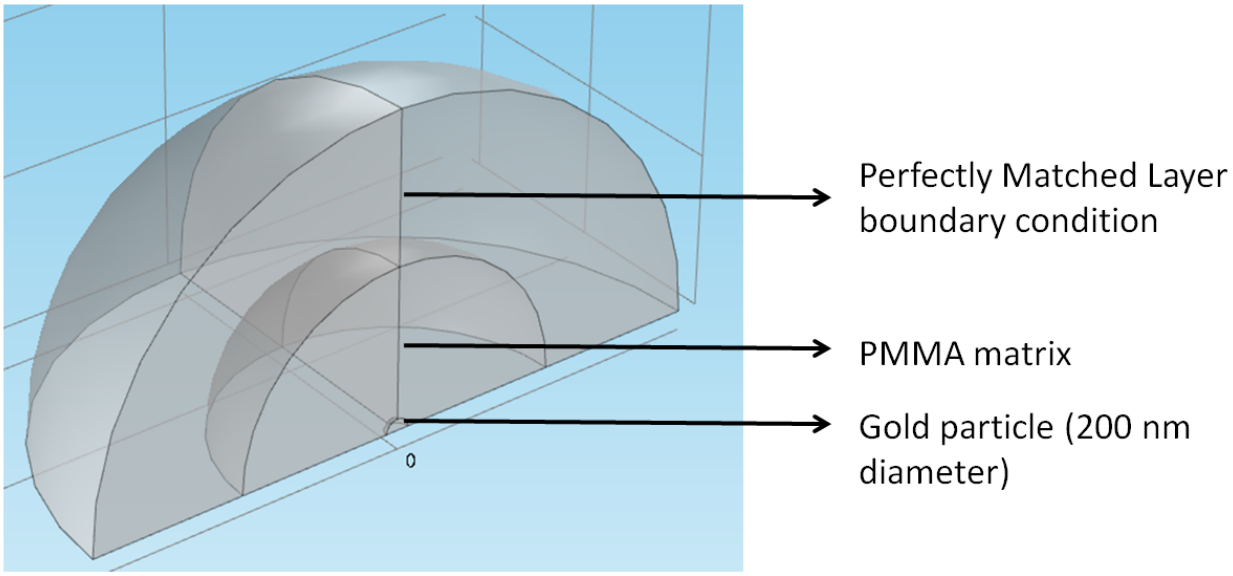

Figure 3-10. Problem geometry for a quarter sphere embedded in PMMA and bounded by a Perfectly Matched Layer.

The default boundary condition is that of the perfect electrical conductor. This assumption applies to all exterior boundaries that are perpendicular to the polarization state of the background electric field. During the scattering solution computation, the total heat loss in the sphere is incorporated as a volume integral of resistive heat losses over the nanosphere domain.

The spectral complex dielectric constant is needed as an input parameter for the sphere. These values are interpolated from existing literature data for the real and imaginary parts of the parameter [4]. Unknown material properties for the PMMA polymer matrix are calculated using the Bicerano's Snythia module for polymer property prediction, as implemented in Accelrys Materials Studio[5]. A variable mesh is used within the simulation space. The maximum mesh element size is set as $\lambda/6$ to allow for a practical balance of convergence likelihood and result precision.

Figures 3-11, 3-12, and 3-13, show some of the graphical outputs from the 3D scatterer simulation for the 380 nanometer incident wavelength data set, as viewed in the x-y, y-z, and x-z planes, respectively. The figures show the time averaged power outflow (W/m^2) in volume, contour,

and arrow plots overlaid on top of each other. In general, it may be observed that incident radiation from the x-direction in general travels through the particle and leaves with a mostly straightforward bearing in the x-direction.

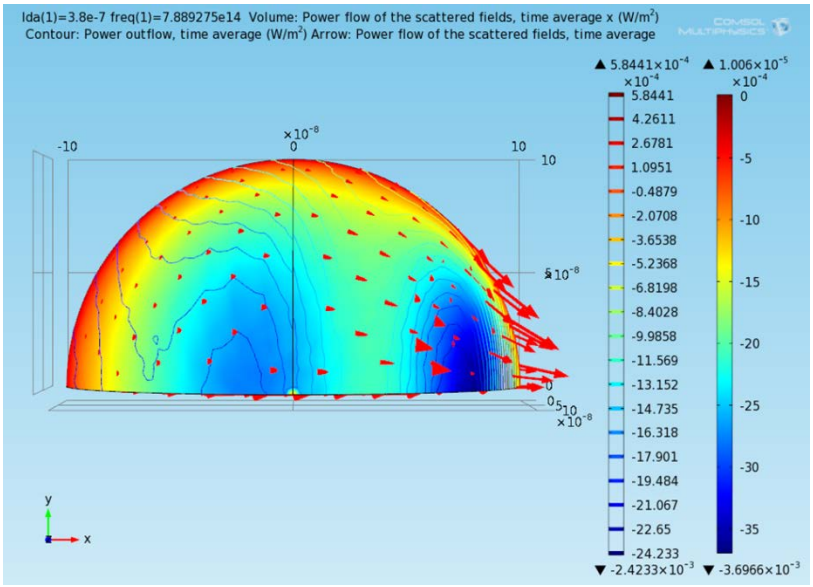

Figure 3-11. Scattering simulation results for a 3D gold sphere in PMMA, viewing only the surface of the sphere in the x-y plane.

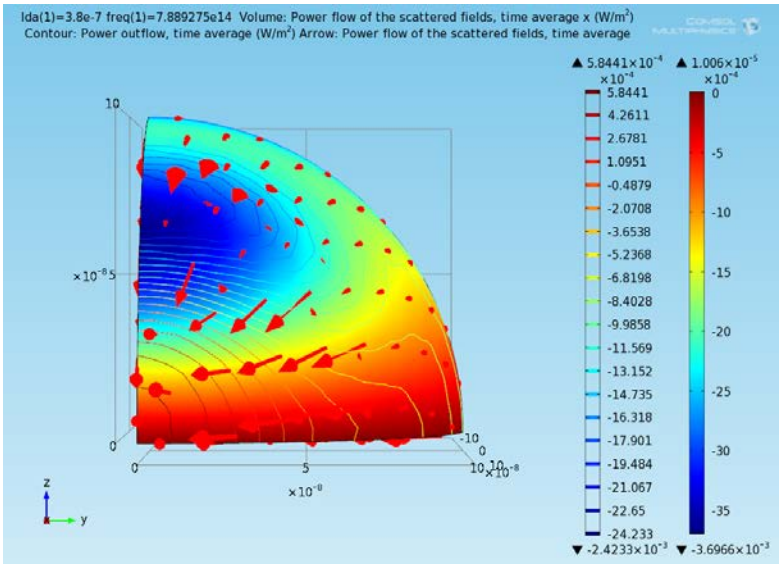

Figure 3-12. Scattering simulation results for a 3D gold sphere in PMMA, viewing only the surface of the sphere in the y-z plane.

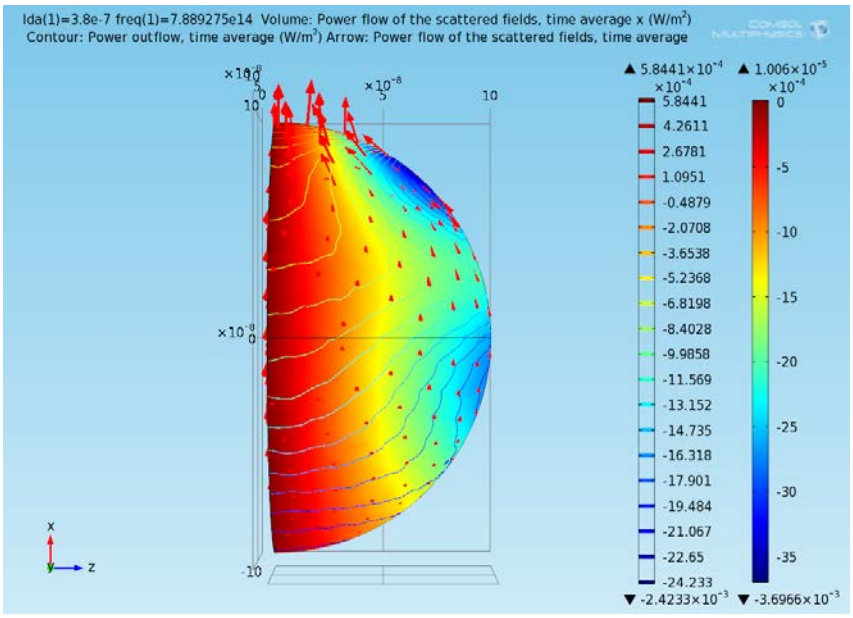

Figure 3-13. Scattering simulation results for a 3D gold sphere in PMMA, viewing only the surface of the sphere in the x-z plane.

Figure 3-14 shows the same output as before, but now viewed only x-z plane, so that comparisons form results of different incident wavelengths may be made. Figure 3-14 shows that forward scattering dominates for incident wavelengths from 380 to 530 nanometers, while evanescent waves dominant the scattering field at incident wavelength of 580 nanometers, due to a large amount of total internal reflection occurring at the sphere's boundaries. The forward scattering regime recommences at wavelengths greater than 580 nanometers, but the average scattering direction becomes increasingly side-scattered as the incident radiation wavelength approaches 780 nanometers.

The arrow plot overlaid in the 3D scatter result plots may be used to perform quadrature on the 3D scattering surface along the surface of the inclusion. Those weighted arrow photon portions may be transferred to the overall ray tracing multiscale code.

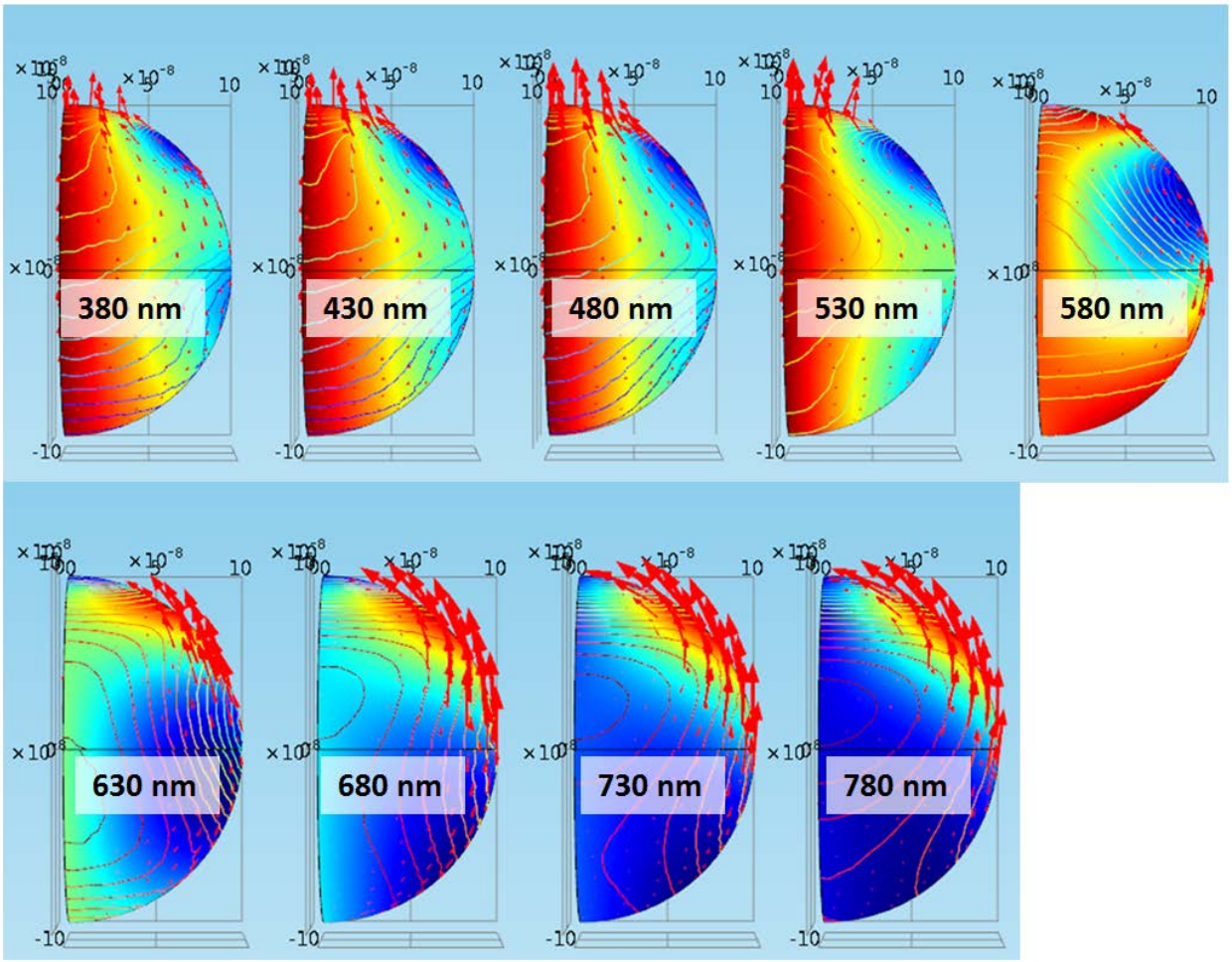

Figure 3-14. Scattering simulation results for a 3D gold sphere in PMMA, with increasing incident radiation wavelength from 380-780 nanometers. As incident radiation wavelength increases, the dominant scatter mode changes from forward to evanescent to side scattering situations.

The 3D inclusion approach affords a level of detail and insight that is unobtainable in the 2D result. This is another example of a case where ray tracing optics solutions would fail to predict the nuanced scattering behavior that is observed in the more analytical solution.

3.9. Further reading

For more information on bulk, volume, or inclusion scattering, one is firstly directed to the seminal book by Van de Hulst[6], as well as the similar yet updated treatment given by Bohren and

Huffman[7]. Both sources use as a foundation the classical electrodynamics math put forth in such classics texts as Jackson[1], Schwartz[8], and Shadowitz[9].

3.10. Conclusions

The tools needed to construct an appropriate multi-scale model for the global electromagnetic radiation of polymer composites containing various sizes and shapes of inclusions have been discussed. As the length scale of inclusions in composite materials continues to shift lower and lower into the nanometer range, models are needed that accurately predict the scattering profile of inclusions that are below the geometric limit and that are also capable of having myriad geometries such as spheres, ellipsoids, flakes, or cylindrical fibers. Lorenz-Mie scattering theory works well for spherical inclusion of all sizes, while a discretized Mie-formalism and finite element methods are suitable for predicting the scattering of various axisymmetric inclusions. When scattering by a single inclusion is adequately simulated, the summation of the scattering results of a large number of randomly or specifically placed inclusions in a material slab may predict global properties of the composite material, most notably the electromagnetic signature of the composite. A fully-realized version of the model will thus predict the visual appearance of the composite at various angles of observation while being illuminated by a variety of electromagnetic radiation sources. The composite may contain specifically placed inclusions of specific shape and size, or may be randomly placed and randomly sized, as determined by particle size distribution and loading level of the inclusion material. Preliminary qualifications of the model have been performed, wherein the system being studied is a polymer slab with a layer of nanofiber-reinforced polymer contained within it. The decrease in adhesion between fiber and matrix will lead to the creation of air voids around the fiber, which will result in a different electromagnetic signature which may be used as a non-destructive evaluation method for such similar, real-world composites.

3.11. References

1. Jackson, J., *Classical Electrodynamics*. 1998, New York, NY: Wiley.
2. Sapper, E. and B.R. Hinderliter. *Monte Carlo Method for Electromagnetic Scattering Incorporating Finite Element Methods to Generate Scatter Sources for Nanoscale Inclusions in Composites*. in *TMS 2010*. 2010. Seattle, WA.
3. Maile, F.J., G. Pfaff, and P. Reynders, *Effect pigments - past, present, and future.* Progress in Organic Coatings, 2005. **54**: p. 150-163.
4. Johhson, P.B. and R.W. Christy, *Optical Constants of Noble Metals.* Phys. Rev. B., 1972. **6**: p. 4370-4379.
5. Bicerano, J., *Prediction of Polymer Properties*. Plastics Engineering, ed. D. Hudgin. 2002, New York: NY: Marcel Dekker, Inc.
6. van de Hulst, H.C., *Light Scattering by Small Particles*. 1957, New York: John Wiley & Sons, Inc.
7. Bohren, C.F. and D.R. Huffman, *Absorption and Scattering of Light by Small Particles*. 1983, New York: John Wiley & Sons. 530.
8. Schwartz, M., *Principles of Electrodynamics*. Dover Books on Physics. 1987, New York, NY: Dover.
9. Shadowitz, A., *The Electromagnetic Field*. Dover Books on Physics. 2010, New York, NY: Dover

CHAPTER 4. SIMULATION OF LIGHT SCATTERING BY A NANOCOMPOSITE MATERIAL: A HYBRID MULTISCALE APPROACH TO ELECTROMAGNETIC RADIATION TRANSPORT

"All we do is draw little arrows on a piece of paper – that's all!"

– Richard P Feynman[1]

4.1. Introduction

After introducing surface and inclusion scattering, it naturally follows that one consider combining the two approaches into a comprehensive modelling approach for light scattering simulation. The hybrid and multiscale scattering approach presented here uses the simplification that surface scattering will be performed by geometric optics, as shown in the above cases, and that any and all inclusion scattering will be treated using the complete solution to the Maxwell equations. This is not as computationally expensive as it initially sounds; each inclusion scattering profile only needs to be computed once, while the results from such a one-off simulation are held in a numerical matrix that is regularly called upon by the overall geometric optics framework. Thus, all transport between scattering events within the material will occur through geometric optics ray tracing processes. This means that incident radiation will strike the surface of a material while acting as a particle, be partially absorbed and travel to an inclusion as a particle, and interact with an inclusion as an incident wave which produces scattered photons behaving as particles, each of which will further propagate through the material as particles. This approach makes full use of the flexible nature of wave-particle duality that is inherent to light scattering problems.

Scattering of light by a coating has a significant impact on the perceived quality of that coating. Light scattering metrics have also been used as a nondestructive measurement surrogate for

the protective state of the coating. Light scattering at the surface and subsequent reemerging from within a coating is a function of wavelength and results in the measured gloss and color of a surface. Monte Carlo ray tracing methods have been used to calculate the transport of nuclear radiation particles and high energy electromagnetic waves since the methodology was developed in the 1930's by Ulam, Fermi, von Neumann, Metropolis and others. Beyond applying Monte Carlo methodology to coating appearance, the technique also lends itself to calculations of curing efficiency and cure distributions in light and UV curing technologies. Image recognition and identification of infrared signatures represent additional applications. A 3-dimensional ray tracing model is presented here, based on geometric scattering assumptions. The new scattering model allows for the simulation of scattering of light by object that is on the same size scale as the wavelength of the incident light. The light scattering distribution for various simple coating states are compared to other models, such as Bennett and Porteus and explicit Mie theory calculations.

Electromagnetic radiation scattering is, in almost every case, the result of incident radiation interacting with various types of interfaces. The complexity of the scattering phenomenon at a given interface is determined by the geometry and composition of the entities located there. In the field of coatings and polymeric materials, these interfaces are usually composed of polymer matrix, pigment particles or fibers, air, and the substrate that the coating or composite is applied to, in differing geometries and spatial arrangements. The transport of electromagnetic radiation in polymeric composites and organic coatings is responsible for the entire set of visual properties and appearance characteristics of these systems. For example, the ratio of specularly reflected radiation that is scattered from a smooth or rough surface relative to the maximum possible specular reflectance at a given angle is the coating scientist's definition of gloss and, along with surface shadowing effects, will determine how glossy or hazy a composite surface will appear to an observer. Directional diffuse and uniform diffuse scattering arising from subsurface scattering by pigments, dyes, or other

inclusions determines the visual appearance (color) of a coating or polymeric nanocomposite. In traditional organic coatings, such as those used in architectural applications, scattering by pigment inclusions such as titanium dioxide and other mineral fillers, as well as scattering by air/polymer and air/pigment interfaces due to voids present in the coating, determines the hiding power of the coating, that is, how effectively a coating can block reflectance from a colored substrate. As a wider range of specialty pigments and inclusions becomes available, it becomes increasingly useful for chemists and material engineers to be able to predict with fair accuracy the electromagnetic signature that a novel composite, coating, or other material may exhibit. There are numerous methods available that are capable of simulating the scattering properties of single inclusions and even large clusters of inclusions, but very few comprehensive models are capable of doing so for a slab of composite material or coating with a real surface roughness and containing a large number of randomly spaced inclusions. Because of the random nature of inclusion location in real-world composite materials and the dependence of electromagnetic signature on global, as opposed to local, scattering properties, a stochastic and non-deterministic simulation is the best choice for modeling the scattering properties of these types of systems.

The choice of which mathematical approach will best simulate the electromagnetic scattering by inclusions in composite materials is highly dependent on the shape of the inclusion as well as its size relative to the incident radiation wavelength. For polymeric composites and coatings with inclusions significantly larger than the geometric limit, geometric optics or ray tracing may be used to simulate the scattering event, given that the inclusions are spherical or axisymmetric. However, in the case of pigmented coatings and polymeric nanocomposites, where at least one length scale of the inclusion species is shorter than incident wavelength, the geometric optics approximation no longer holds and other methods, such as the Lorenz-Mie scattering solution for spheres or finite element methods must be used. This chapter explains in detail how ray tracing and finite element simulation

methods will be used to aggregate the scattering by single inclusions into global results like the electromagnetic signature of a polymeric composite. In addition, this chapter will address the various methods of scatter source available to us, namely Lorenz-Mie scattering and finite element methods.

4.2. Simulations of bulk scattering through a homogeneous polymer slab

A deterministic ray tracing approach was applied to systems of unpigmented coating atop various substrates. Output from the simulations was used to construct ray tracing diagrams and determine what percentage of incident light reflects from the film in a specular fashion, as well as the diffuse contribution of reflected light. Figures 3 and 4 show the ray tracing diagrams produced from the striking of incident light at three different angles (20, 60, and 85 degrees) onto a 1 micron thick coating applied to nickel and silver substrates. The thickness of each ray is indicative of its weight, or percent of incident light. Table 4-1 provides the specular and diffuse reflectance values predicted by the model for the cases shown in Figures 4-1 and 4-2. Table 4-1 indicates that the specular weight is independent of substrate composition, as is expected. Differences arise in the diffuse contributions due to the different physical properties of the substrates, such as index of refraction and absorption coefficient. Further, trends in the data are easily noticeable; as incident angle increases the amount of diffusely scattered light decreases and the amount of specular reflected light increases. The largest change in these amounts occurs when an incident angle of 85 degrees is employed. Results from the slab on metal ray tracing simulation confirm that the general ray tracing approach is valid for polymer matrices.

Table 4-1. The ray tracing reflectance simulation predicts the contributions from specular and diffuse reflectance from a coating applied to different substrates. Originally presented at FutureCoat! 2008[2].

Substrate	Incident angle (degrees)	Specular %	Diffuse %	Specular %	Diffuse %
		(percent of incident weight)		(percent of total scattered weight)	
nickel	20	4.03	28.14	12.53	87.47
silver	20	4.03	92.25	4.19	95.81
nickel	60	8.92	27.51	24.49	75.51
silver	60	8.92	87.62	9.24	90.76
nickel	85	61.28	6.34	90.62	9.38
silver	85	61.28	34.66	63.87	36.13

4.3. Simulations of scattering by an embedded pigment using geometric optics and Mie theory: a comparison of methods

The discretized ray tracing model was then used to predict the scattering caused by a single 300 nm diameter TiO_2 pigment particle embedded in an organic coating. The purpose here is to determine how the results from geometric scattering compare to Mie theory calculations for inclusions embedded in a dielectric. If Mie theory calculations are more accurate, they may be used to directly generate the scattering probability and direction to be used as input in the coupled surface and bulk scattering model.

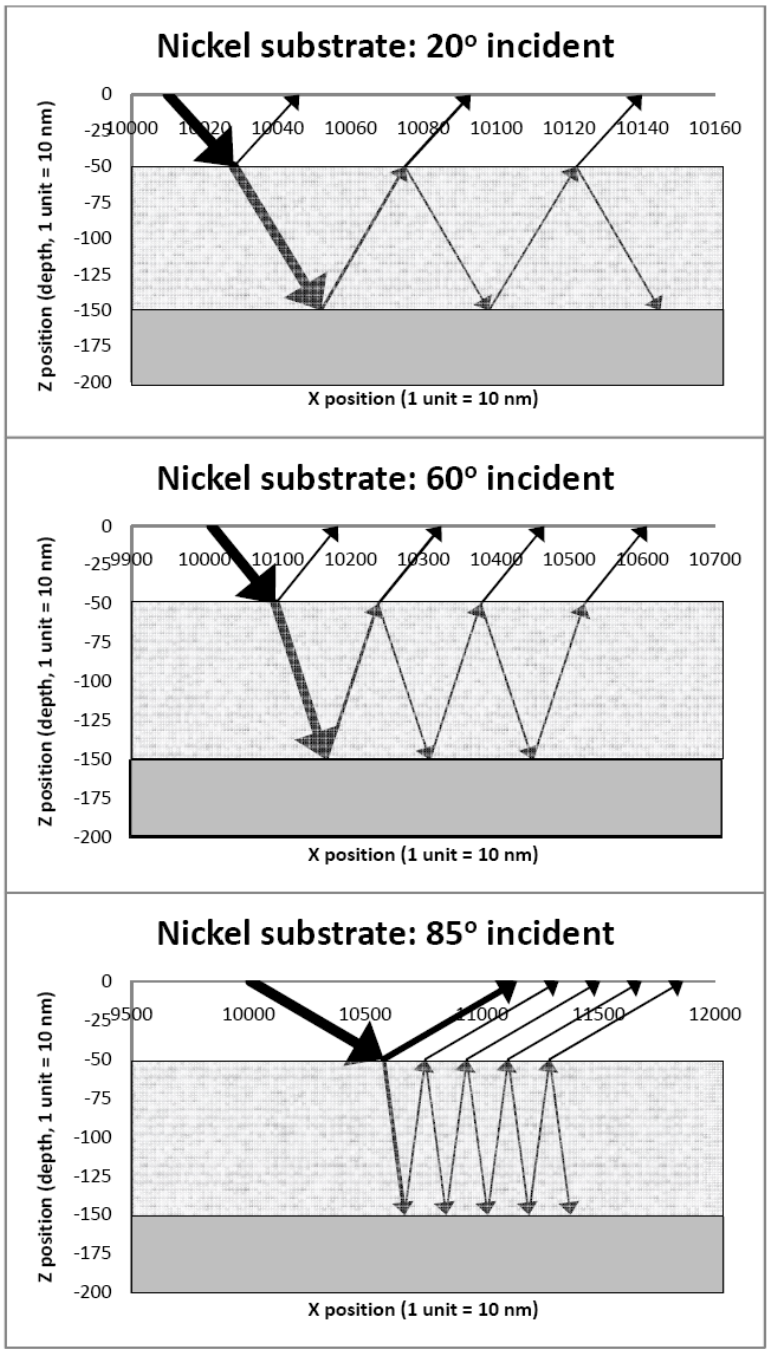

Figure 4-1. The bulk material reflectance ray tracing simulation allows for computing of specular and diffuse reflectance from various angles of incident radiation striking an organic coating applied to a nickel substrate. Arrow size and weight is proportional to ray or photon weight. Originally presented at FutureCoat! 2008[2].

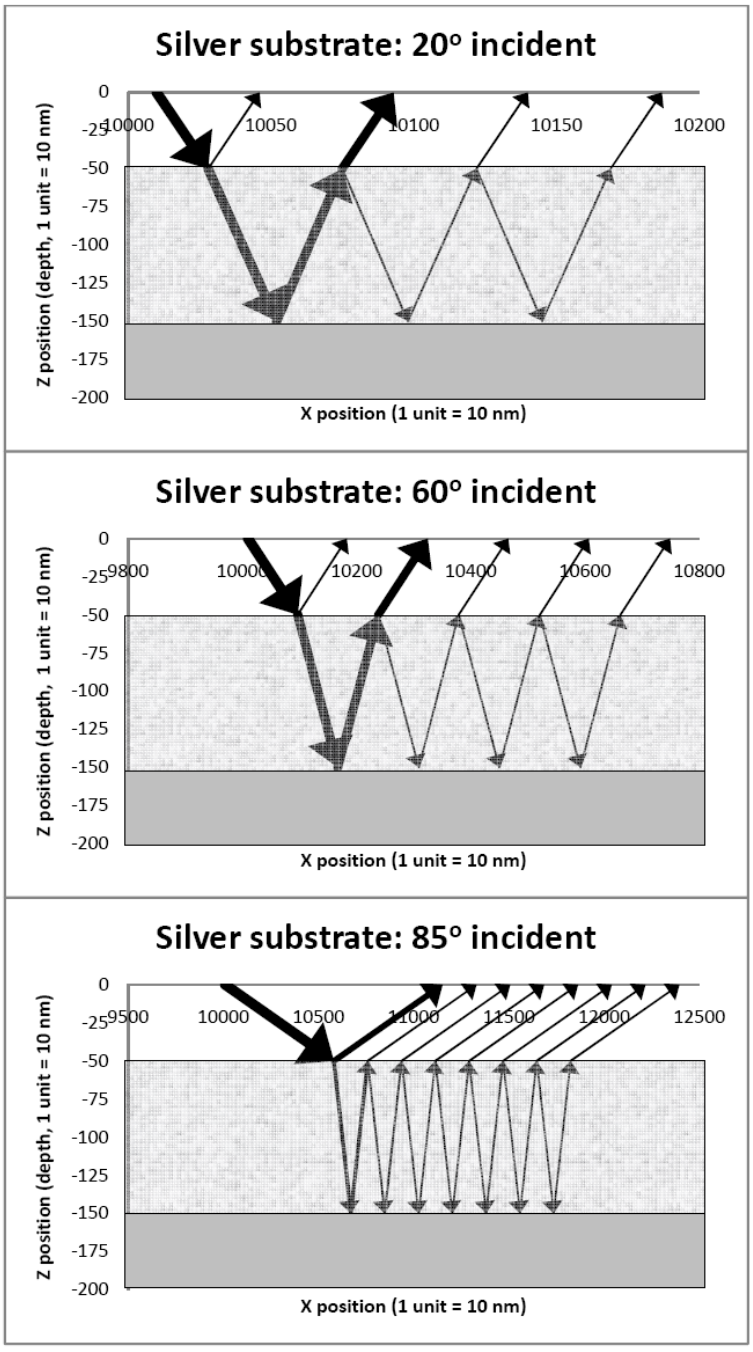

Figure 4-2. The bulk material reflectance ray tracing simulation allows for computing of specular and diffuse reflectance from various angles of incident radiation striking an organic coating applied to a silver substrate. Arrow size and weight is proportional to ray or photon weight. Originally presented at FutureCoat! 2008[2].

For the ray tracing / Mie inclusion calculation, the position of the incident light on the surface of the pigment was described in an angular fashion, as shown in Figure 4-3. A pigment sphere is located with its center at position *A*. Incident light arriving from position X_1 would strike the particle exactly normal to the surface inclusion surface in this frame of reference, with an angle θ of zero. If the incident light arrives from a position not normal to the surface, X_2 for example, the light strikes the pigment at an angle θ away from the normal around the circumference of the pigment. One should be careful to not confuse these angles with incident angles. Here, in every case, the incident ray approaches the pigment straight on. In preliminary studies the Y-position of the incident light is keep constant and the X-position is manipulated in order to observe scattering off the sphere at different angles. At this point, the simulation is essentially that of light scattering by a cylinder of infinite length.

Ray tracing from the simulation output provides a visual representation of the scattering by the pigment particle in the coating, shown in Figure 4-4. The data in Figure 4-4 is more approachable if one focuses solely on the light scattered off the surface of the pigment, shown in Figure 4-5, which indicates that a larger percentage of the incident photon weight is scattered as the angle of striking increases.

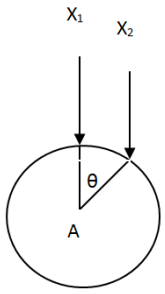

Figure 4-3. The ray tracing reflectance simulation directs incident light to different locations on the pigment's surface area. Here, the wave from X_1 strikes the pigment exactly normal to the surface and the wave from X_2 strikes the pigment an angle θ away from normal. Originally presented at FutureCoat! 2008[2].

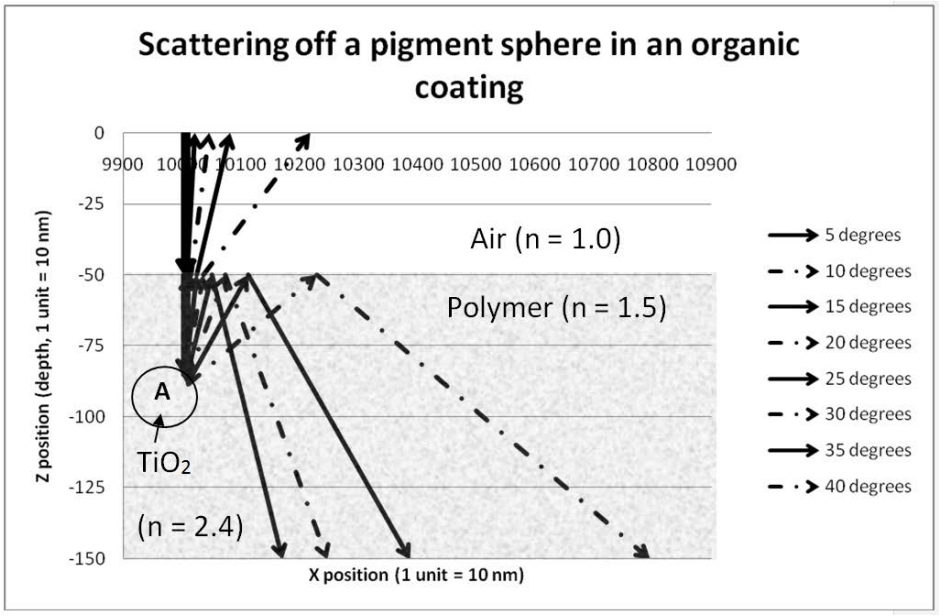

Figure 4-4. Ray tracing diagram of light scattered off a pigment surface. The pigment is centered at location *A*. The dimensions of the total simulation space pictured here are 10 microns wide and 1.5 microns deep. Originally presented at FutureCoat! 2008[2].

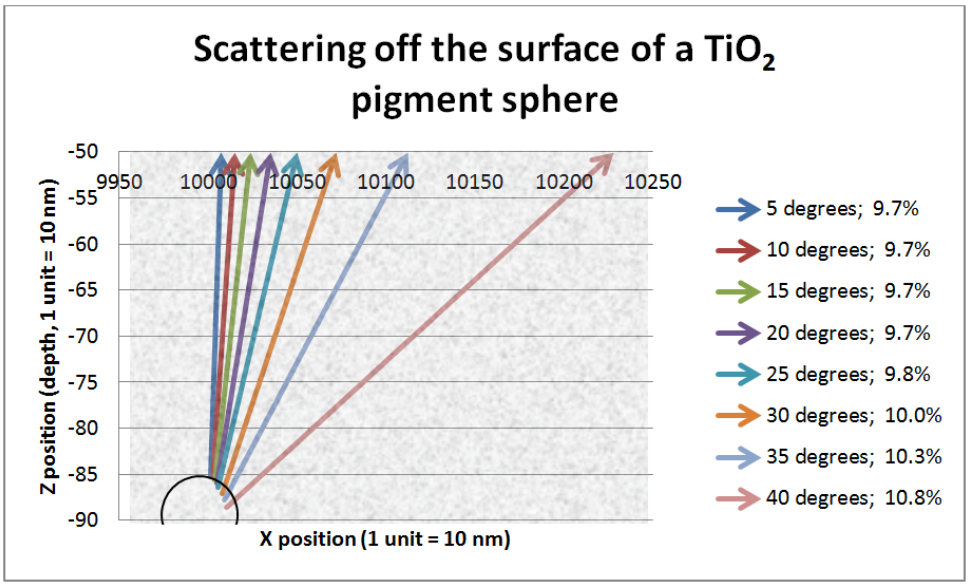

Figure 4-5. Ray tracing diagram of light scattered off a pigment surface. As the light strikes the surface at greater angles away from the overall problem geometry normal, the weight percent of scattered light increases. The dimensions of the total simulation space pictured here are 3 microns wide and 0.4 microns deep Originally presented at FutureCoat! 2008[2].

In Figure 4-5, rays striking the pigment at angles of or greater than 25 degrees to the normal are observed to strike the polymer-air interface at angles greater than the Brewster angle of 41.8 degrees. Thus, these rays are reflected back into and retained in the polymer matrix domain as propagating evanescent beams.

As mentioned earlier, a pressing matter is to correlate data from the geometric ray tracing simulations with concurrent Mie theory scattering calculations. Mie theory is capable of predicting the angular scattering of a spherical particle, as well as many other parameters, such as the scattering cross section, extinction coefficients, and polarization of scattered light for a pigment embedded in a monolith of constant refractive index. Figure 4-6 shows the angular scattering of a spherical titanium dioxide pigment particle. Incident light approaches at a 0 degrees heading, and it can clearly be seen that the bulk of scattered light is in the forward, 0 degrees direction. The azimuthal scale is normalized to the maximum amount of scattering in the forward direction, that is, at angle of zero.

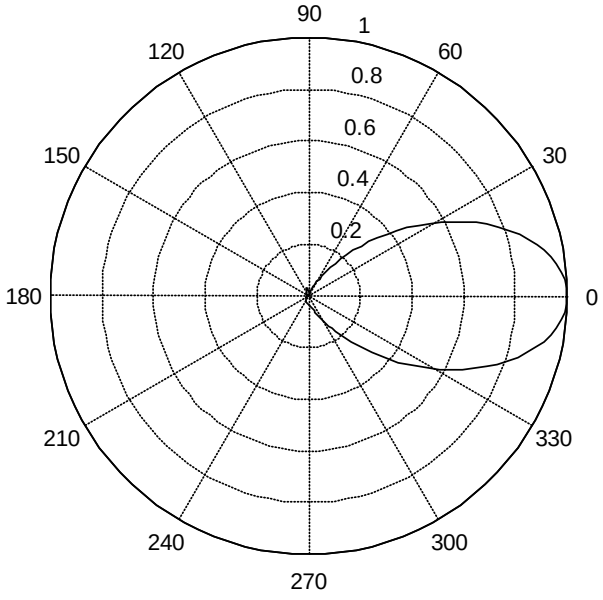

Figure 4-6. Mie theory prediction of the angular scattering of light by a 300 nm diameter titanium dioxide sphere embedded in a polymer coating. The azimuthal scale is normalized to the largest degree of scattering, which occurs in the forward direction at angle 0 degrees.

Data from Mie calculations used to produce Figure 4-6 may be compared to the scattering data from geometric optics calculations that were used to produce Figures 4-4 and 4-5. Figure 4-7 shows the angular scattering as a function of angle predicted by both methods.

Figure 4-7 suggests that the geometric model produces reasonably accurate results as compared to Mie theory. The investigation of different scattering prediction methods is necessary in order to understand whether future simulations with commercially relevant pigments, including flakes and ellipsoidal particles, could be done solely with ray tracing methods.

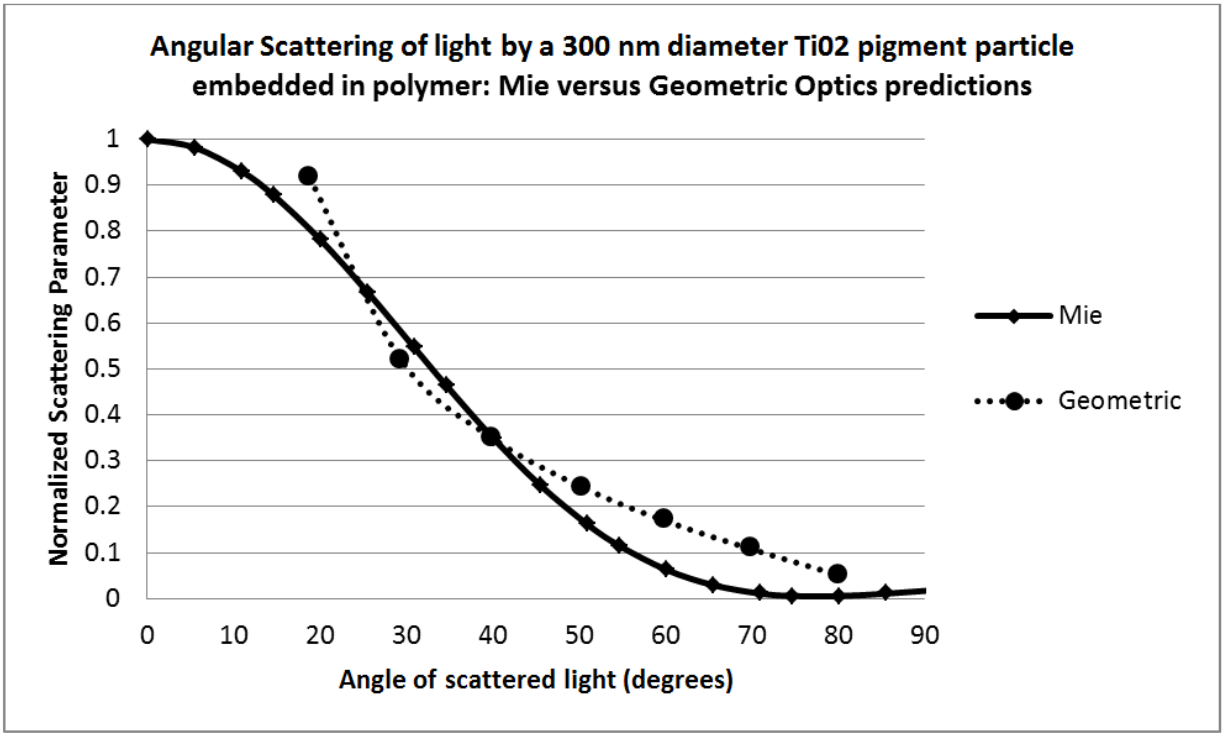

Figure 4-7. The current geometric model fits Mie theory results reasonably well. Originally presented at FutureCoat! 2008[2].

If not, then finite element models of electromagnetic wave transport will be employed in order to generate scattering cross section patterns for individual inclusions.

The current model is capable of performing geometric optics on a pigmented coating with pigments located at known positions within the polymer matrix. At this point, simulations of surface

degradation and light scattering are performed separately. Future development of the model will make use of Mie theory calculations and finite element solutions to the Maxwell equations to give scattering probability and distributions for pigment particles. An ultimate goal of this work is to marry the degradation and scattering simulations into a single model that is able to predict macroscale properties given a large number of input parameters such as pigment composition, size probability distribution, shape, pigment loading, physical properties of the substrate, and photon flux.

A "real" coating or composite system, with multiple components and many inclusions, can now be considered. The degradation portion of the model will predict the fraction of pigment particles exposed on the surface over time, and, coupled with the angular dependent scattering portion of the model, should provide reasonable estimates of gloss and color change measured at different angles as a function of weathering or exposure time.

4.4. Description of combined surface and bulk hybrid scatter model

The hybrid model for nanocomposite scattering presented here represents a marriage of the surface geometric optics ray tracing model with a finite element bulk transport model that accommodates many sorts of inclusions and various scattering phenomena. There are two approaches to this hybrid, total-geometry model; discrete (or deterministic) and statistical (or stochastic).

In the discrete model the geometry of the system is strictly defined, including the surface topography and the precise placement and size of the inclusions in the bulk matrix. This model is useful for applications where a specific surface texture is of interest (patterned or etched ridges, grooves, or other templated surfaces with directionality in either one or two dimensions), or where

the placement of inclusions in the bulk material is well defined, such as fiber-containing composite materials where the fibers are directionally or anisotropically aligned.

The second type of model is the statistical or stochastic model, where global and local statistical parameters are applied to the model either at the generation of the geometry, such as in the generation of surface roughness and height profiles, or on-the-fly and in real time, when individual scattering events occur in the bulk material. The statistical model relies on inputs such as volume percent loading of an inclusion such as a pigment or an air void, The statistical model employs a dice-rolling, random-number generator determination scheme at defined steps during the simulation run time to determine whether an inclusion is at a strikeable set of coordinates for any particular incident photon. Because of the nature of the statistical model, a well-defined dimensional volume of simulation space does not need to be defined, and photons being tracked will not be forced out of the tracking queue due to geometric or spatial limitations. In other words, in the statistical model every photon that enters will be tracked until it dies of extinction or exits the material simulation space, while in the discrete model some photons may continue out of the simulation space in lateral directions and will be lost or missing from the summed scattering results. The width of the statistical scatter model simulation space is undefined because the compositional input is volumetric and statistical, not discrete and spatially fixed.

The surface scatter treatment of both discrete and statistical hybrid approaches is the same simulation protocol as presented in Chapter 2. The geometric optics surface scatter model employs a solution to Snell's law and Fresnel reflection coefficient equations in a geometric optics formalism, where Snell's law gives the entrance angle of a photon incident on the material and the Fresnel reflection coefficient equations provide the weight of the photon or photon beam that is transmitted at that angle.

A necessary parameter of the statistical model is the path length that a photon will travel in a straight line in the material until a dice roll is performed to determine if the photon hits a scatterer or other inclusion, or otherwise continues to propagate in the direction it was originally travelling in. At each step length a random number generator is used in combination with volumetric input to determine if a photon hits an inclusion or not. The photons are tracked until they die of extinction or exit the material and collect at laterally and arbitrarily positioned detectors at a set height above the material. A detector in simulation space represents a photomultiplier where photons exiting the space may be counted and summed into results.

In both statistical and discrete material approaches, absorption through the dielectric matrix is included as a path loss using the simple exponential Beer's law, an approach that is justified if the imaginary component of the matrix complex refractive index is small; a fair assumption to make for many common engineering and coatings industry polymers.

4.4.1. Steps in a hybrid scattering simulation approach

The scatter model presented in the following pages comprises seven steps, outlined in Figure 4-9, and shown schematically in Figure 4-8.

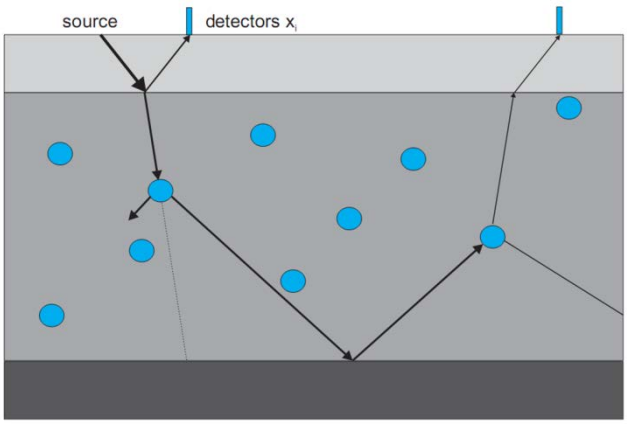

Figure 4-8. A schematic of the complete approach to multiscale electromagnetic radiation transport modeling. Originally presented at FutureCoat! 2008[2].

First, the geometry and/or composition of the material is defined. This is accomplished by discretely entering coordinates of inclusions, boundaries and interfaces, and surfaces in the discrete model, and by defining the statistical, compositional, and volumetric variables for the system in the statistical scatter model.

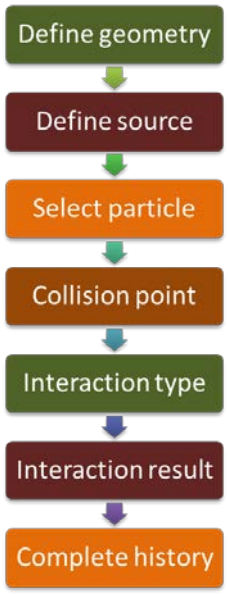

Figure 4-9. A schematic of the seven steps that complete the multiscale electromagnetic radiation transport modeling framework. Originally presented at FutureCoat! 2008[2].

Next, the electromagnetic radiation source is defined, its wavelength or bandwidth and number of photons to be tracked (roughly equal to the incident intensity or weight of the incoming photon packet). The angle of incidence to the global surface normal is defined for the photon trajectory of interest. Next, a photon is selected from the queue to track and a collision point is determined, either by determining a surface or interface strike point, or by taking a step defined in the dice roll input parameter once the tracked photon has entered the matrix of the bulk material.

The interaction type is then determined. In the case of surface or interface scattering the interaction type is a Snell reflection at a point that is assumed to be perfectly flat at that precise

location; this is the application of the Fresnel approximation. In the case of volumetric bulk inclusion scattering, the interaction type is determined by a dice roll. The interaction result is calculated after an interaction type is determined, either by solving Snell's and Fresnel's equations, or by calling the appropriate scattering cross-section profiles from a finite element simulation in the case of an internal, nanoscale scatterer whose size is below the geometric limit. The resultant scattered photon or photons are added to the photon queue and are tracked through the remainder of the simulation until they otherwise die off of extinction or become hopelessly attenuated to a cut-off value determined by the user, or exit the system and are collected at an arbitrary number of histogram-like laterally-positioned detector bins at the top of the simulation space, or located at precise position determined by the user; for example in a well-defined sphere, rectangle, or steradian of interest.

4.5. The significance of studying combined bulk and surface scattering in detail

There are numerous examples of scattering models available in the literature. The two-flux Kubelka-Munk model for example is a widely used model, but is insufficient for many finely structured or very large systems.

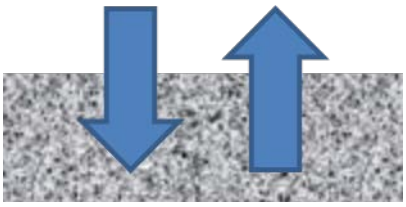

Figure 4-10. The two-flux Kubelka-Munk model for turbid media scattering forms the foundation of modern color mixing programs, but cannot accommodate directional pigments or spatial information in the bulk geometry.

The simplifying assumptions in the two flux model mean information is lost, both in the direct and in the inverse solutions of the problem. Reflectance may be predicted for a simple system, but detail about how individual scattering or surface components contribute to the overall electromagnetic signature of the object or material is not provided for. Combining the geometric optics and finite element approaches allows for a more complete model of scattering by complex composite materials, and encourages the designing, tailoring, or fine-tuning of very specific scattering properties, for example, surfaces that absorb only a limited spectral band or materials that scatter all incident radiation into a well-defined solid-angle in certain specified directions.

4.6. Important aspects and considerations of the hybrid scattering model

Most of the logistical complexity in coding this sort of scattering problem arises from photon accounting issues. Queuing systems used in the code must be flexible yet robust, and must translate exiting photons into meaningful results for the model to ultimately be effective.

The choice of quadrature method is also important, and will have a large effect on the accuracy and precision of the scattering results. The degree of quadrature that is chosen for inclusion scattering can range from 1 scattered ray per scattering event to 360 scattering ray portions for each radial degree direction (or more, 3600 rays, 36000 rays!), however the computational cost of increasing quadrature is exponential, because each scattered photon then goes on to produce more and more scattered photons until the attenuation cut-off is reached or the photon portions leave the simulation space and are collected at a detector. Quadrature can be performed statistically, by hand for a given example or special case, or randomly, by dice roll. Figure 4-11 shows an example of scattering quadrature performed by hand in a peak-biased approach, where the scattering profile generated by finite element analysis in Figure 4-11 (left) is translated to a linear graph of time

averaged power outflow (radiation intensity) as a function of outgoing scattering angle relative to the incident wave approaching from the 90 degree mark in the simulation space.

In Figure 4-11 (right) the quadrature is performed by picking five peaks in the power outflow distribution profile, and manually placing bins centered on each chosen ray that are integrated and incorporated into the photon queue as new photon packet trajectories. Integration performed under the area for each bin gives the corresponding outgoing photon weight for that bin. This process is repeated for each of the five photons in Figure 4-11, for a 300 nanometer diameter SiC fiber embedded in PMMA with incident radiation wavelength 590 nm.

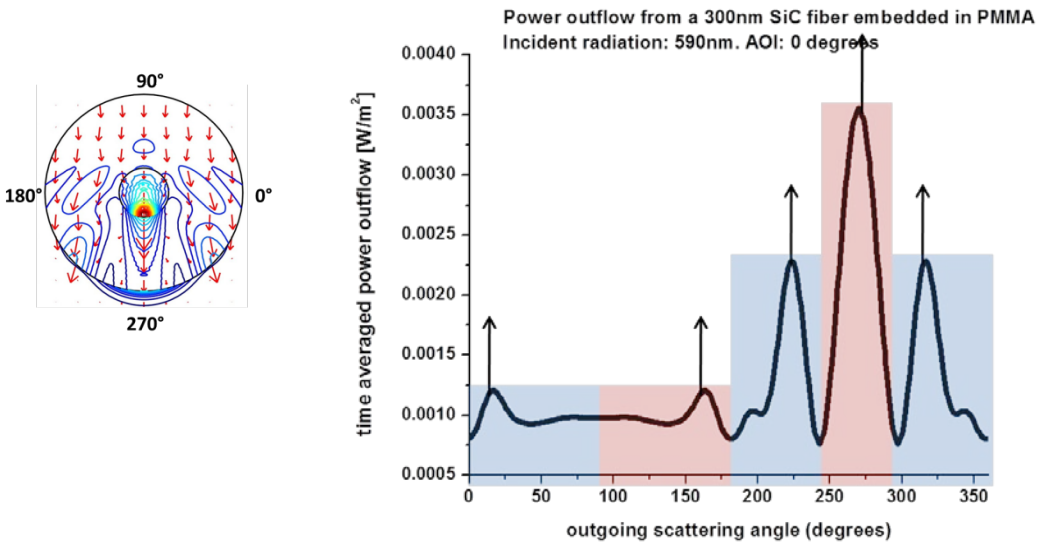

Figure 4-11. The scattering output from a single solution for an embedded inclusion (left) undergoes manual quadrature by hand to produce the 5 outgoing scattered rays in the plot of the power outflow versus outgoing scattering angle (right). The integrated weights for the 5 sections of the outflow plot are the relative photon weights that are passed on to the bulk transport code in the multiscale model. Originally presented at TMS 2010[3].

Finally, the point of origin of scattered rays must be decided on in advance. This is the physical location that scattered rays will originate from in the model. From a numerical standpoint,

scattering events should occur in a location that is ultimately simple to track. It helps to make a geometric assumption here to aid the photon accounting in the model and also to skim some complexity from the number crunching and model formulating. Thus, the model assumes that the scattered rays originate at the center of the scatterer. This is in opposition to the complex case, where scattered rays leave the inclusion at the inclusion boundaries or outer peripheries, which is a simple task in the case of a perfect sphere or circular scatterer, but becomes very difficult, arduous, or intractable in the case of a real, irregularly shaped scatterer. It is necessary to define where, relative to an inclusion's position, the incident ray converges to and where scattered rays or portions of rays originate from. Due to the sub-geometric limit scale of inclusions, to relegate scattering to the perimeter of these inclusions is an undue assumption that neglects the fact that light waves are passing *through* these materials and not simply "bouncing off" them. To assuage this problem and geometric complexity when dealing with real shaped highly asymmetric and irregular particles, all scatterers are treated locally as points, where photons acts centripetally when striking or approaching the object, and scattered photons act centrifugally when leaving or radiating outwards from the inclusion. This will be the treatment regardless of particle shape, as indicated in Figure 4-12.

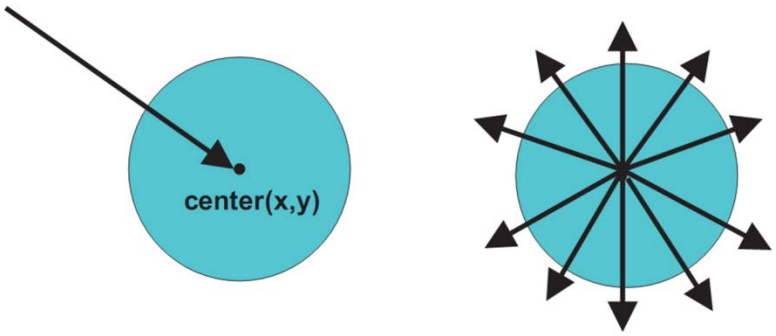

Figure 4-12. When transferring photons from the bulk to the inclusion scattering regimes, incoming photons are assumed to act centripetally, and outgoing photons are assumed to act centrifugally, regardless of scatterer geometry.

4.7. Results: single fiber case study

An example of the total hybrid approach to the electromagnetic radiation scatter by a nanocomposite material is provided in Figure 4-13, where the scattering inclusion is the same as in the previous example for quadrature, that is, a 300 nanometer diameter SiC fiber embedded in PMMA being impinged by a ray of 590 nanometer wavelength photons. Recall that the surface media characteristics are arbitrary and can be changed by simply changing two parameters; the refractive index n and the extinction coefficient k, and by defining the material surface roughness with the statistical parameters rms and autocorrelation length. The images in this figure are most certainly not drawn to scale; otherwise this simulation space would represent only a ~2 micron thick coating of PMMA.

Figure 4-13 shows the partial path that an incident beam of photons takes while interacting with a slab of PMMA on an aluminum substrate. The PMMA slab contains a cylindrical SiC fiber at an arbitrary depth, and the fiber has properties n and k. An incident beam of photons is aimed towards the PMMA surface at an incident angle 20 degrees to the global surface normal. In this case study, the surface at the polymer/air interface is ideally and perfectly flat, so scattering is determined by the straightforward solution of Snell's laws and Fresnel reflectance functions, which predicts that of the 100 incident photons, 4 are reflected specularly and leave the system of interest after exactly 1 scattering event (although, as we saw in the presentation of Feynman diagrams in Chapter 1, that defining of "one" scattering event is complicated issues of semantics). Of the initial 100 photons in the impinging beam, 96 are transmitted into the PMMA material. If the surface was real and had a non-zero roughness value, the incident weight of 100 photons would be entered into a rough surface scattering simulation as seen in Chapter 2 and the results of that simulation would provide the scattered and absorbed photon counts.

The transmitted photon with 96% weight now travels in an assumed straight line. A distance to a dice roll location which will determine whether or not an inclusion is hit is calculated from distance between the material entry point and the next reachable interface (in this case, the PMMA/aluminum interface).

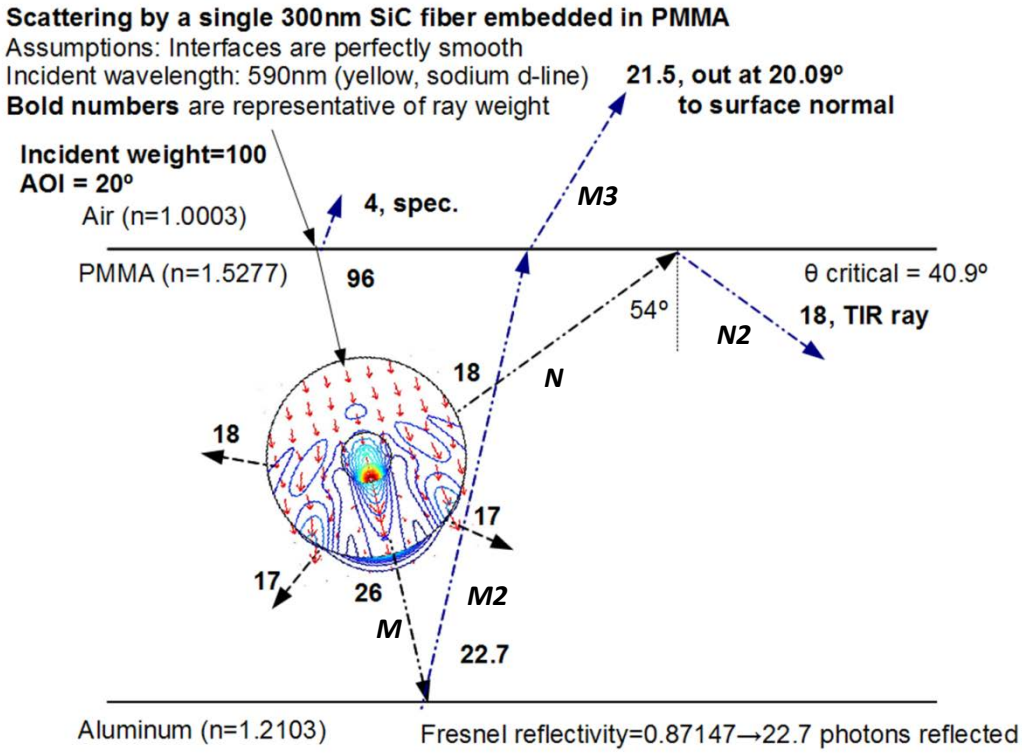

Figure 4-13. Graphical representation of the results from a multiscale scattering simulation involving well-dispersed SiC fibers in a PMMA matrix coated onto aluminum substrate and bounded by air. The air/PMMA interface is ideally smooth, so diffuse surface scattering may be neglected.

Once the uninterrupted internal path length is calculated a step size is chosen for steps between dice rolls. Once the initial step length is chosen the number of steps or dice rolls along the uninterrupted path is determined by taking the uninterrupted path length and dividing by the step size. The photon or photon pack being tracked is then advanced positionally within the material until it arrives at the first chosen dice roll location.

A random number generator is then used to determine whether the photon or photon packet strikes a scatterer. If an inclusion of interest (say, TiO_2 ellipsoids) is loaded into the coating at 40 percent volume, and if the random number generator produces a number (between 0 and 1) that is equal to or less than 0.4, an inclusion is present at the current site in the material and the scattering results are pulled from an earlier or ad hoc finite element calculation of electromagnetic radiation scattering for that particular scatterer in that particular medium. In this case the first *n* steps produce no inclusions, while step *n* does produce an inclusion strike event, which calls the finite element results for that particular SiC inclusion. Figure 4-13 shows a representation of that event in a rough schematic of the ray tracing event, where a photon packet with weight 96% is impinging on the SiC inclusion after being transmitted through the PMMA / air interface.

Quadrature is performed around the circumference or closed sphere (in three dimension cases) of the finite element scattering simulation space in order to determine the number, weight, and direction of outgoing rays from the inclusion scattering event. In this case, (26/96) % weight photons exit the inclusion in a straight path and continue on the original uninterrupted path trajectory; two photon packets with (17/96) % weight each leave forward-facing but at angles, and two (18/96) % weight photon packets leave backwards-facing but at an offset angle to the original incident ray. For each of these five scattered photon packets the unobstructed path length is determined by the above formula and the next dice roll step is determined and applied to the tracked photons in the photon queue. These new photons are then added into the queue and the script continues to solve for trajectory, dice roll, and scattering event results.

For brevity in this demonstration only two scattered rays, *M* and *N* are followed. Ray *M* having weight (26/96) % travels uninterrupted until it reaches the aluminum/PMMA interface, which in this example is assumed to be perfectly flat. Here the scattering event is solved for at the PMMA/interface using Snell's and Fresnel reflectance equations to deduce that (22.7/26) % of the

ray is reflected specularly towards the topmost PMMA/aluminum interface, while the remainder is absorbed into the aluminum metal substrate.

The (22.7/26) % ray *M2* leaves the aluminum interface on a trajectory towards the PMMA/air interface, and after hitting no inclusions during its travel exits the system as photon packet *M3* which travels towards a detector. The outgoing strength is 21.5% of the incident radiation due to some slight attenuation during travel, and the outgoing angle is 20.09 degrees to the global surface normal. Recalling that the incident angle is 20 degrees, this outgoing photon packet could be summed into a specular reflection bin depending on the relative size and placement of any detectors, even though the photon packet was transmitted through the material and the photon packet impinged on or through a nanoscale scatterer in the material. Note also that in this very simplified model a total of 21.5 + 4 photons out of 100 could potentially be collected at the specular gloss detector, resulting in a gloss reading well above 100% specular gloss.

The side scattered photon packet *N* travels towards the PMMA/air interface without reaching the aluminum substrate, that is the scattering event reversed the photon's trajectory back towards the topmost surface. Here, however, the photon packet grazes the underside of the PMMA/air interface at an angle (54 degrees) greater than the critical angle for total internal reflection (40.9 degrees). The entire bulk of scattered photons from *N* is internally reflected as ray *N2*, which is now directed towards the aluminum/PMMA interface as the photon packet leaves the frame of reference for this example. The photon continues to be tracked in the actual simulation.

This model formalism can be used to study or investigate the scatter processes or phenomena by nanoscale inclusions that are generally considered to be invisible or clear. In reality, they are invisible to the human eye, but not to instrumental detectors. However, these scattering events are definitely "invisible" to closed form ray tracing where photons wouldn't effectively "see"

the inclusions because their scattering cross sections are smaller than the geometric limit of the radiation system of interest.

4.8. Results: a multiple fiber case study

Figure 4-14 is nearly identical to the material geometry presented in Figure 4-13 above, but with multiple inclusions and local coarseness present, where the inclusions are clustered closely and not properly dispersed, but only in local regions. Here, three 300 nanometer diameter SiC fibers are embedded horizontally to each other in a PMMA slab over an aluminum substrate. This is a cluster or brush arrangement of SiC nanofibers, and may be present in composites that are designed to have directional anisotropic mechanical properties.

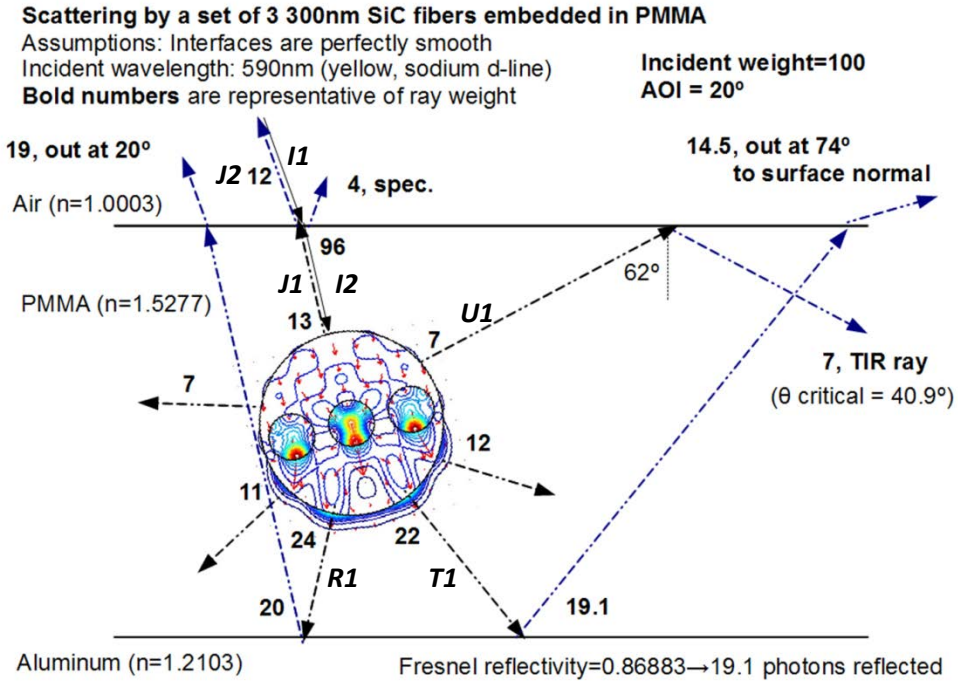

Figure 4-14. Graphical representation of the results from a multiscale scattering simulation involving well-dispersed SiC fibers in a PMMA matrix coated onto aluminum substrate and bounded by air. The air/PMMA interface is ideally smooth, so diffuse surface scattering may be neglected.

The incident ray launched into the system at *I1* has a relative weight of 100. This ray enters the PMMA slab as before, with 4 percent of *I1* photons specularly reflected off the surface after one scattering event, and 96 photons of *I1* entering or being transmitted into the PMMA slab as *I2*. Photon packet *I2* continues on a trajectory until it reaches the scattering region occupied by the cluster of SiC brushes. Here, as before, the geometric optics model shifts to the finite element simulation approach and solves the Maxwell equations for wave propagation for this system of 3 SiC fibers. This is a much more interesting, complex, and crowded scattering event than before in the case of a solitary fiber, and there is significant retroreflectance (12 percent of initial photon weight travelling as *I3*) in the direction of the original photon source that isn't present in the single fiber case. In the straight ray- tracing approach to light scattering simulation and prediction, this cluster of SiC fiber nanoinclusions would still be "invisible" to the incident photons, and no retroreflectance would be predicted. Indeed, many closed-form solutions would predict no scattering at all by the cluster of nanoscale fibers.

This is a more complicated arrangement of inclusions and scattering behavior, and is also easily accommodated by the hybrid formalism presented here. Interesting and unexpected results are obtained, even at the case study level, which may at first seem counterintuitive. Also, the finite element solution here is still a "single" scattering event, but the results are amplified when the volume or number of inclusions is increased.

Scattering from the finite element region in the polymer that contains 3 SiC nanofibers produces seven rays during peak-biased quadrature that will be added to the growing photon queue. In this example, rays or photon packets *J1*, *U1*, *R1*, and *T1* will be tracked, as the balance of the scattered rays each travel laterally outside of the figure frame of reference (but are continued to be tracked in the actual simulation itself). *J1* with weight (13/100) is retroreflected in the direction of the source, and eventually is collected at a detector positioned exactly where the source was located,

photon *J2* (12/100 photon packet weight). Scattered photon packet *R1* is forward scattered from the cluster of inclusions and scatterers off the aluminum substrate before exiting the slab at the polymer / air interface and heading to a detector that is also positioned close to the incident source. The other strongly forward scattered photon packet *T1* also reflects off the aluminum substrate before travelling to the PMMA/ air interface and exiting the system at an angle close to grazing (74 degrees relative to the surface normal). Finally, the slightly backscattered photon packet *U1* is internally reflected at the PMMA/air interface after it arrives at an angle greater than the critical angle for total internal reflection.

4.9. Benefits and generality of the hybrid scattering model

There are many benefits to adopting a highly general hybrid scattering approach to electromagnetic radiation transport calculations.

Inputs into the model are simple and can be quickly adjusted. The finite element solutions of the Maxwell equations can be used to treat objects of all sizes, not just those around or beneath the geometric limit in dimension. This approach is computationally expensive, but is becoming increasingly affordable due to the enhanced computing power that is widely available in academia and industry.

The incorporation of finite element methods allows for very complex 2D/3D and even 4D shapes, structures, and systems to be modeled. Coatings and composites often have a temporal, as well as a spatial dimension, meaning their material appearance is often a function of time, due to natural weathering, aging, in-service wear, or other modes of exposures. The multiscale approach here may be modified for such "4D" applications, where the temporal inclusion changes are modeled separately, and the proper time-dependent scattering result is used during the total multiscale simulation. An example of a 4D scatterer or inclusion would be an air void or a

heterogeneous phase enlarging over time due to Ostwald ripening, or might be a fiber debonding from the surrounding polymer matrix with accumulated wear and damage over time.

The statistical dice roll used in the model allows for coarseness to occur naturally, and is more realistic than discretely entering a coarse inclusion pattern into the model. While discrete models are very useful in certain applications, they are often difficult or impossible to empirically reproduce in a real material. Thus, the statistical approach to both simulation and real material production is often the wiser approach to take when experiments and models have to validate and evolve through iterative improvements in a coupled experimentation-simulation feedback loop.

4.10. Adding color to radiation transport simulations: mathematical conversion to color coordinates

Oftentimes, light scattering simulations are only useful if they can ultimately provide visual results. Fortunately, this is readily accomplished by parameterizing the simulations across the visible spectrum, and summing those results into values for tristimulus values, CIE L*a*b*, or RGB. Literature in computational color science, such as the book by Westland and Ripamonti[4] and the classic text by Billmeyer and Saltzman, now maintained by Berns[5], offer many numerical methods for summing and translating between different color spaces.

More so than electromagnetic signature, the coatings scientist is often interested in what color a certain formulation will have in its cured, in-service state. This can be accomplished a number of ways, as summarized in Figure 4-15.

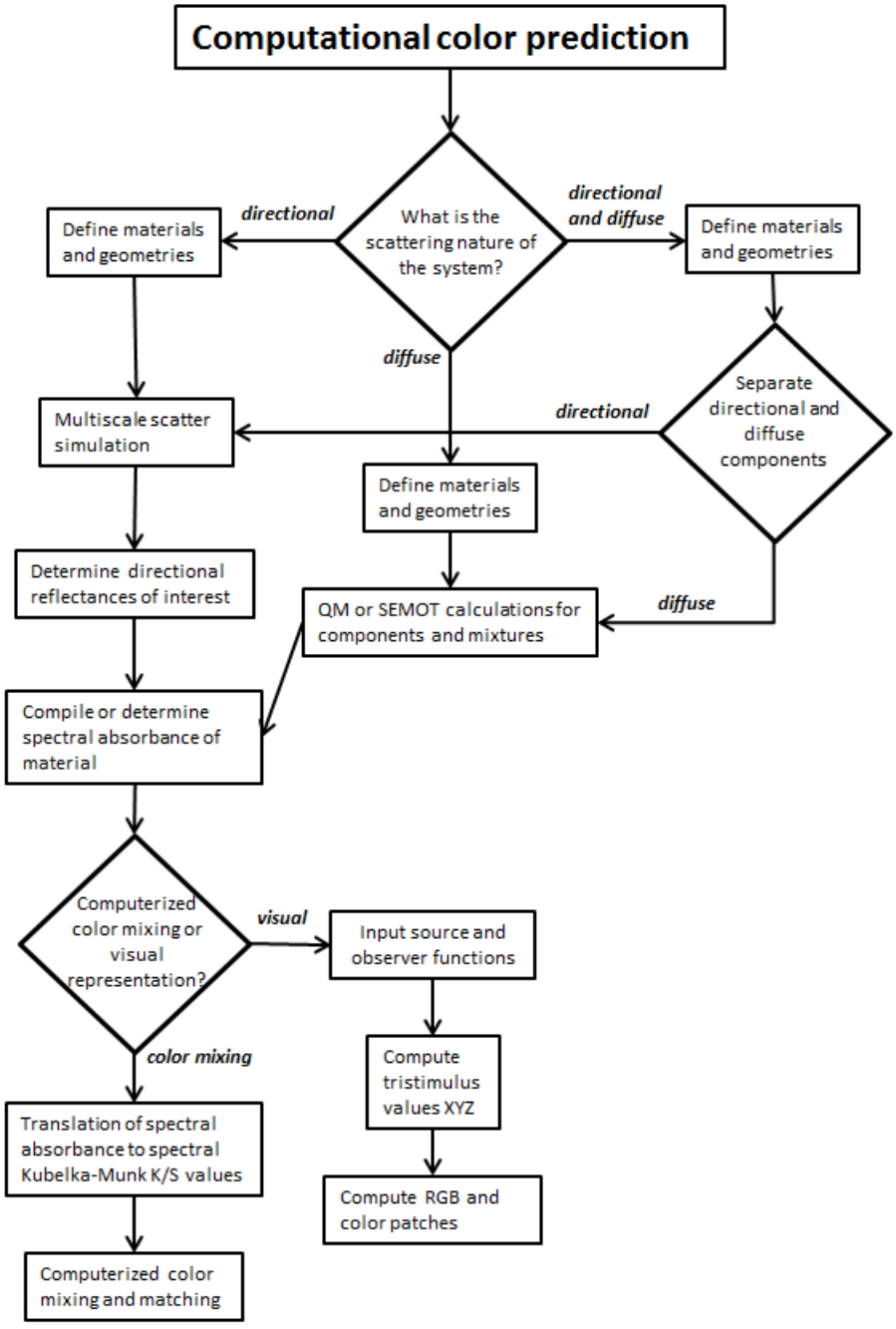

Figure 4-15. Diagram of options for color treatment in multiscale simulations containing directional, diffuse, or combined components.

4.10.1. Color prediction of purely directional scattering systems

Purely directional scattering systems are those where diffuse scatterers are not present in the bulk, i.e. all scattering events occur at the continuum length scale. Examples of such systems are nanoparticles in coatings, organic coatings containing titanium dioxide, coatings containing special effects pigments, and composites containing fibers and other continuum scale inclusions. In this case, the multiscale geometric optics and finite element scattering simulation is performed for the given system. The incident radiation is parameterized over multiple wavelengths in order to produce predictions of directional spectral reflectance, collected from photons that leave the system at variously placed directional detectors outside of the simulation space. These results are converted and compiled into spectral absorbance values for the material of interest, which are in turn converted to Kubelka-Munk theory K/S values for color mixing applications, or are converted to tristimulus values after a light source and set of standard observer functions is input by the user. The former approach can be used to select pigments and concentrations that will produce the desired color response, while the latter approach is used to view visual representations of color predictions on a computer monitor or printed report.

4.10.2. Color prediction of purely diffuse scattering systems

In the case of purely diffuse scattering systems, such as dyed coatings and composites, quantum mechanical or semi-empirical molecular orbital theory calculations are used to compute the spectral absorbance of the material individual material components, or of small clusters of components if dispersion if heterogeneous.

The semi-empirical molecular orbital theory package VAMP uses the same linear combination of atomic orbitals-self consistent field (LCAO-SCF) theory that more computationally expensive *ab initio* programs use. However, some of the complex and more computer intensive

integrals are removed and replaced using either simple approximations or empirical relationships or parameters where appropriate. The following example of implementation uses the NDDO Hamiltonian approximation set with AM1 parameterized elements. This approach is relatively appropriate for molecules containing on carbon, hydrogen, oxygen, and nitrogen. Modified approximation sets and parameterized elements should be used with other molecular systems, or a more dedicated computational approach should be undertaken to accommodate *ab initio* calculation.

For quinacridone violet in poly(methyl methacrylate), PMMA, the spectral absorbance of each of the components is calculated in VAMP, along with a mixed cell containing both components for comparison, shown in Figure 4-16.

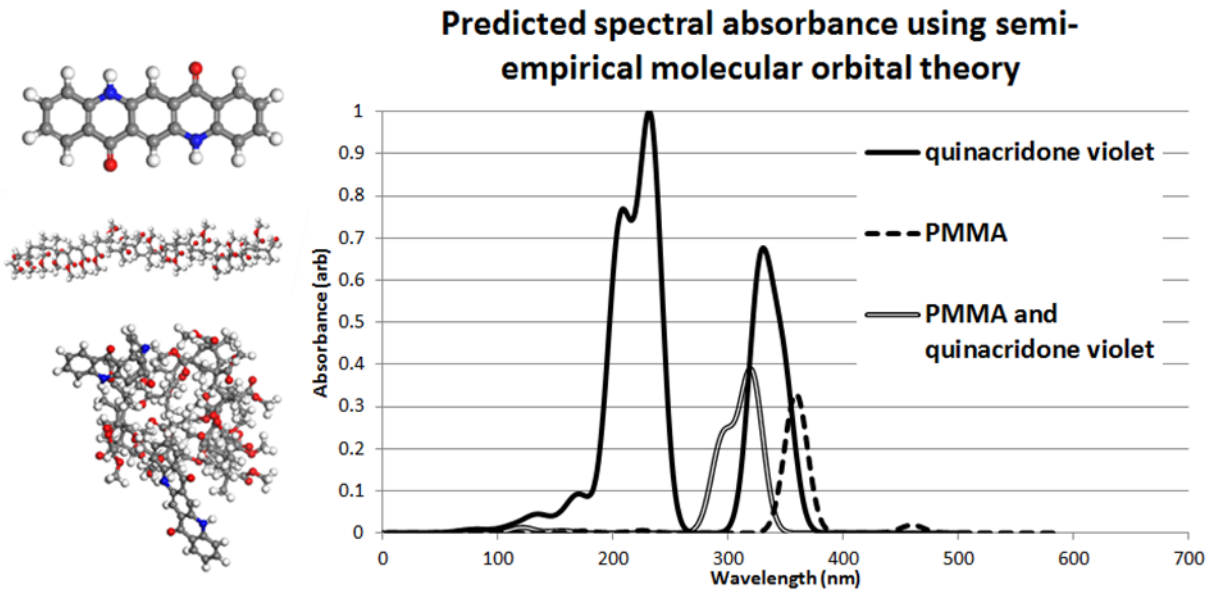

Figure 4-16. Semi-empirical molecular orbital theory predicts the optimized geometry of various components in a colored system, as well as the spectral absorbance spectra.

For a statistical material prediction, the weighted absorbance spectrum for the complete material may be computed from the individual component weights and their respective absorbance spectra. For discrete material predictions, a finite element approach to averaging may be used, where

a grid of material is defined, wherein each grid element may have a different concentration of dye or other chromophore, and the local grid properties are summed into the gross length scale absorbance values, as seen in Figure 4-17.

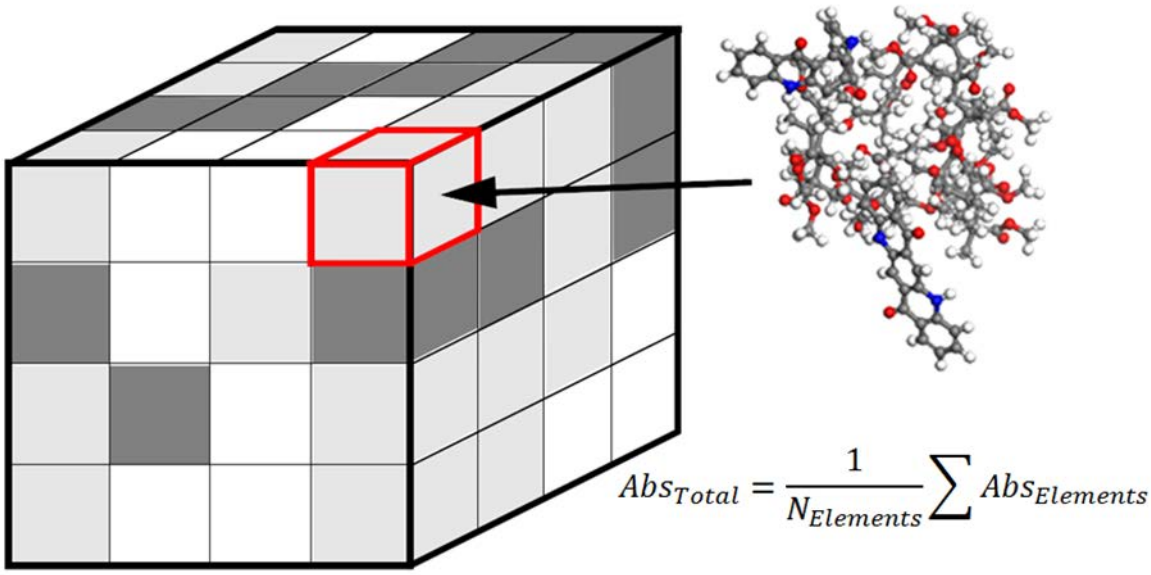

Figure 4-17. In systems with heterogeneous distribution of chromophores, a finite element approach to averaging may be used, whereby molecular modeling computes the individual absorbance of separate grid elements, and the bulk property exhibits summed absorbance of its components.

If the total material has significant absorbance in the visible wavelength range, the color prediction codes presented elsewhere in this dissertation may be used to compute XYZ, RGB, and visual appearance color patches for qualitative and aesthetic assessment.

If the resultant total material absorbance is desired for color mixing and matching applications, the predicted absorbance response may be converted to Kubelka-Munk K/S values, using the formalism presented below.

It should be noted that many pigments and dyes contain and indeed rely on inorganic components to impart their chromophoric behavior. For many such systems the ab initio and semi-empirical methods readily available may not suffice, and it may be user to find values for spectral

reflectance to be used as starting points in the open color science literature, such as the technical report by Mohammadi et al.[6].

4.10.3. Kubelka-Munk theory and application to multiscale light scattering simulations

The Kubelka-Munk set of color mixing theories [5, 7-14] are useful in situations where the material being modeled scatters as well as absorbs light, and where only general flux information is desired. Although light in a scattering as well as absorbing material undergoes complex-subtractive mixing, the employment of Kubelka-Munk theory greatly simplifies matters. In this case, it is assumed that all light will be designated as either travelling up or down in a direction perpendicular to the plane of the sample. In other words, there is an "in-flux" and an "out flux," and the most common form of the Kubelka-Munk theory is generally referred to as a "two-flux" theory. A second important assumption in the theory is that the colorant layer must be completely diffuse, so that no directional information is incorporated into the model. Because of this, metallic, pearlescent, and many other directional special effects pigment types cannot be considered with Kubelka-Munk theory. Another negative aspect of the approach is that the set of parameters used apply to only one wavelength at a time, so a spectrophotometer must be used to generate data, and care must be taken in deciding what wavelengths to perform the math on.

For opaque systems like heavily pigmented or dyed coatings, a Kubelka-Munk value of K/S ("K over S," is determined from the reflectance at a given wavelength, and represents the ratio of absorption (K) to scattering (S).

$$\left(\frac{K}{S}\right)_{\lambda} = \frac{(1-R_{\lambda,i})^2}{2R_{\lambda,i}} \qquad \text{Equation 4-1}$$

The K/S ratio of a mixture of components in a single material is simply an additive combination of each colorant component's unit absorptivity, k_λ, and unit scattering, s_λ, scaled by the effective concentration and added to the absorption and scattering of the substrate, noted with subscript *t*, as in Equation 4-2.

$$\left(\frac{K}{S}\right)_{\lambda,mix} = \frac{K_{\lambda,mix}}{S_{\lambda,mix}} = \frac{k_{\lambda,t}+c_1k_{\lambda,1}+c_2k_{\lambda,2}+\cdots}{s_{\lambda,t}+c_1s_{\lambda,1}+c_2s_{\lambda,2}+\cdots} \qquad \text{Equation 4-2}$$

If one assumes no scattering and only absorption, the mixing equation is simplified and only the component K/S value needs to be known and Equation 4-3 may be used.

$$\left(\frac{K}{S}\right)_{\lambda,mix} = \left(\frac{k}{s}\right)_{\lambda,t} + c_1\left(\frac{k}{s}\right)_{\lambda,1} + c_2\left(\frac{k}{s}\right)_{\lambda,2} + \cdots \qquad \text{Equation 4-3}$$

Surface roughness and refractive index changes at the surface or surfaces are included through the Saunderson correction, Equation 4-4 [15], where K_1 and K_2 are the Fresnel reflection coefficients for light incident on the material from the outside and striking the surface from the inside, respectively.

$$R_{\lambda,i} = \frac{R_{\lambda,m}-K_1}{1-K_1-K_2+K_2R_{\lambda,m}} \qquad \text{Equation 4-4}$$

For measurements taken with a specular excluded geometry, the K_1 value is removed from the numerator[5]. The Kubelka-Munk (K/S) value is roughly linear with respect to colorant concentration and can, with slight or no modification, be used when the appearance of a coating

must be related to the type and amount of colorants in them, provided the colorants are typical dyes and pigments[16].

For the quinacridone violet and PMMA system noted above, the material is only weakly absorbing in a narrow absorbance band centered on 320 nanometers wavelength, with a relative unit value of 0.4. Thus, the (K/S) for this system is given by:

$$\left(\frac{K}{S}\right)_{QV/PMMA,320nm} = \frac{(1-(1-0.4))^2}{2(1-0.4)} = 0.133 \qquad \text{Equation 4-5}$$

This simulated material is now ready to be added to a virtual color mixing program as a component or colorant. Due to the discrete nature of the atomistic simulation used to compute the absorbance, care should be taken to adjust the virtual concentration of dye within the surrounding polymer matrix. An effort should be made to create standard curves using known physical formulations to benchmark the simulations against.

4.10.4. Color prediction of scattering systems with diffuse and directional components

For systems containing both diffuse and directional components, a hybrid approach must be taken. The diffuse components should be separate from the directional components, and their visual and colorimetric properties should be computed separately. The directional components may undergo the usual ray tracing and finite element inclusion scattering approach, and results can be combined to produce the final predicted material response.

A typical example of such an approach would be an organic coating containing an organic dye, such as quinacridone violet, and a pigment such as titanium dioxide. The quinacridone violet in polymer matrix will be computed using the atomistic and Kubelka-Munk approaches, and the rough surface and titanium dioxide pigments will be treated using the ray tracing and finite element

approach used for directional materials. Results can be summed at the material tristimulus value construction, as the tristimulus value and, subsequently, RGB and CIELAB values, are not length scale or directionally-dependent.

An interesting aspect of color visualization is the prediction of metamerism. These methods replicate the effects of color blindness (observer metamerism) and the effect of changing the incident radiation source (source metamerism), or perceived differences between two observers with different observer functions. Using tristimulus values, the predicted spectral response of a material generated by coupled surface and inclusion scattering methods can be combined with known light source spectral power distributions to predict the resultant color of the material seen by a neutral observer. Figure 4-18 shows the predicted source metamerism effects of an epoxy loaded with quinacridone violet dye, illumined under different common light sources C, D65, A, and F2 incandescent bulb. Clearly, the illuminant will render the same surface many colors, ranging from orange to purple. These methods enable the coatings scientist to predict color and appearance, even when a large selection of laboratory light sources is physically unavailable.

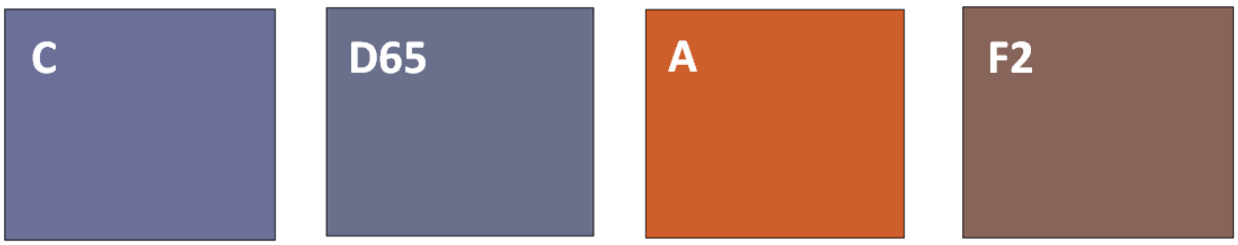

Figure 4-18. Simulating the effects of source metamerism; an epoxy loaded with quinacridone violet illuminated under various lighting conditions.

4.11. Queuing approaches in the modeling of radiation transport

The robustness and scalability of ray tracing simulations is largely dependent on the queuing method used to account for, track, and process the in-system photons until they exit and are collected or otherwise die of extinction within the system.

Because the finite element solutions to the Maxwell equations are readily performed in COMSOL, and because COMSOL integrates readily with MATLAB, a first choice for an overall coding language is the MATLAB .m file. MATLAB is a high-level programming tool that can accommodate Java queuing packages that allow for a variety of last-in-first-out (a LIFO stack), first-in-first-out (a FIFO stack), and a double ended queue structure that is accessible in either LIFO or FIFO mode, called DEQUE (for double-ended queue).

However, a JavaScript approach is not absolutely necessary. A brute force while loop may be used to grow a pseudo-queue as a photon array inside of a loop structure. The pseduocode structure for such an approach takes the following pseduocode form:

```
% initialize photons
photons = ones(100,3);
icount = 1;

while icount <= length(photons)

workingphoton = photon(icount);

% do simulation on workingphoton
newphotons = simulation(workingphoton);

% add new partial photons to list
Photons =  ( photons; newphotons );

% increase counter
icount = icount + 1:

end
```

Other approaches to queue structures in MATLAB are available in the open literature[17], but have not been tested for efficacy or efficiency.

4.12. Advanced topics and proposed improvements to the model

Advanced topics include the treatment of multiple layer coatings and may involve the solving of systems such as scratched basecoats being covered by clearcoats and resultant color changes, or the modeling of geometrically flat yet optically matte clearcoats that might serve as topcoats for rough camouflage basecoats, or a clear topcoat that is covered by a thin layer of polymer waveguide to eliminate specular reflection from the flat surface.

Actual surfaces can be included in the simulation by using various scanning probe microscopy methods and transferring that discrete surface information into a model system. For example, atomic force microscope height maps may be used to simulate a discrete material surface.

These hybrid approaches might also be used to improve inverse formalism and evolve those types of models, for example a surface or material that absorbs only in a narrow spectral band, or a material that scatters the preponderance of incident radiation into a well-defined directional steradian[18]. Metamaterials are easily accommodated for in this model by simply entering a material that has metamaterial optical properties displayed in n and k.

4.13. Conclusions

The surface scattering model from Chapter 2 can simulate appearance, source metamerism, and predict effects of surface roughness on specular components of a material's EM signature.

The 2D and 3D surface scattering models presented in Chapter 3 can predict trends in rough surface scattering behavior given a system with well-defined geometrical surface statistics and component material optical properties.

Thus, a hybrid multiscale model has been developed and presented that relies on ray tracing methods to compute surface scattering and bulk material transport properties. The hybrid model uses finite element solutions to the Maxwell equations for bulk inclusion scattering calculations, where the relative size of the inclusion in comparison to the wavelength is arbitrary. That is, inclusions may be smaller than or larger than the geometric limit dictated by the incident radiation wavelength.

The placement of nanoscale finite element zones in the bulk ray tracing model can be used to study unique, difficult, or intractable systems such as clusters of nanoscale inclusions, pearlescent pigments and color change/flop phenomenon, as well as air voids, debonding of fibers, heterogeneous phase evolution, and other time-dependent, 4D scattering phenomenon.

4.14. References

1. Feynman, R.P., *QED: The Strange Theory of Light and Matter*. Princeton Science Library. 1985, Princeton, New Jersey: Princeton University Press.
2. Sapper, E., S.G. Croll, and B.R. Hinderliter. *Monte Carlo Simulation of Geometric Scattering of Light by Coatings*. in *FutureCoat! 2008*. 2008. Chicago, IL.
3. Sapper, E. and B.R. Hinderliter. *Monte Carlo Method for Electromagnetic Scattering Incorporating Finite Element Methods to Generate Scatter Sources for Nanoscale Inclusions in Composites*. in *TMS 2010*. 2010. Seattle, WA.
4. Westland, S. and C. Ripamonti, *Computaitonal Colour Science using MATLAB*. 2004, West Sussex, England: John Wiley.
5. Berns, R.S., *Billmeyer and Saltzman's Principles of Color Technology*. 3rd ed. 2000, New York, NY: John Wiley.
6. Mohammadi, M., et al., *Pigment selection using Kubelka-Munk turbid media theory and non-negative least square technique*, 2004, Rochester Institute of Technology: art spectral imaging (Art-si.org).
7. Kubelka, P., *New contributions to the optics of intensely light-scattering material, part I*. J. Opt. Soc. Am., 1948. **38**: p. 448.

8. Kubelka, P., *New contributions to the optics of intensely light-scattering material, part II.* J. Opt. Soc. Am., 1954. **44**: p. 330.
9. Kubelka, P. and F. Munk, *Ein beitrag zur optik der farbanstriche.* Z. Tech. Physik., 1931. **12**: p. 330.
10. Latimer, P. and S.J. Noh, *Light propagation in moderately dense particle systems: a reexamination of the Kubelka-Monk theory.* Appl. Opt., 1987. **26**(3): p. 514-523.
11. Molenaar, R., J.J.t. Bosch, and J.R. Zijp, *Determination of Kubelka-Munk scattering and absorption coefficients by diffuse illumination.* Appl. Opt., 1999. **38**(10): p. 2068-2077.
12. Murphy, A.B., *Modified Kubelka-Munk model for calculation of the reflectance of coatins with optically-rough surfaces.* J. Phys. D: Appl. Phys., 2006. **39**(2006): p. 3571-3581.
13. Phillips, D.G. and F.W. Billmeyer, *Predicting Reflectance and Color of Paint Films by Kubelka-Munk Analysis.* J. Coat. Technol., 1976. **48**(616): p. 30-36.
14. Vargas, W.E. and G.A. Niklasson, *Applicability conditions of the Kubelka-Munk theory.* Appl. Opt., 1997. **36**(22): p. 5580-5586.
15. Saunderson, J.L., *Calculation of the Color of Pigmented Plastics.* J. Opt. Soc. Am., 1942. **32**: p. 727-736.
16. *The Kubelka-Monk theory and K/S*, in *Insight on Color*2008: HunterLab.
17. Various. *MATLAB Central File Exchange.* 2012; Available from: www.mathworks.com/matlabcentral/fileexchange.
18. Maradudin, A., ed. *Light Scattering and Nanoscale Surface Roughness.* Nanostructure Science and Technology. 2007, Springer.

CHAPTER 5. COMMERCIAL AND RESEARCH APPLICATIONS OF LIGHT SCATTERING SIMULATIONS

5.1. Introduction

There are many conceivable platforms for the multiscale method of electromagnetic signature presented here, ranging from coatings and composites to biological systems, as well as more industrial applications such as aerospace, defense, and the development of novel non-destructive evaluation methods.

Each of the above will be addressed here, with a heavy-handed and lengthy emphasis on coatings applications.

5.2. Coatings applications: a program for color and appearance changes with roughness

Electromagnetic radiation transport in coatings is responsible for color and gloss perception, as well as the photodegradation and weathering of a coating. Radiation transport is in many cases a geometrical process, so surface roughness (even on the nanoscale) can have large effects on a coatings appearance and remaining service lifetime. A user-friendly program has been developed, that simulates the color change of a given surface with nanoscale surface roughening, capable of providing as outputs a spectral power distribution with roughening, as well as RGB, XYZ, ΔE, whiteness index, yellowness index, and tint index when reflectance versus wavelength, initial roughness, roughening rate, light source, and standard observer choice are entered as inputs. The degree of surface roughening is limited to 1270 nanometers as a maximum value, as indicated by the Bennett and Porteus equations for reflectance and roughness[1, 2]. The program has been used to

simulate the color change with increasing surface roughness for a variety of colored amine-crosslinked epoxy pucks.

5.2.1. Introduction and theory

Electromagnetic radiation transport is important in many aspects of coatings technology. How radiation interacts with a coating (and indeed, any material) determines how the coating will appear visually, as well as how the coating will weather or photodegrade. Appearance and weatherability are of primary importance in coating formulation and design. Previous work has focused on electromagnetic radiation and photodegradation relationships in polymeric materials, with some emphasis on nanoscale surface roughening and gloss. Until now, the visual appearance of colored samples with imposed weathering (i.e. surface roughness) has not been studied. The program presented here is a first attempt to do just that.

Bierwagen has used Kubelka-Munk theory to simulate the change in coating optical properties with film thickness nonuniformities of up to 0.5 mils (12.7 microns, or 12,700 nanometers)[3], although no research has been presented on color changes due to nanoscale surface roughness. Bennett and Porteus reported a correlation between gloss (specular reflectance) and surface roughnesses less than 50 microinches (1270 nanometers)[1]. The Bennett and Porteus model is a robust equation that has been modified into a statistical model for predicting reflectance changes with surface roughness by Croll and Hinderliter [4-8]. Croll and Hinderliter incorporate the Central Limit Theorem into the Bennett and Porteus model, allowing for predictions of surface roughness caused by a large number of random and repeated events, such as the striking of ultraviolet photons on a coating surface during photodegradation and weathering processes. This statistical model assumes that random, repeated assaults of ultraviolet, damage-inducing photons will produce a surface topography that becomes random after many repeated events. If one assumes that the

random topography consists of heights that are normally distributed in a Gaussian fashion[8], then the standard deviation of the surface height distribution may be represented as being proportional to the square root of the number of events contributing to the accumulating surface damage.

For a material that is being degraded, $\boldsymbol{N}$ is defined as the average number of fragments removed at a certain physical location on the surface and is equal to the product of the photon flux, the absorption probability, the quantum efficiency of removing a length of polymer, and elapsed time. For a given material the first three terms simplify to a constant $\boldsymbol{K}$, defined as the flux of photons multiplied by the absorption probability multiplied by the quantum efficiency multiplied by time. Now, $\boldsymbol{N}$ may be simplified as being equivalent to $\boldsymbol{K} * t$.

The above approach assumes that degradation is simple and linear (zero-order kinetics). Thus, trends in color change with increasing roughness will appear linear. Under these assumptions the overall degradation (including mass loss or thickness decrease) will be a linear function with time. The simplified expression for $\boldsymbol{N}$ may be correlated to a more common descriptor of surface roughness, **σ**, which is the root mean square (rms) of the surface height distribution. For polymeric coatings, **σ** represents the standard deviation in the average number of polymer segments removed at a location on the coating surface after sufficient exposure has occurred to randomize the surface. If we define **ε** as a characteristic fragment size or length removed at each time step **Δt**, then overall roughness may be represented as follows:

$$Roughness = \sigma_{rms} = \varepsilon\sqrt{N} = \varepsilon\sqrt{Kt} = \sqrt{kt} \qquad \text{Equation 5-1}$$

Therefore, roughness increases as exposure continues with the square root of exposure time due to the random arrival of ultraviolet photons and the statistics of the material response. The variable $\boldsymbol{k}$ introduced above will be referred to as the *degradation rate* parameter. This parameter

includes the effect of absorption, bond scission chemistry, size of erosion event (related to the fragment length and the extent to which damage is smoothed out by molecular relaxation properties), and radiation intensity. Thus, the value of $\boldsymbol{k}$ is environment- as well as material-dependent.

The degradation rate may be used in a physical model that correlates surface roughness and surface roughness changes to changes in the objects reflectance. The model uses as a starting point the familiar Bennett and Porteus model for the specular reflectance (gloss) of a rough surface:

$$\frac{R_s}{R_0} = exp\left[-\left(\frac{4\pi \cos\theta\sigma}{\lambda}\right)^2\right] \qquad \text{Equation 5-2}$$

In Equation 5-2, $\boldsymbol{R_s}$ is the specular reflection of the rough surface, $\boldsymbol{R_0}$ is the reflection of a perfectly smooth surface of the same material, $\boldsymbol{\sigma}$ is the root mean square deviation of the surface from its mean, assuming a Gaussian distribution, and assuming that its value is smaller than the wavelength of incident light, $\boldsymbol{\theta}$ is the specular angle, and $\boldsymbol{\lambda}$ is the wavelength of illumination (however, most reflectance measurements use a standard illumination spectrum, not a single wavelength).

The boundary condition of having no rms roughness greater than the wavelength of incident light effectively means that the Bennett and Porteus equations do not hold for rms surface roughnesses greater than 1270 nanometers[1]. The rms roughness of the surface at any time $\boldsymbol{t}$ will be a combined effect of its initial value, $\boldsymbol{\sigma_{initial}}$, due to application procedures and composition, and the subsequent increase due to weathering, represented by $\boldsymbol{kt}$ in Equation 5-3:

$$R_s(t) = R_0 exp\left[-\left(\frac{4\pi \cos\theta}{\lambda}\right)^2 ({\sigma_{initial}}^2 + kt)\right] \qquad \text{Equation 5-3}$$

Equation 5-3 will be used in code to predict the change in reflectance (and thus perceivable color) for samples that are being roughened on the nanometer length scale with any arbitrary time step t. It is important to note this last part and its implications on k. The degradation parameter will include any and all non-linear responses to roughening, while only changing t will give a strictly linear response. That is to say, an accurate k parameter is heavily dependent on strong experimental weathering data and contains the bulk of the material weathering performance properties, while t may be thought of as a series of calculations performed by the program that does not contain any material parameters.

Tristimulus values (XYZ) are the fundamental coordinates of color measurement. Once tristimulus values are calculated, conversion to other color spaces (RGB, L*a*b*, etc) is a matter of simple matrix transformation. The tristimulus values are defined as follows in Equations 5-4, 5-4, and 5-6, given by ASTM E-308[9]:

$$X = k\sum_{\lambda} R(\lambda)S(\lambda)\bar{x}(\lambda)\Delta\lambda \qquad \text{Equation 5-4}$$

$$Y = k\sum_{\lambda} R(\lambda)S(\lambda)\bar{y}(\lambda)\Delta\lambda \qquad \text{Equation 5-5}$$

$$Z = k\sum_{\lambda} R(\lambda)S(\lambda)\bar{z}(\lambda)\Delta\lambda \qquad \text{Equation 5-6}$$

In Equations 5-4, 5-5, and 5-6, k is defined by Equation 5-7:

$$k = 100/\sum_{\lambda} S(\lambda)\bar{y}\,(\lambda)\Delta\lambda \qquad \text{Equation 5-7}$$

Furthermore, in Equations 5-4, 5-5, and 5-6, $R(\lambda)$ is the sample reflectance factor, $S(\lambda)$ is the source spectral power distribution, $\bar{x}, \bar{y}, \bar{z}$ are the standard observer functions for either the 1931 or 1964 standard observer, and $\Delta\lambda$ is the step size in nanometers.

An example of the easy transformation from XYZ to another color space is the XYZ→RGB matrix transformation, performed as follows[10]:

$$\begin{bmatrix} R \\ G \\ B \end{bmatrix} = \begin{bmatrix} 2.3707 & -0.9001 & -0.4706 \\ -0.5139 & 1.4253 & 0.0866 \\ 0.0053 & -0.0147 & 1.0094 \end{bmatrix} \begin{bmatrix} X \\ Y \\ Z \end{bmatrix} \quad \text{Equation 5-8}$$

The transformation from XYZ→CIE L*a*b* is performed not with a matrix transformation, but by using the following equations[10]:

$$L^* = 116(Y/Y_n)^{1/3} - 16 \quad \text{Equation 5-9}$$

$$a^* = 500[(X/X_n)^{1/3} - (Y/Y_n)^{1/3}] \quad \text{Equation 5-10}$$

$$b^* = 200[(Y/Y_n)^{1/3} - (Z/Z_n)^{1/3}] \quad \text{Equation 5-11}$$

In the above equations, X_n, Y_n, and Z_n, are tristimulus values for a reference white. The above XYZ→L*a*b* equations hold true only for colors where X/X_n, Y/Y_n, and Z/Z_n are greater than 0.008856 (only for very dark colors does this not hold true). CIELAB space is more intuitive to use than tristimulus values and has the advantage of residing in a 3-dimensional, Euclidean space, where each axis represents a pair of opponent colors. The L* axis runs from black to white, the a* axis runs from green (negative) to red (positive), and the b* axis runs from blue (negative) to yellow (positive). For this program, the most apposite use of L*a*b* is in computing color differences. The standard CIELAB color difference is ΔE and is simply the Cartesian distance between two points in 3-D space:

$$\Delta E = \sqrt{(\Delta L^*)^2 + (\Delta a^*)^2 + (\Delta b^*)^2} \quad \text{Equation 5-12}$$

Generally speaking, a value of ΔE less than 1.0 represents an acceptable color match (no perceivable difference). The program presented here uses ΔE not to assess color matching, but to quantify color changes with roughening and to rank those changes across many different colors.

The final set of computations in the program involves calculating the whiteness index (WI), the yellowness index (YI), and the tint index (TI), as defined by ASTM E-313[9]:

$$WI = Y + (WI,x)(x_n - x) + (WI,y)(y_n - y) \quad \text{Equation 5-13}$$

$$YI = 100\frac{(C_x X - C_z Z)}{Y} \quad \text{Equation 5-14}$$

$$TI = T,x(x_n - x) - T,y(y_n - y) \quad \text{Equation 5-15}$$

In Equation 5-13, 5-14, and 5-15, WI is the whiteness index, X,Y, and Z are the tristimulus values, WI,x and WI,y are the numerical coefficients defined in ASTM E-313, x and y are chromaticity coordinates, x_n and y_n are chromaticity coordinates of the CIE standard illuminant/source, YI is the yellowness index, C_x and C_z are the correction factors defined in ASTM E-313, TI is the tint index, and T,x and T,y are the tint index numerical coefficients defined in ASTM E-313.

The use of whiteness index equations should generally be restricted to samples that are commercially labeled as "white," and should not be used to quantify the whiteness of a colored or high chroma sample. Similarly, care should be taken when reporting yellowness index values, as YI for samples that are not white or whitish may be meaningless.

5.2.2. The nanoscale surface roughness color change program

All of the equations and operations mentioned above may easily be incorporated into a single mathematical program with only a little background in matrix-vector mathematical notation. A computer code for predicting color change with nanoscale surface roughness has been written in MATLAB (technically a MATLAB "script" or .m file) for simulating the perceived color difference of a surface with nanoscale surface roughening. This codes uses the mathematics presented in the

previous section of this chapter. The user-friendly program asks the user to define a light source and provide the spectral reflectance of the sample being studied (from 380-780 nm), the sample's initial rms roughness, the degradation rate ***k*** (in the form of nanometers per step), the angle of the detector, and the choice of standard observer. The program then computes, in order, spectral reflectance at each step, XYZ at each step, RGB at each step, L*a*b* at each step, and yellowness, whiteness, and tint indices at each step, and graphically displays the following outputs: ΔE color difference at each step, RGB at each step, yellowness, whiteness, and tint indices at each step, as well as spectral reflectance before roughening and after ten steps of roughening. The last graphical outputs are computer-generated color patches of the sample before roughening, and after ten steps of roughening, as well as a patch at each step of roughening. The program also has a built-in option that allows for the exporting of any or all of the numerical results into an Excel spreadsheet for later use. The general inputs and outputs of the program are summarized in Table 5-1.

An appealing aspect of the program is that it asks for no material properties input from the user, apart from what is inherently defined or included in the degradation parameter. That is to say, as long as a reliable ***k*** is chosen, the program does not distinguish between samples or surface types; initial reflectance values for paints, printed paper, dyed textiles, or plastic pucks may all be used in the program. To perform qualification studies of the program, various plastic pucks of different colors were produced and their spectral reflectances measured, as outlined in the following pages.

5.2.3. Experimental procedure

EPON resin 828 (distributed by Miller-Stephenson), an epoxy resin based on the oligomeric prepolymer diglycidyl ether of bisphenol A (DGEBA), and Amicure PACM curing agent (Air

Table 5-1. The nanoscale roughness and color change program inputs and outputs in tabulated form.

INPUTS from USER:	Initial reflectance (380-780 nm) Initial rms roughness σ (nm) Degradation rate ***k*** (nm/step) Detector angle (degrees)
INPUTS chosen by USER:	Source (A, F2, D65, C) Standard observer (1931 (2^o) or 1964 (10^o))
NUMERICAL OUTPUTS: **(all for each step *t*)**	Sample reflectance Tristimulus values (XYZ) Chromaticity coordinates (xyz) RGB color space values CIELAB L*a*b* coordinates Color difference ΔE Whiteness index Yellowness index Tint index
GRAPHICAL OUTPUTS:	Reflectance versus wavelength RGB versus roughness WI,YI,TI versus roughness ΔE versus roughness
COLOR PATCH OUTPUTS:	Initial appearance Initial and after ten steps Appearance at each step
OUTPUT TO EXCEL:	All calculated results in tabulated form

Products), the cycloaliphatic diamine bis(para-amino cyclohexyl) methane, were mixed in a stoichiometric ratio, along with pigments and colorants, to make epoxy-amine pucks of various colors. Epoxy resin was weighed into a plastic tripour beaker, to which a pre-weighed amount of titanium dioxide (grade 706) was added under low shear speeds on a Dispensator disperser (Premier Mill Corp.). Once TiO_2 pigment was dispersed, colorants (if desired) were stirred in by hand. Colorants used in this study include quinacridone violet 9401 (Aqua-Chem), permanent medium yellow 888-2040 T (Colortrend), and phthalocyanine green (Hilton-Davis). A stoichiometric amount of amine curing agent was then added, stirred by hand, and the mixed coating was allowed to sweat for 30 minutes before being poured into cylindrical molds 30 mm in diameter and 25 mm deep (Struers) that were lined with strips of Tedlar release film (DuPont). The epoxy-amine was allowed to cure in the molds at room temperature for 30 additional minutes before being cured in an oven for 48 hours at 45 degrees Celsius. Figure 5-1 shows an empty mold, a mold containing cured epoxy-amine formulation, and the finished plastic puck.

Figure 5-1. The amine-cured epoxy puck molding process: (left) the empty mold, (center) the mold with wet coating, (right) the final puck sample.

Once the cured pucks were removed from the molds they were sanded and polished with a Struers TegraPol-25 polisher with a Tegra-Force 5 attachment. Reflectance measurements were recorded on a Varian Cary 5000 UV-Vis-NIR spectrophotometer equipped with a DRA (Diffuse Reflectance Accessory) attachment. Other color measurements were performed with a datacolor™ SpectraFlash 200 color eye spectrophotometer. Calculations were performed in MATLAB (Matrix

Laboratory, The MathWorks, version 2007a), using the in-house written program for calculating the perceived color difference with nanoscale surface roughening.

5.2.4. Qualification studies of the nanoscale roughness and color change program

The spectral reflectance and L*a*b* coordinates of colored epoxy pucks were measured. The spectral reflectances were used as inputs in program, and the resultant L*a*b* values were compared to those produced by the SpectraFlash color eye. The program is designed to be used with reflectance data of (and only of) the range 380-780 nm. Many commercially-available color eyes measure only 400-700 nm, so less information is produced compared to what the program can account for. Thus, color eye L*a*b* will always be slightly different than program-computed L*a*b*, as the color change program contains more information in its broader range of wavelengths. This is demonstrated in the qualification test using the turquoise puck.

Figure 5-2 shows the spectral reflectance of the turquoise sample puck as measured by UV-Vis in the range of 380-780 nm. The shaded blue areas of the graph represent regions that the computer program incorporates into its L*a*b* calculation that the SpectraFlash color eye does not; in other words, it represents the information gained by using program in combination with UV-Vis instrumentation, compared to using the SpectraFlash color eye alone. Table 2 shows the L*a*b* color coordinates as measured by the SpectraFlash color eye, as compared to the same coordinates produced by the color change program when the spectral reflectance was used as input.

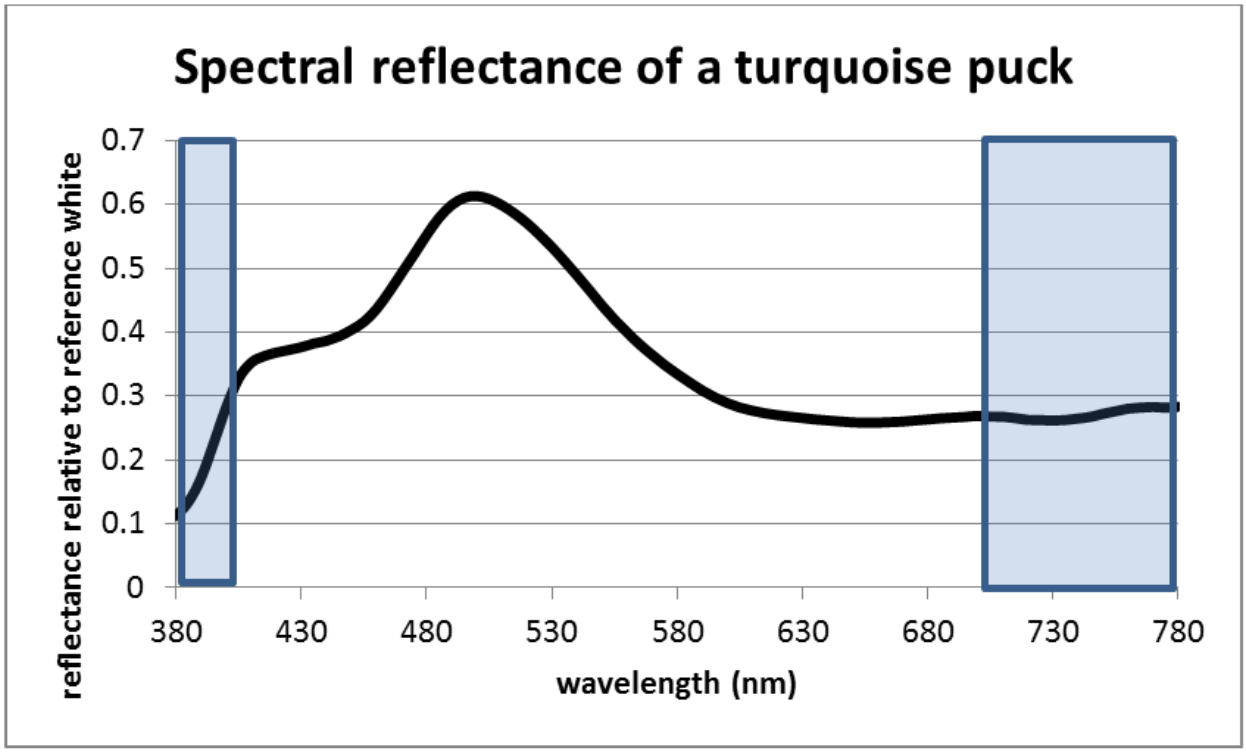

Figure 5-2. The spectral reflectance of a turquoise puck, as measured by UV-Vis spectrophotometry. The shaded blue areas represent the information that is included in the color change program's computed L*a*b*, but not SpectraFlash L*a*b*.

Table 5-2 shows that the L* coordinate is identical for both the SpectraFlash L*a*b* and the program-computed L*a*b*. The program-computed a* is more positive than the SpectraFlash a*, indicating the presence of more red in the sample, clearly from including the 700-780 nm range in the calculation. Likewise, the program-computed b* is more negative than the SpectraFlash b*, indicating an increased presence of blue in the sample, explained by the expanded area in the 380-400 nm range. After these qualification tests, the computer program may be used as intended. The following section presents a complete case study simulation using plastic puck reflectance as initial input.

Table 5-2. A comparison of L*a*b* color coordinates provided by the SpectraFlash color eye and the color change program.

	SpectraFlash 200	std. dev.	Program	[Δ(value)]
L*	71.193	0.0503	71.196	0.003
a*	-25.787	0.0306	-25.075	0.712
b*	0.677	0.0321	-2.081	2.758

5.2.5. Results

The intent of this section is to show the complete set of outputs that a complete simulation with the color change program would provide, as opposed to actual research that may be performed with the program. The sample used in the following simulation is a violet-colored pastel plastic puck. Its reflectance was measured via UV-Vis spectrophotometry and was placed in the sample.xls file in the computer program folder. After the program was initiated in MATLAB, the input listed in Table 5-3 was entered into the program when prompted.

Table 5-3. Arbitrary sample input used in the case study simulation.

Sample:	Violet pastel puck
$\sigma_{initial}$:	0 nm
k:	150 nm/step
Source:	D65
Std.Obs.:	1964 (10 degree)

The choice of sample inputs was chosen randomly, but intentionally covers the entire length scale of the Bennett and Porteus model (150nm/step at ten steps = 1,500 nm roughness, c.f. 1270 nm limit of Bennett and Porteus). Indeed, a ***k*** of 150 nm/step is completely uncorrelated to any physical measurement of time. In the case of real physical weathering of this sample the time per

step may be anywhere from minutes to months, depending on the weathering conditions. As mentioned in the Theory section, it is the ***k*** that will require most experimentation to get right. Also, the choice of a 0 nanometer initial roughness is assuredly an oversimplification. However, the program will output the correct initial color patch and reflectance data even when the initial roughness entered is incorrect.

The first graphical output by the program is a graph of spectral reflectance versus wavelength at different roughnesses, shown in Figure 5-3. Note that at every point in the spectral distribution reflectance is decreased with roughening, but not every decrease is equal in magnitude. For example, the decrease is much more pronounced in the violet region (~415 nm) than it is in the orange region (~600 nm).

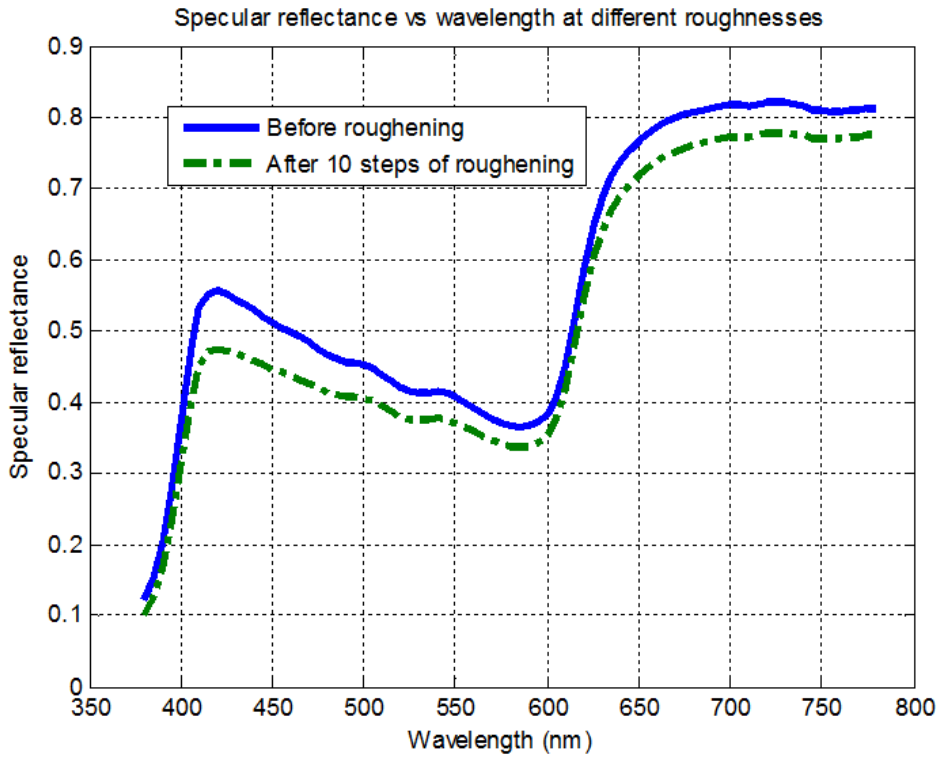

Figure 5-3. Color change program output 1: Specular reflectance vs wavelength at different roughnesses. Note that the magnitude of decrease is not equivalent at each wavelength.

This dynamic change in color with roughening may perhaps be represented more clearly by the second graphical output of the program, RGB as a function of rms roughness, shown in Figure 5-4.

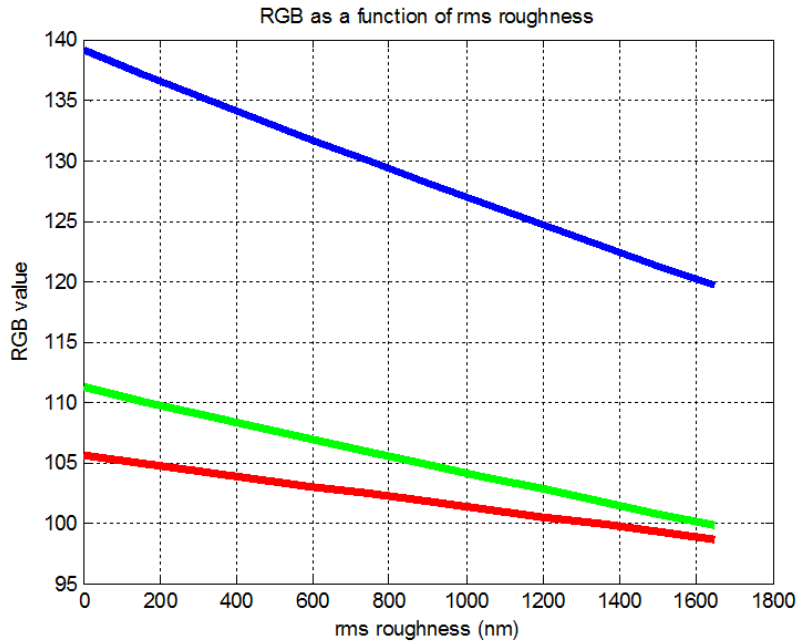

Figure 5-4. Color change program output 2: RGB values as a function of increasing surface roughness. Note how the slope of each line is different.

In Figure 5-4, each RGB value is represented by a color-coded line. While each value is decreasing with increased roughness, the slopes (the rates of change) are different for each value, meaning that the balance between the red, green, and blue channels is constantly changing.

The third graphical output from the color change program is a graph of whiteness, yellowness, and tint indices as a function of rms roughness, shown here in Figure 5-5. The figure clearly indicates that whiteness decreases and yellowness increases as the surface is roughened.

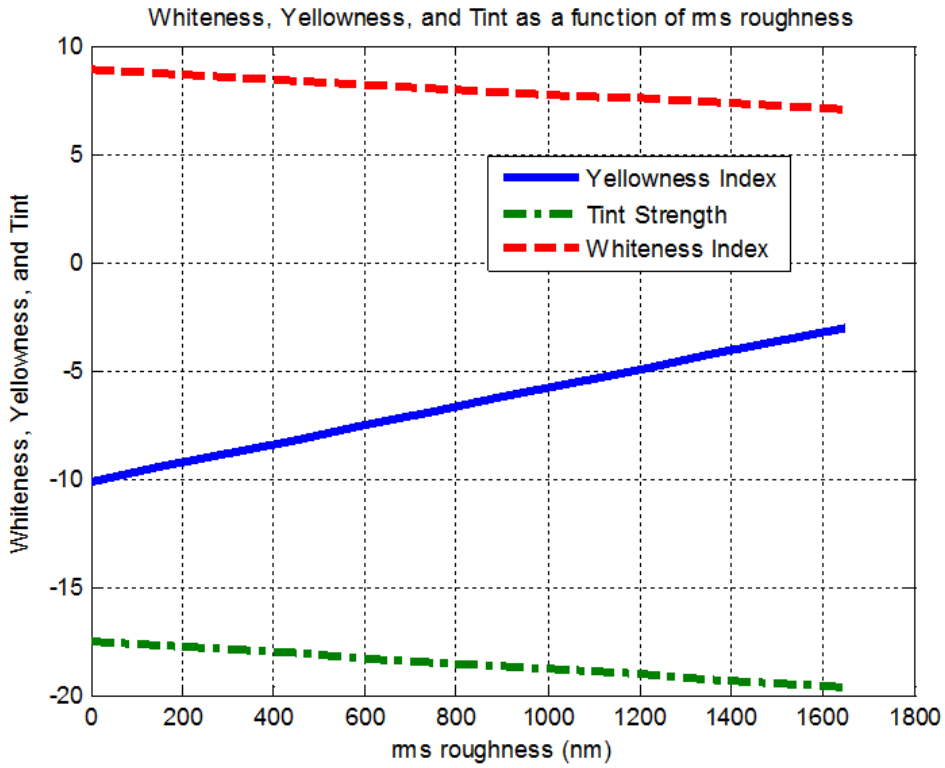

Figure 5-5. Color change program output 3: whiteness, yellowness, and tint indices as a function of surface roughness.

The fourth graphical output of the program is a graph of the color difference ΔE between the current color (with roughness) and the initial color (with $\sigma_{initial}$ roughness; here, $\sigma_{initial}$ is equal to zero), and is provided here as Figure 5-6. When plotted against the surface roughness, the color difference increases linearly, a direct effect of the zero-order kinetics used in the model assumptions. However, if the color difference were plotted against real time, not simulation steps, one would expect the color difference to increase with the square root of time.

The data used to generate the first four graphical outputs is at this point sent to results.xls in the program folder, and the program now generates various color patches to supplement the quantitative color data.

Figure 5-7 shows the first color patch generated by the program, a simple thumbnail of the initial visual appearance of the sample under light source D65 and using standard observer functions from 1964.

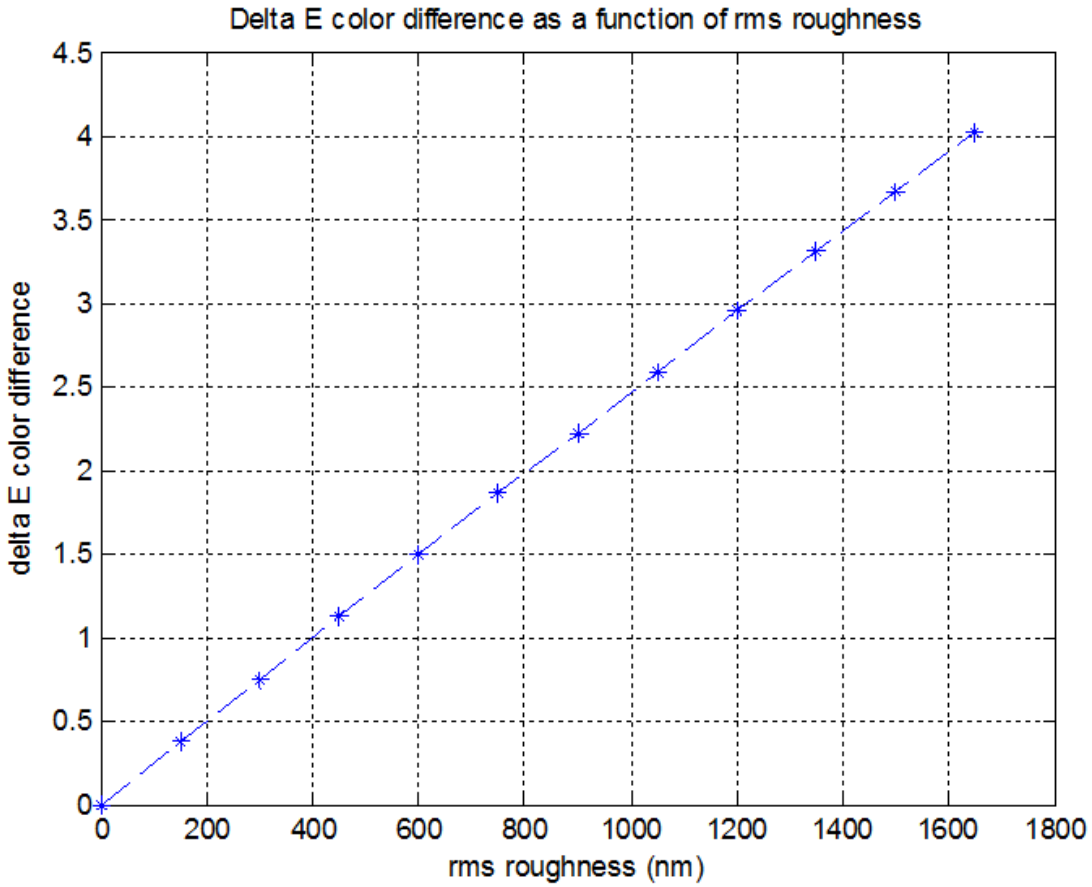

Figure 5-6. Color change program output 4: The ΔE color difference (current versus initial) as a function of rms surface roughness.

Figure 5-8 displays the second color patch output, a series of color patches showing the visual appearance of the object at each step of roughening (initial = 0 nm, 1 step = 150 nm, 2 steps = 300 nm, and so on).

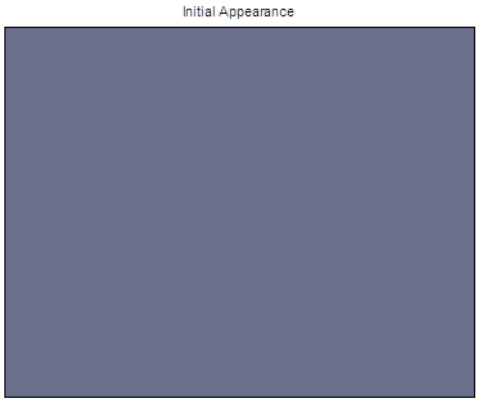

Figure 5-7. Color change program color patch output 1: The initial visual appearance of the violet sample, as seen under source D65 using standard observer functions from 1964.

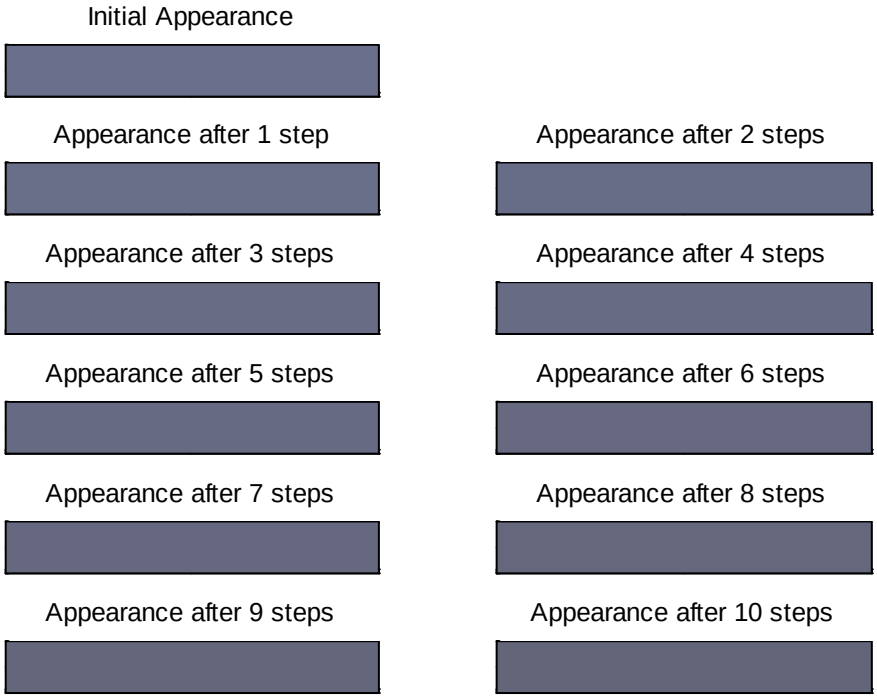

Figure 5-8. Color change program color patch output 2: The visual appearance of the sample initially and at each step of roughening. Roughening rate is 150 nm/step, and the sample is viewed under source D65 with 1964 standard observer functions.

Trying to distinguish between the colors in Figure 5-8 is a difficult, yet not entirely impossible, task for the human eye. However, if one can place the initial color side by side with the final color (after ten steps of roughening), the difference is easily noticeable. The last color patch output does just that; Figure 5-9 shows a box of color on a black background. The top triangle (A) is the initial appearance of the object, while the bottom triangle (B) shows the appearance after ten steps of roughening. As seen in Figure 6 above, the color difference here is a ΔE of ~3.7, and is easily detectable by the human eye.

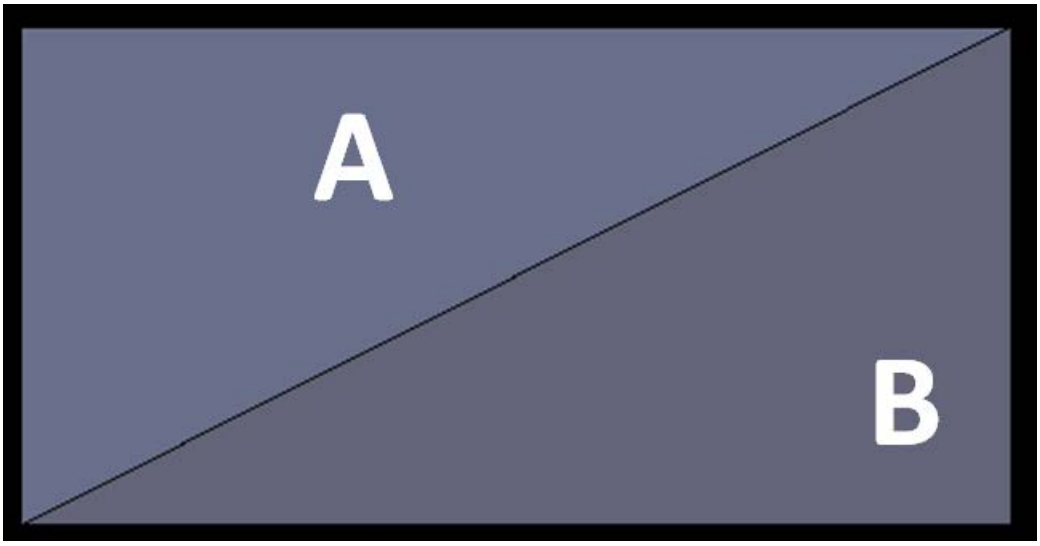

Figure 5-9. Color change program color patch output 3: The visual appearance of the sample initially (A) and after ten steps of roughening (B). Roughening rate is 150 nm/step, and the sample is viewed under source D65 with 1964 standard observer functions. The difference is equivalent to ΔE = 3.7.

The benefit of performing color calculations in a program as diverse and functional as the one presented here is that one can easily make comparisons between light sources, standard observer choices, and detector angles. For example, source metamerism may be demonstrated by running the program four times, each time using the same initial reflectance input, but changing the

light source used in each simulation. Figure 5-10 shows the same violet sample used in the above simulation, this time observed under four different light sources but with the same standard observer functions. That is, any perceived difference is strictly due to the change in the illuminant.

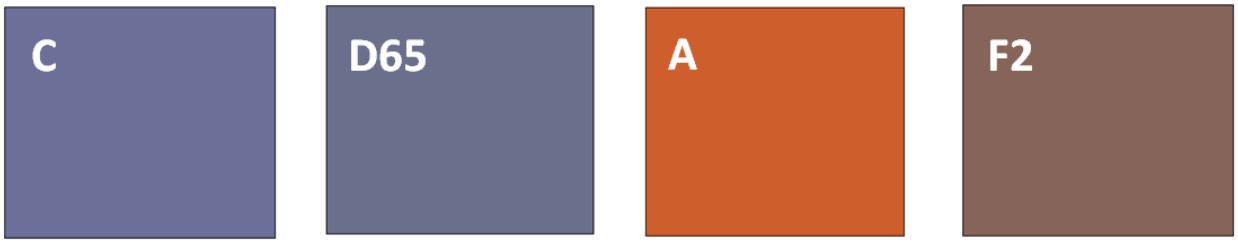

Figure 5-10. The color change program is used to simulate the visual effects of source metamerism. The violet puck is "viewed" under four different light sources (indicated by the text) using 1964 standard observer functions.

The versatility of the program is highly dependent on the imagination and the desired end-results specified by its user. Just as source metamerism is easily simulated in Figure 5-10, observer or geometrical metamerism may be simulated by altering the standard observer functions used or the angle of the detector, respectively. However, until experimentally verified values of ***k*** become available for different materials, the program will remain a strictly-theoretical simulation tool.

5.2.6. Suggestions for future improvement to the color change program

The program is currently at version 0.10 (with version 1.0 signifying a version ready for wide, inter-lab release), with some bugs still needing to be worked out. The first major change that should be made is to allow for various ranges of spectral distributions to be entered into the program seamlessly. Currently, only data in the 380-780 nm range with 5 nm steps is easily used; all other ranges and step sizes require slight modifications to the code.

The program assumes that all tristimulus values will satisfy $X/X_n > 0.00856$ (and similar for Y and Z), so that only the simplest form of the XYZ→CIE L*a*b* equations are used to convert to

L*a*b* color coordinates. Adding the conditional equations will allow for the program to handle very dark or very high chroma colors.

Experimentally, samples of various materials with known nanoscale surface roughnesses are needed to verify the prediction aspect of the program. Techniques that will allow for such nanoscale roughening to be added to samples are currently being investigated.

Finally, the program may be adopted as a small programming piece into other, much larger and comprehensive, electromagnetic radiation scattering and degradation models to form a more complete theory of electromagnetic transport in materials.

5.2.7. Summary of color change program

A program has been developed that is capable of simulating the changes in visual appearance of colored surfaces with increased surface roughness on the nanometer scale. The program uses as input the initial spectral reflectance of the unroughened sample, the roughening rate of the sample material, the light source, standard observer functions (either 1931 or 1964), and angle of detector, and produces as outputs XYZ, RGB, L*a*b*, ΔE, whiteness, yellowness, and tint indices of the material as a function of surface roughness, as well as visual color patches of the sample appearance at each step of the simulation. Qualification tests of the program have verified the integrity of its calculations, and a sample simulation with its graphical outputs has been presented here. Furthermore, the program has been used to quickly simulate source metamerism, without the need for measuring or collecting reflectance data under each source. The program is not ready for wide release, but major bugs have been identified and tractable solutions are being considered.

5.3. Composites

The fast-growing field of nanocomposite materials containing quantum dots, nanoparticles, graphene slabs, and carbon nanotubes will require scattering prediction methods and treatments that are functional across all length scales, regardless of the wavelength of incident light.

Not just inclusions, but heterogeneous phases, are critical to advanced composite manufacturing, as well. Light scattering simulations will shed insight into heterogeneity-based and phase-separation enabled performance and failure modes, such as incomplete dispersion of inclusions and improper phase separation of complicated copolymer blends. An example of morphological heterogeneity in an otherwise chemically or compositionally homogeneous material is crazing in a polymer that is the result of an applied and repeated stress that aligns polymer chains and effectively pulls them out of the amorphous bulk polymer. The polymer material now scatters light and appears white on the macroscale. This is readily seen by bending a cheap pen cap repeatedly. Long range molecular ordering imparted into the multiscale simulation framework will allow for the prediction of crazed polymer response.

5.4. Biological applications

Biological sciences and engineering makes great use of electromagnetic radiation transport models. Skin is a great example of a turbid, diffusive media, and so non-directional scattering models that rely on diffusion equations are apt for those systems[11]. Modified Kubelka-Munk theory may also be applied to biological tissue systems, and the multilayer modifications by Dorsey and Hanrahan will suite the multilayered dermal systems nicely[12]. Monte Carlo ray tracing has been effectively used to simulate radiation transport in biological suspensions[13], and simplified spherical harmonics approaches have also recently been used[14].

A framework for multilayer modeling and color and appearance prediction is perfectly suited for predictions of cosmetic appearance when applied to skin. Given a set of standard skin reflectance functions, a proposed cosmetic such as a foundation powder may be applied to various skin tones in simulation space, and the final appearance under different lighting conditions may be predicted. Just as in coatings and composites applications, the method would allow for more rapid screening of new material, dye, and pigment candidate materials before expensive R&D time and resources are spent in the physical laboratory.

5.5. Aerospace and defense applications

In aerospace coating technologies oftentimes stealth is desired for defense applications, but an equally useful application of this complete scattering simulation methodology is called for in the design of low solar load or so-called "cool" coatings that are highly reflective in the IR and NIR regions. These coatings are designed to reduce the solar heat transfer onto lightweight composite fuselage and wing components. Tracking the heat losses in a finite element simulation imparted by various proposed pigment systems will enable tracking and accumulation of scattering results into a collected heat response. This approach may serve as a useful screening protocol for candidate materials before costly in-service trials of those new materials are arranged.

The properties of tailored and designed surfaces with precise electromagnetic signature can be also be predicted over time with weathering, fiber debonding and other in-service conditions. The extension to a true in-service lifetime prediction model would be a logical next step for this work.

Another interesting application is the design of camouflage coatings, which are historically very rough in order to provide a matte appearance that minimizes coherent backscatter that can lead to unwanted detection by the enemy. Although the electromagnetic signature is well-defined and

designed here, the surfaces are difficult to clean. A rough camouflage primer with a flat and clear topcoat on the outermost surface would allow for a wipeable camouflage coating. Advanced multilayer simulation models like the work presented here will allow for the prediction of electromagnetic response with varying thicknesses and optical properties of clearcoat materials.

Finally, robust coatings and composite materials with designed broadband invisibility are needed to enhance warfighter safety and protect military assets. A new class of designed invisibility materials relies on the close but precise alignment of carbon nanotubes grown in a forest arrangement on various substrate materials[15]. The precise alignment creates a compound complex refractive index which very nearly matches that of air, and the resultant material exhibits near-perfect absorbance, absorbing electromagnetic radiation from radio waves to visible light to ultraviolet radiation. This class of materials offers a new approach to material cloaking, and the simulation methods outlined in this dissertation may aid in the R&D of such materials at an industrial scale. An approach to scale-up that is especially suited to this computational simulation toolbox is the incorporation of carbon nanotube forests with excellent broadband absorption onto the surface of microballoon or hollow pigments that are subsequently embedded in traditional organic coating materials; thus, designed invisibility is imparted into a familiar carrier system with minimal added weight.

5.6. Conclusions

This chapter has presented potential areas of use for multiscale radiation transport modeling in various commercial platforms, with a heavy emphasis on coatings applications and prediction of color change with imposed surface roughness. Although the emphasis was on coatings, the generality and adaptability of the models allows for straight-forward modification of individual framework components to predict the response of various materials of commercial and research

interest, including biological systems such as tissue or cosmetics, aerospace and defense applications, and novel composites. The extension of the multiscale framework to each of these areas would surely yield interesting results as well as useful research and product development tools.

5.7. References

1. Bennett, H.E. and J.O. Porteus, *Relation Between Surface Roughness and Specular Reflecance at Normal Incidence*. J. Opt. Soc. Am., 1961. **51**(2): p. 123-129.
2. Bennett, J.M. and L. Mattson, *Introduction to Surface Roughness and Scattering*. 1989, Washington, D.C.: Optical Society of America.
3. Bierwagen, G.P., *Estimation of Film Thickness Nonuniformity Effects on Coating Optical Properties*. Col. Res. Appl., 1992. **17**(4): p. 284-292.
4. Croll, S. and B. Hinderliter, *A framework for predicting the service lifetime of composite polymeric coatings*. J. Mater. Sci., 2008. **43**: p. 6630-6641.
5. Croll, S.G. and B.R. Hinderliter, *Statistical approaches for predicting weathering degradation and service life*. Prog. Org. Coat., 2006. **55**: p. 75-87.
6. Hinderliter, B. and S. Croll, *Monte Carlo Approach to Estimating the Pjotodegradation of Polymer Coatings*. JCT Res., 2005. **2**(6): p. 483-491.
7. Hinderliter, B.R. and S.G. Croll, *Simualtions of Nanosclae and Macroscopic Propert Changes on Coatings and Weathering*. JCT Res., 2006. **3**(3): p. 203-212.
8. Hinderliter, B.R. and S.G. Croll. *Predicting Coating Failure using the Central Limit Theorem and Physical Modeling*. in *The Fifth International Conference on Advances in Corrosion Protection by Organic Coatings*. 2009. Christ's College, Cambridge.
9. ASTM, ed. *ASTM Standards on Color and Appearance Measurement*. 4th ed. 1994, ASTM: Philadelphia, PA.
10. Berns, R.S., *Billmeyer and Saltzman's Principles of Color Technology*. 3rd ed. 2000, New York, NY: John Wiley.
11. Martelli, F., et al., *Light Propagation through Biological Tissue and Other Diffusive Media*. 2010, Bellingham, WA: SPIE Press.
12. Dorsey, J., H. Rushmeier, and F. Sillion, *Digital Modeling of Material Appearance*. 2008, New York: NY: Elsevier.
13. Chicea, D. and I. Turcu, *A Random Walk Monte Carlo Approach To Simulate Multiple Light Scattering On Biological Suspensions*. Roman. Rep. Phys., 2005. **57**(3): p. 418-425.
14. Chu, M., et al., *Light transport in biological tissue using three-dimensional frequency-domain simplified spherical harmonics equations*. Phys. Med. Biol., 2009. **54**: p. 2493-2509.
15. Shi, H., et al., *Low density carbon nanotube forest as an index-matched and near perfect absorption coating*. Appl. Phys. Lett., 2011. **99**: p. 211103.

CHAPTER 6. SUMMARY, IMPACTS, AND CONCLUSIONS

6.1. Summary of the dissertation

The transport behavior of electromagnetic radiation through a polymeric coating or composite is the basis for the material color, appearance, and overall electromagnetic signature. As multifunctional materials become more advanced and next generation in-service applications become more demanding, a need for predictive design of electromagnetic signature is desired. This dissertation presented various components developed and used in a computational suite for the study and design of electromagnetic radiation transport properties in polymeric coatings and composites. Focus was given to the treatment of the forward or direct scattering problem on surfaces and in bulk matrices of polymeric materials. The suite consists of surface and bulk light scattering simulation modules that may be coupled together to produce a multiscale model for predicting the electromagnetic signature of various material systems. Geometric optics ray tracing was used to predict the surface scattering behavior of realistically rough surfaces, while a coupled ray tracing-finite element approach was used to predict the bulk scattering behavior of material matrices consisting of microscale and nanoscale fillers, pigments, fibers, air voids, and other inclusions. Extension of the suite to color change and appearance metamerism was addressed, as well as the differences between discrete versus statistical material modeling.

6.2. Impacts of the research

The research presented in this dissertation has accomplished many things:

- A virtual, multiscale laboratory and electromagnetic radiation transport modeling approach has been designed, where the properties of electromagnetic signature of nanocomposite materials may be investigated, measured, and controlled.
- The coupling of surface and bulk scattering into a single adaptive, general, and rigorous approach has been developed and detailed, with an emphasis on coatings applications.
- Photon transport behavior in materials has been compiled into predictions for color and appearance change, as well as detectability when retroreflectance is concerned. This approach has been coupled to earlier Monte Carlo models of photodegradation in order to begin uncovering novel non-destructive evaluation and assessment methods using interrogating light beams.
- Photon transport behavior has been compiled into uncommon results, such as tracking the number of scattering events per incident photon, or the portion of a surface caught in shadow. These results shed new light on the surface scattering problem, and are useful tools in the assessment of rough surfaces being impinged on by incident radiation.
- Demonstration of retroreflectance onset in nanocomposites exhibiting inclusion coarseness was shown and quantified, an example of expanding the available knowledge concerning the light scattering behavior of nanomaterials. With a multiscale modeling approach such as the one presented here, a materials designer can detect at what loading level various nanomaterials become detectable by different optical systems and techniques.
- A computer code package was written to translate, interpret, and predict the spectral response of materials having nanoscale surface roughnesses.
- A translation matrix for XYZ to CIE L*a*b* was developed, out of necessity, and is documented in Appendix A.

6.3. Conclusions

An ongoing challenge in any simulation-driven area of research is the continual incorporation of new methods with historically proven methods, as well as the repackaging of those methods to serve new audiences of users. The work presented here combined two well-established light scattering simulation methods, one for surfaces and one for bulk inclusions, into a hybrid approach for whole-material, omniscale light scattering, which is flexible and adaptive to many material types, but which is also rigorous in its treatment of the radiative transfer mathematics. Gaps in the modeling capability left after combination were filled in with new techniques and approaches, specifically in the areas concerning the translation of photon transport to visual appearance. Forthcoming papers from the author will present the results of scaled up hybrid light scattering simulations, will address nuances in photon queue and accounting structures, and will present experimental validation of the models using various materials with industrial importance.

APPENDIX A. A TRANSFORMATION MATRIX FOR CONVERTING TRISTIUMULUS VALUES (XYZ) TO CIE L*a*b*

In 1976 the International Commission on Illumination (CIE) established the following equations for transforming the tristimulus values XYZ into CIELAB L*a*b* coordinates:

$$L^* = 116\left(\frac{Y}{Y_n}\right)^{\frac{1}{3}} - 16 \qquad \text{Equation A-1}$$

$$a^* = 500\left[\left(\frac{X}{X_n}\right)^{1/3} - \left(\frac{Y}{Y_n}\right)^{1/3}\right] \qquad \text{Equation A-2}$$

$$b^* = 200\left[\left(\frac{Y}{Y_n}\right)^{1/3} - \left(\frac{Z}{Z_n}\right)^{1/3}\right] \qquad \text{Equation A-3}$$

In the above equations, X_n, Y_n, and Z_n, are tristimulus values for a reference white dependent on light source and standard observer functions used. The equations above hold for all cases when (X/X_n), (Y/Y_n), and (Z/Z_n) are greater than 0.008856. The astute reader will note that this does not hold true only for very dark colors. In almost all cases, the above equations may be used, and in cases where they may not be used the decision should be quite obvious.

While early advances in color technology were purely qualitative, present color science is ubiquitously handled by computers that are capable of handling and manipulating large amounts of data, usually in vector-matrix notation. The quantitative nature of color science today, combined with the large number of different numerical descriptions of color in use, all rely on the ability to quickly and efficiently convert from values residing in one color space to those in another. Many 3x3 transformation matrices exist that quickly convert RGB to XYZ and vice versa, as well as many

Bradford matrices that transform color coordinates in from one illuminant to the same coordinates under a different illuminant. However, a literature and internet search has shown that no transformation matrix has been proposed for converting from XYZ to L*a*b*. These proposed transformation matrices will complement the vector-matrix notation of numerical color used by Allen, Berns, etc. While the exercise is arguably a purely academic task of mathematical manipulation, it remains as being one of the last (possibly overlooked?) set of transformation matrices to be addressed.

Take t to be a 3x1 column vector containing the tristimulus values XYZ as such:

$$t = \begin{bmatrix} X \\ Y \\ Z \end{bmatrix} \qquad \text{Equation A-4}$$

Convert t into a 4x1 column vector u containing a unit place holder as such:

$$u = \begin{bmatrix} X \\ Y \\ Z \\ 1 \end{bmatrix} \qquad \text{Equation A-5}$$

Now transpose u and take the cube root of each of its components to get row vector T:

$$T = (u')^{1/3} = \begin{bmatrix} X^{1/3} \\ Y^{1/3} \\ Z^{1/3} \\ 1 \end{bmatrix}' \qquad \text{Equation A-6}$$

Extracting the cube roots of the tristimulus values out of the classic XYZ to L*a*b* equations and rearranging the equations into matrix form gives the root version of the XYZ to L*a*b* transformation matrix S, as such:

$$S = \begin{bmatrix} 0 & 500\left(\frac{1}{X_n}\right)^{\frac{1}{3}} & 0 \\ 116(\frac{1}{Y_n})^{1/3} & -500\left(\frac{1}{Y_n}\right)^{\frac{1}{3}} & 200(\frac{1}{Y_n})^{1/3} \\ 0 & 0 & -200(\frac{1}{Z_n})^{1/3} \\ -16 & 0 & 0 \end{bmatrix}$$ Equation A-7

Now multiplying T by S gives the 1x3 row vector of corresponding L*a*b* values:

$$T * S = [L^* \quad a^* \quad b^*]$$ Equation A-8

In the case of illuminant C and 1964 (10 degree) standard observer functions, X_n, Y_n, and Z_n are 97.285, 100, and 116.145, respectively, and S is simplified as Equation A-:

$$S_{C,64} = \begin{bmatrix} 0 & 108.7146 & 0 \\ 24.9914 & -107.7217 & 43.0887 \\ 0 & 0 & -40.99175 \\ -16 & 0 & 0 \end{bmatrix}$$ Equation A-9

Similar transformation matrices can easily be made from the root of S for varying illuminants, standard observer choices, and reference whites. The set of S transformation matrices for standard observer choices 1964 and 1931 and sources C and D65 are given in Table A-1.

Table A-1. S Transformation Matrices for Sources C and D65 and Standard Observer Functions from 1931 and 1964.

Source	Std. Obs.	S
C	*1964*	$\begin{bmatrix} 0 & 108.7146 & 0 \\ 24.9914 & -107.7217 & 43.0887 \\ 0 & 0 & -40.99175 \\ -16 & 0 & 0 \end{bmatrix}$
X_n	97.285	
Y_n	100	
Z_n	116.145	
C	*1931*	$\begin{bmatrix} 0 & 108.4223 & 0 \\ 24.9914 & -107.7217 & 43.0887 \\ 0 & 0 & -40.7491 \\ -16 & 0 & 0 \end{bmatrix}$
X_n	98.074	
Y_n	100	
Z_n	118.232	
D65	*1964*	$\begin{bmatrix} 0 & 109.6521 & 0 \\ 24.9914 & -107.7217 & 43.0887 \\ 0 & 0 & -42.0880 \\ -16 & 0 & 0 \end{bmatrix}$
X_n	94.811	
Y_n	100	
Z_n	107.304	
D65	*1931*	$\begin{bmatrix} 0 & 109.5613 & 0 \\ 24.9914 & -107.7217 & 43.0887 \\ 0 & 0 & -41.8835 \\ -16 & 0 & 0 \end{bmatrix}$
X_n	95.047	
Y_n	100	
Z_n	108.883	

APPENDIX B. ANNOTATED BIBLIOGRAPHY

This appendix is the author's attempt to highlight specific references which were most insightful, enjoyable, helpful, and in general served as excellent launching points during the research presented in this dissertation. The order of the list is alphabetical by author and is by no means meant to be an exhaustive bibliography for light scattering and color and appearance prediction.

1. Beckmann, Petr; Spizzichino, Andre. The Scattering of Electromagnetic Waves from Rough Surfaces. This work provides an historical perspective of the theory of light scattering by rough surfaces, and is best-suited for a broad overview of light scattering theory that is fairly rigorous in its mathematical treatment.
2. Bennett, Jean M.; Mattsson, Lars. Introduction to Surface Roughness and Scattering. A slender yet excellent volume that covers much of the material in Beckmann and Spizzichino, but with a well-thought economy of words applied to the discussion. Unfortunately, the book is currently out of print, though it seems to be a standard within many university and industrial libraries.
3. Bergström, David. The Absorption of Laser Light by Rough Metal Surfaces. PhD thesis from Luleå University of Technology in Luleå, Sweden. This doctoral thesis served as a well-established launching-off point for a fair portion of the surface scattering simulation work presented in this dissertation. Bergström's codes for surface scattering are some of the best currently available, and they are presently hosted at his website, mysimlabs.com, in MATLAB m-file format.
4. Berns, Roy S. Billmeyer and Saltzman's Principles of Color Technology. One of the premier texts on color definition, space, measurment, and interpretation, this volume by Berns is best place to start for anybody looking to explore color with mathematics.

5. Bohren, Craig F. Clouds in a Glass of Beer: Simple Experiments in Atmospheric Physics. Probably one of the best popular science books I've read, this slim volume by Bohren elaborates on many commonly observed phenomenon related to atmospheric physics and chemistry. An excellent read for any curious-minded person.
6. Bohren, Craig F.; Huffman, Donald R. Absorption and Scattering of Light by Small Particles. After reading Clouds in a Glass of Beer, sample a text by Bohren that does away with pop niceties and delves right into the mathematical heart of the matter. Absorption and Scattering of Light by Small Particles is unnecessary if one is entirely familiar with the earlier volume by Van de Hulst (discussed below), though the mathematical formalism presented by Bohren and Huffman is easier to digest than that of their predecessor.
7. Dorsey, Julie; Rushmeier, Holly; Sillion, Francois. Digital Modeling of Material Appearance. A fantastic and delightful volume that serves as a computationally-minded extension to the work by Berns discussed above. Dorsey and her co-authors provide a wonderfully mid-level review of light scattering and reflections models, including empirical, semi-empirical, and first-principles formalisms. The book is flush with illustrations, and the breadth of materials covered, from wood to ceramics to glass to flesh is truly incredible. Highly recommended for those interested in the computational simulation of material appearance.
8. Feynman, Richard P. QED: The Strange Theory of Light and Matter. A Feynman classic, this series of lectures given to a mostly unscientifically-minded crowd discusses the most fundamental aspects of quantum electrodynamics, contains a wonderful discussion of surface scattering and photon-electron interactions, and introduces the novice to Feynman diagrams. Most highly recommended.
9. Fleisch, Daniel. A Student's Guide to Maxwell's Equations. Fleisch devotes an entire volume to the study of the Maxwell equations, where many textbooks grant the mathematics only a

chapter at most. Fleisch's volume is approachable to the nth degree; each aspect of the Maxwell equations is discussed in depth, at the individual variable level. Highly recommended when a rigorous understanding of the Maxwell equations is desired.

10. Maradudin, Alexei A., ed. Light Scattering and Nanoscale Surface Roughness. Maradudin's recent compilation of papers by various heavyweights in the field of light scattering is a joy to read. The volume is broad enough to stand on its own as a text on light scattering, though the recent publication date ensures that the text won't feel dusty or dated, even to those readers with many years of experience in the field.
11. Martelli, Fabrizio; Del Bianco, Samuele; Ismaelli, Andrea; Zaccanti, Giovanni. Light Propagation through Biological Tissue and Other Diffusive Media. Martelli and his co-authors provide an interesting account of light scattering through mostly diffusive media, with an emphasis on skin and other biological tissue. A worthwhile read for those seeking understanding of how electromagnetic radiation transport mathematics is applied to fields outside the materials engineering, chemistry, and hard physics domains.
12. Van de Hulst, H.C. Light Scattering by Small Particles. Van de Hulst gave to the community one of the first texts on light scattering by small particles The text is still relevant today, fifty-five years after its original printing, and it's affordable list price on Dover makes it worthy of adding to any light scattering library, though the information contained in its pages has been superseded and slightly improved by Bohren and Huffman.

COLOPHON

This disquisition was composed using Microsoft Office 2010 Garamond, set in twelve-point height, and written on a Dell Precision M4600 laptop computer.

Garamond is an old-style serif typeface named after Claude Garamond (c. 1480-1561), a French punch-cutter and publisher who is credited with the introduction of the apostrophe, the accent, and the cedilla to the French language. Jean Jannon used many Garamond stylistics in his development of the modern set of Garamond typefaces developed sixty years after Garamond's death. Characteristics of Garamond style are the small and squished bowl in the **a**, and the small eye in the **e**. Garamond is considered one of the most legible and readable serif fonts in print applications, and has also been demonstrated to be one of the most ink-conservative fonts.

Despite its worldly serif appearance, Garamond has rich ties to youth culture. It was used for printing the preponderance of Theodore Geisel's work which he published under his most famous nom de plume, Dr Seuss. All American additions of J.K. Rowling's Harry Potter books are set in twelve-point Garamond, with the exception of *Harry Potter and the Order of the Phoenix*, which is set in 11.5-point Garamond because it's so dang long. The Hunger Games trilogy by Suzanne Collins is set in Adobe Garamond Pro, and Abercrombie & Fitch uses a Garamond variant in its logo work.

One can visit a complete set of original Garamond dies and matrices at the Plantin-Moretus Museum in Antwerp, Belgium.

The choice of font was mine to make. Regrettably, the decision to use a Dell laptop was not.